BRNO UNIVERSITY OF TECHNOLOGY
VYSOKÉ UČENÍ TECHNICKÉ V BRNĚ

FACULTY OF ELECTRICAL ENGINEERING AND COMMUNICATION
FAKULTA ELEKTROTECHNIKY
A KOMUNIKAČNÍCH TECHNOLOGIÍ

DEPARTMENT OF RADIO ELECTRONICS
ÚSTAV RADIOELEKTRONIKY

INTERFERENCE OPTIMIZATION IN CELLULAR COMMUNICATION SYSTEMS
OPTIMALIZACE INTERFERENCÍ V CELULÁRNÍCH KOMUNIKAČNÍCH SYSTÉMECH

DOCTORAL THESIS TOPIC
POJEDNÁNÍ

AUTHOR   Edward Kassem
AUTOR PRÁCE

SUPERVISOR   Ing. Jiří Blumenstein, Ph.D.
ŠKOLITEL

BRNO 2018

ABSTRACT

This thesis is divided into six chapters. The first chapter clarifies the differences between uplink layers of LTE and LTE Advanced systems. It investigates the channel characteristics of device to device (D2D) communication underlaying LTE Advanced network and provides the main key mechanisms of interference management. The structure of Software Defined Radio platform which can be used in channel sounding is also presented. The second chapter evaluates and compares both LTE and LTE Advanced uplink layer performances. Therefore, the structure of previously described LTE Advanced transmitter and receiver with all signal processing stages are implemented in MATLAB. The generated signals of both above mentioned systems are transmitted over different International Telecommunication Union channels. Different channel estimation and signal detection techniques to recover the transmitted signal are used. The results are presented in terms of bit error rate and throughput performance curves. The third chapter suggests fractional frequency reuse with three power levels technique as an interference mitigation method. The normalized capacity densities of the cells and their regions with three cases of user distribution inside the cells are considered. The correlation between the overall capacity and the radius of each region is presented. The achieved results of the proposed scheme are compared with traditional frequency reuse (Reuse-3) technique. The fourth chapter provides a research about another method of interference mitigation. The verification of cooperative spectrum sensing methods using four different real channel conditions is conducted. Indoor-indoor, indoor–outdoor, outdoor-indoor, and outdoor-outdoor environments are taken into consideration. The defined system is tested using the Universal Software Radio Peripheral devices. Two types of detectors; the energy detector and the Kolmogorov Smirnov statistical detector have been implemented at the receiver for signal sensing evaluation. One of the main requirements of D2D communication is a good channel impulse response characteristics knowledge. Therefore, the fifth chapter presents the proposed frequency domain Zadoff-Chu sounding as an alternative technique of channel sounding. Using the proposed method, the basic channel characteristics like RMS delay spread, mean excess delay, path-loss and coherence bandwidth are extracted in (20x) shorter time period compared to the continuous wave method. The channel characteristics of an outdoor long range static channel campaign for both ultra-high and super high frequency bands with co-polarized horizontal and vertical antenna configurations are also investigated. The sixth chapter concludes the thesis.

KEYWORDS

ALMMSE, cellular networks, channel estimation, cooperative sensing, DRMS, D2D, interference, LTE Advanced, MIMO, physical layer, SSD, USRP, Zadoff-Chu, ZF, 5G.

DECLARATION

I declare that I have written my doctoral thesis on the theme of "Interference Optimization in Cellular Communication Systems" independently, under the guidance of the doctoral thesis supervisor and using the technical literature and other sources of information which are all quoted in the thesis and detailed in the list of literature at the end of the thesis.

As the author of the doctoral thesis I furthermore declare that, as regards the creation of this doctoral thesis, I have not infringed any copyright. In particular, I have not unlawfully encroached on anyone's personal and/or ownership rights and I am fully aware of the consequences in the case of breaking Regulation §11 and the following of the Copyright Act No 121/2000 Sb., and of the rights related to intellectual property right and changes in some Acts (Intellectual Property Act) and formulated in later regulations, inclusive of the possible consequences resulting from the provisions of Criminal Act No 40/2009 Sb., Section 2, Head VI, Part 4.

Brno   . . . .

                                                  (author's signature)

ACKNOWLEDGEMENT

Brno   . . . .
                                                                (author's signature)

CONTENTS

LIST OF FIGURES

LIST OF TABLES

INTRODUCTION

Digital communication systems are becoming increasingly attractive because of high speed data transmission. Moreover, future wireless systems, especially mobile communication systems are expected to support efficient transmission and provide high throughput. Long-Term Evolution (LTE) Advanced or 3rd Generation Partnership Project (3GPP) LTE Release 10 standard [1, 2] consists of various developed radio access technologies supporting advanced services.

LTE has been designed to support only packet switched services, in contrast to the circuit-switched model of previous cellular systems. Specifically, data rate requirements have been increased. In order to support advanced services and applications, 100 Mbps for high and 1 Gbps for low mobility scenarios must be implemented [3, 4]. In September 2009, 3GPP Partners made a formal submission to the International Telecommunication Union (ITU) proposing that LTE Release 10 and beyond (LTE advanced) should be evaluated as a candidate for International Mobile Telecommunications (IMT)-Advanced [3]. This release provides best-in-class performance attributes such as peak and sustained data rates and corresponding spectral efficiencies, capacity, latency, overall network complexity and quality of service (QoS) management. One of the major advantages of LTE Advanced is its backward compatibility[3], that means, LTE devices can work in LTE Advanced and LTE Advanced devices can operate in LTE as well.

Furthermore, it supports Multiple Input Multiple Output (MIMO) [5] to improve the performance of the LTE system [6], spectral efficiency and data throughput. MIMO defines multiple antennas on the receiver (RX) and transmitter (TX), which are used to: utilize the multipath effects, reduce interference and lead to high throughput. Multipath occurs when different signals arrive at the receiver at various time intervals. MIMO transmits data in multiple unique parts in the same radio channel at the same time. The receiving ends use an algorithm or employ special signal processing to receive the signal that was originally transmitted. This and other techniques are included in the LTE Release 10 specifications [7].

One of the most promising methods of communication is D2D communication [8]. D2D communication gives different devices the ability to create a direct wireless link between them. Realization of D2D communication is a step forward to reduce the communication delay and increase the network capacity [9]. Both the unlicensed and licensed spectrum can be occupied by D2D users. Therefore, two types of bands are implemented for D2D communication. In outband, D2D does not share the frequencies with a cellular network. This type of communication has an advantage of interference absence between the D2D users and cellular users. However, D2D users should have two interfaces in order to support cellular communication simul-

taneously with D2D communication. Inband D2D operates on a licensed cellular spectrum. The operating inband is divided into underlay D2D communication where both the cellular and D2D user share the same frequencies and overlay when each of the above mentioned kind of users has its own dedicated frequency band.

This study will conduct underlay D2D communication as it is a more spectrum efficient method. The main focus of D2D communication underlaying cellular networks is ensuring minimum interference between these two technologies. There are several key mechanisms for mitigating interference among the cellular and D2D communication users. Some of these mechanisms are mode selection, distributed resource allocation, power control, and cooperative communication. Channel measurements are also an important factor in order to achieve high capacity and throughput in any communication system. These measurements should be accurate and fast enough in order to support not only stationary devices but mainly mobile ones. The receiver measurements should obtain full band channel information by integrating the sounding sequences over time and frequency, and applying advanced methods of channel estimation, equalization, demodulation and decoding.

This dissertation is divided into several chapters. The first chapter introduces the basic principles in the design of LTE Advanced and compares it with the previous LTE system. Communication systems including a TX and RX are presented. It is followed by frame structure differences. The evolution of LTE to LTE Advanced and the corresponding changes in the uplink reference signals are described. An overview about D2D communication and various kinds of interference mitigation are explained. Software Defined Radio (SDR) including the hardware and software are presented. The purpose of the first chapter is to provide a brief description of the techniques and equipment that will be used in this dissertation. The second chapter gives an overview of the different radio channels. It also presents the different channel estimation and signal detection techniques which can be used in the LTE Advanced system. Then the basic structure of the uplink demodulation reference signals (DMRSs) in LTE and LTE Advanced are depicted. After presenting a complete picture of the LTE and LTE Advanced system (TX, channel, RX, channel estimation, signal detection techniques and the reference signal which can be used in this process), the modified version of the Vienna LTE uplink level MATLAB code simulator is depicted. The performance results of the LTE Advanced system are presented and compared with the achieved results in LTE. The third chapter describes the interference management method in the LTE Advanced system. This study can be considered as the first step for an underlaying D2D communication realization. Fractional Frequency Reuse (FFR) with Three Power Levels is studied and suggested as a suitable method for the LTE Advanced system. Capacity results of Fractional Frequency Reuse with Three Power Levels will be presented and discussed. D2D

communication is one of the features of LTE Advanced technology. Cognitive Radio is a topic which has attracted lots of interest from researchers recently; it is a promising technology that could play a strong role in future communication systems. The results of Cooperative Spectrum Sensing for D2D communication are depicted in the fourth chapter. The measurements are done for different signals using the LTE Advanced spectrum. Finally the fifth chapter presents the proposed method of channel sounding for D2D communication. This method is compared with a frequency sounding method. The proposed method is tested using different indoor real channels. The proposed method provides quicker and more efficient channel measurements which can be used in D2D time-varying channels. The channel measurement campaign of outdoor long-range environments and the sounder systems for ultra high frequency (UHF) and super high frequency (SHF) bands is also described. The channel measurement results are captured for line of sight (LOS) and non-line of sight (NLOS) outdoor environments with different polarization combinations. Based on channel measurement results, the root-mean-square (RMS) delay spread, the path loss, the channel frequency response (CFR) variation, and the coherence bandwidth are analyzed. Chapter six concludes the dissertation.

AIMS OF THE THESIS

The dissertation describes the physical layer of LTE Advanced and D2D communication suitability. As mentioned above, D2D communication is promising technology which can be used for capacity and throughput increment of cellular networks. However, implementation of D2D communication into LTE Advanced systems causes huge interference. In order to mitigate interference, more improved methods of channel measuring and interference cancellation should be proposed. Therefore, several researches are conducted. The results could be summarized as:

- LTE Advanced uplink link level evaluation. In order to perform the evaluation, several modifications are applied on both the TX and RX of previously developed LTE systems. Moreover, the modifications include two extra processes: layer mapping and precoding. In addition, MIMO technology with various system settings is involved. The demodulation reference signal is also generated and employed. The effects of these modifications and its dependency on bit error rate (BER) and throughput are explored. All these modifications considerably improved LTE Advanced performance in the case of BER and throughput values. The motivation of this part was to implement an uplink layer of the LTE Advanced system which could be used for testing in further researches.

- FFR with three power levels method is suggested to be used as a co-channel interference (CCI) coordination and avoidance method. It implements multiple power levels and uses the whole available bandwidth in each cell. The optimized capacity densities of the cells and their regions are evaluated. Three different cases of user distribution, uniform, and non-uniform (non-uniform distributions with clustering to the BS and the edge of the cell), are considered. This study was conducted in order to suggest new methods of interference cancellation which can be used in future D2D communication.

- Interference mitigation using the cooperative spectrum sensing method is also evaluated. This system is built to insure the effectiveness of using cooperative sensing approach in D2D communication. One transmitter and two receivers are implemented. Two types of detectors, the energy detector (ED) and the Kolmogorov Smirnov (KS) based statistical detector, have been scripted at the receivers for the signal sensing evaluation. This model allows different signals to be transmitted. The signals are processed using Universal Software Radio Peripheral (USRP) devices to insure the effectiveness of the model in a real channel environment.

- Frequency domain Zadoff-Chu sounding technique is proposed. It depends on the most important sequence (Zadoff-Chu) as a part of the uplink layer of

LTE Advanced systems. The proposed technique can be used for both indoor and outdoor channel measurements. The carrier frequency of the transmitted Zadoff-Chu sequence is swept across the whole measured bandwidth. This approach can be considered as an improved way of channel sounding in vehicle channels for D2D communication. The proposed method provides quicker and more efficient channel measurements. The technique is tested using different real channel conditions between the TX and RX (LOS, NLOS). RMS delay spread, mean excess delay, coherence bandwidth and path loss are extracted for a real channel environment.

- The ability of deploying D2D communication underlay 5G network in the wideband long-range static channel for both UHF and SHF bands, as a part of fifth generation (5G) New Radio (NR) frequency band allocation, is tested. Both LOS microcell and NLOS macrocell measurements are involved. For a microcell LOS environment (with 315 m distance), the CFR variation, path loss, and RMS delay spread distribution in the case of vertical and horizontal polarizations for both 1.3 GHz and 5.8 GHz center frequencies are provided. In the case of macrocell NLOS environments (with 2.089, 4.11, and 5.429 km distances), in addition to all previous mentioned parameters, distance dependence of the path loss and the RMS delay spread are analyzed. RMS delay spread dependence of the coherence bandwidth is also investigated

By considering all of the above mentioned points, the dissertation covers the key mechanisms of D2D communications underlay LTE Advanced network functionality and provides several proposed methods to improve D2D performance. These mechanisms are interference cancellation, cooperative communications, accurate and fast channel estimation.

1 THEORETICAL BACKGROUND

This chapter is divided into three sections. The first section gives an overview about uplink layers of LTE and LTE Advanced systems. This is helpful in further LTE Advanced system implementation and its channel sounding. The second one describes D2D communication and the main key mechanisms that makes it work in cooperation with LTE advanced. The last section defines the structure of the SDR systems and describes the one that will be used in this research.

1.1 LTE and LTE Advanced Uplink Layer

The 3GPP LTE Standard Release 10 [2], commonly named as LTE advanced, is the next major milestone in LTE Release 8 [10] evolution. In this chapter, LTE and LTE Advanced system structures, followed by the frame structure overview, are presented. Furthermore, the difference between the generations of demodulation reference signals in both previous mentioned systems are described.

1.1.1 LTE and LTE Advanced System Structures

This section concentrates on the Physical Uplink Shared Channel (PUSCH). This channel carries user data. It optionally supports three types of modulation: QPSK, 16QAM and 64QAM [10]. Information bits are firstly generated, then cyclic redundancy check (CRC) bits are calculated and attached to it. After that the output block is segmented to the code blocks, then channel-coded with a turbo code with a rate of 1/3, before being adapted by a rate matching process for a final suitable code rate. Then it sequentially concatenated the rate matching outputs for the different code blocks and multiplexed with control information. Afterwards, one stream of information data is generated using the channel intervaler. Note that only one stream in the LTE uplink transmitter can be generated. This stream is called codeword. After this process, the bits deal with the following blocks: scrambling, modulation mapping, Discrete Fourier transform (DFT) spreading, sub-carrier mapping and Frequency Division Multiplexing Access (OFDMA).

There are several differences between the two LTE releases 10 and 8, which are shown in Fig. 1.1 [11]. The blue blocks depict the physical uplink shared channel process for the LTE transmitter, whereas the LTE Advanced transmitter is described by the whole diagram. The LTE Advanced transmitter can generate up to two different codewords instead of one generated by LTE. This evolution provides best-in-class performance attributes such as peak and sustained data rates and corresponding spectral efficiencies, capacity, and QoS management. These codewords
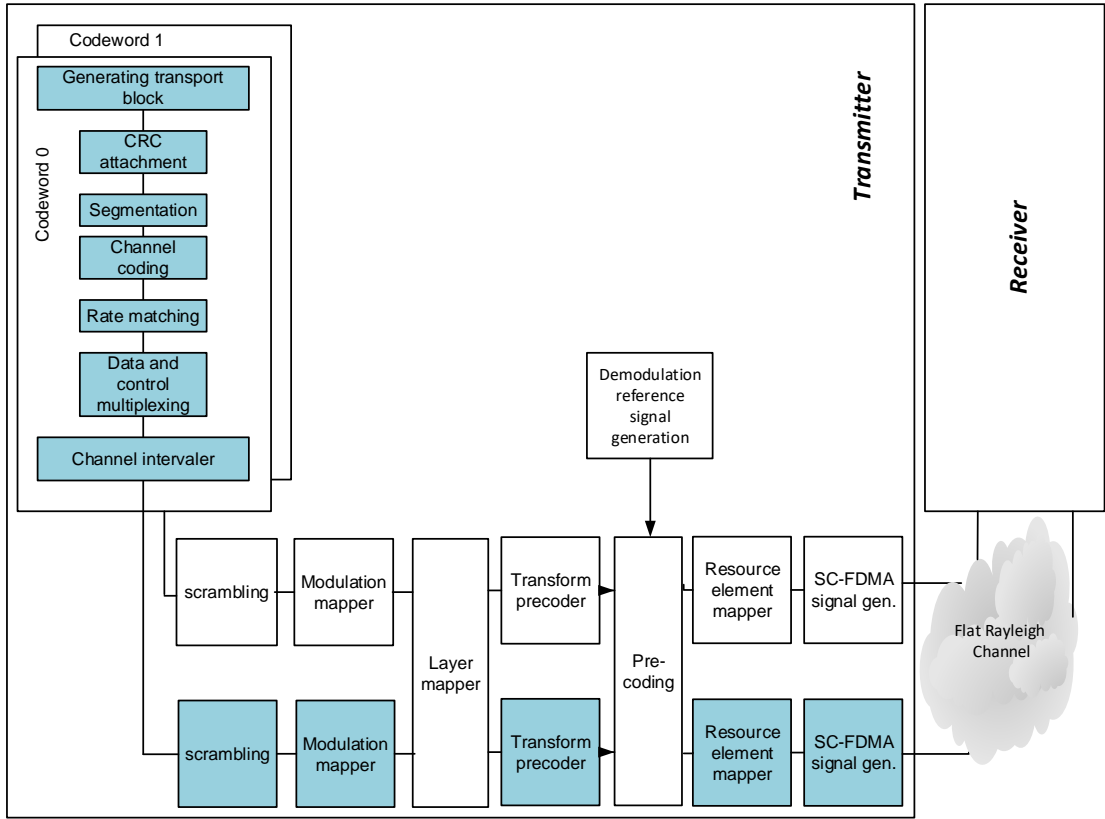
Fig. 1.1: LTE Advanced system model. Source: author [11].

can be mapped to a maximum of four layers, depending on the configuration of the layer mapper block. This process guarantees MIMO properties for uplink layers of the LTE Advanced system. Precoding of the complex-valued symbols can also be used in LTE advanced.
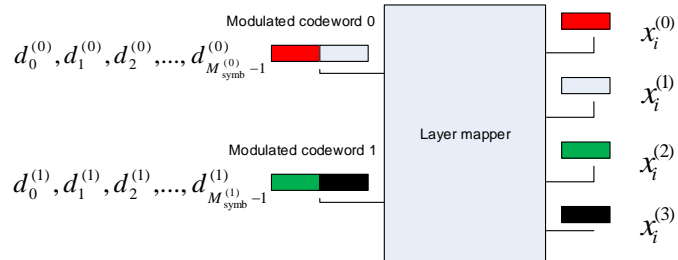
Fig. 1.2: Description of the function of the layer mapper. Source: author [11].

Layer Mapper: The main function of the layer mapper is to divide data

streams into several transmission layers (up to four layers) as shown in Fig. 1.2 [11]. $M_{symb}^{(layer)}$ is the number of modulated symbols in the corresponding layer and $M_{symb}^{(layer)} = M_{symb}^{(0)}/2 = M_{symb}^{(1)}/2$; $d^{(0)}(i)$ and $d^{(1)}(i)$ are the sequence symbols in codeword 0 and codeword 1, respectively. The function of the layer mapper is described in Eq. 1.1.

$$
\begin{aligned}
x^{(0)}(i) &= d^{(0)}(2i) \\
x^{(1)}(i) &= d^{(0)}(2i+1) \\
x^{(2)}(i) &= d^{(1)}(2i) \\
x^{(3)}(i) &= d^{(1)}(2i+1)
\end{aligned}
\tag{1.1}
$$

Precoding [12] usually takes place after the layer mapping stage and its structure for the uplink antenna is very similar to downlink non-codebook based precoding. The maximum setting of uplink antenna precoding supports transmission using up to four antenna ports and deals with spatial multiplexing with up to four layers. Note that spatial multiplexing supports $P = 2$ or $P = 4$ antenna ports and defined in Eq. 1.2, where $y^{(0)}(i), ..., y^{(v-1)}(i)$ are the sequences of the data symbols in corresponding v layers after transform the precoder; $z^{(0)}(i), ..., z^{(P-1)}(i)$ are the sequences of the data symbols in P ports. Precoding in the physical uplink shared channel has a maximum of four different states of input and four different states of output, so the precoding matrix W of size Pxv is given by one of the entries in Tables $5.3.3A.2$ [2].

$$
\begin{bmatrix}
z^{(0)}(i) \\
\cdot \\
\cdot \\
z^{(P-1)}(i)
\end{bmatrix}
= W
\begin{bmatrix}
y^{(0)}(i) \\
\cdot \\
\cdot \\
y^{(v-1)}(i)
\end{bmatrix}
\tag{1.2}
$$

In order to retrieve the transmitted signal in the receiver, the transmitter inserts occasional reference symbols into the data stream, which have a pre-defined amplitude and phase. This operation happens in the resource elements mapper block after generating and precoding the reference signal.

Single-carrier Frequency Division Multiple Access (SC-FDMA): [13]: SC-FDMA is the best solution for the LTE Advanced uplink due to the importance of the low cubic metric and corresponding high power-amplifier efficiency. These are very important properties for user equipment because of battery constraints as well as demanding construction of sufficiently linear power amplifiers.

1.1.2 Frame Structure Overview

The radio frames in both LTE and LTE Advanced have the same structure. In the time domain, it is 10 ms long and consists of 10 subframes of length 1 ms, and each

subframe contains two slots. Each slot has a 0.5 ms duration and consists of seven or six of OFDMA symbols corresponding to a normal or extended cyclic prefix. Both normal and extended cyclic prefixes are described in Tab. 1.1.
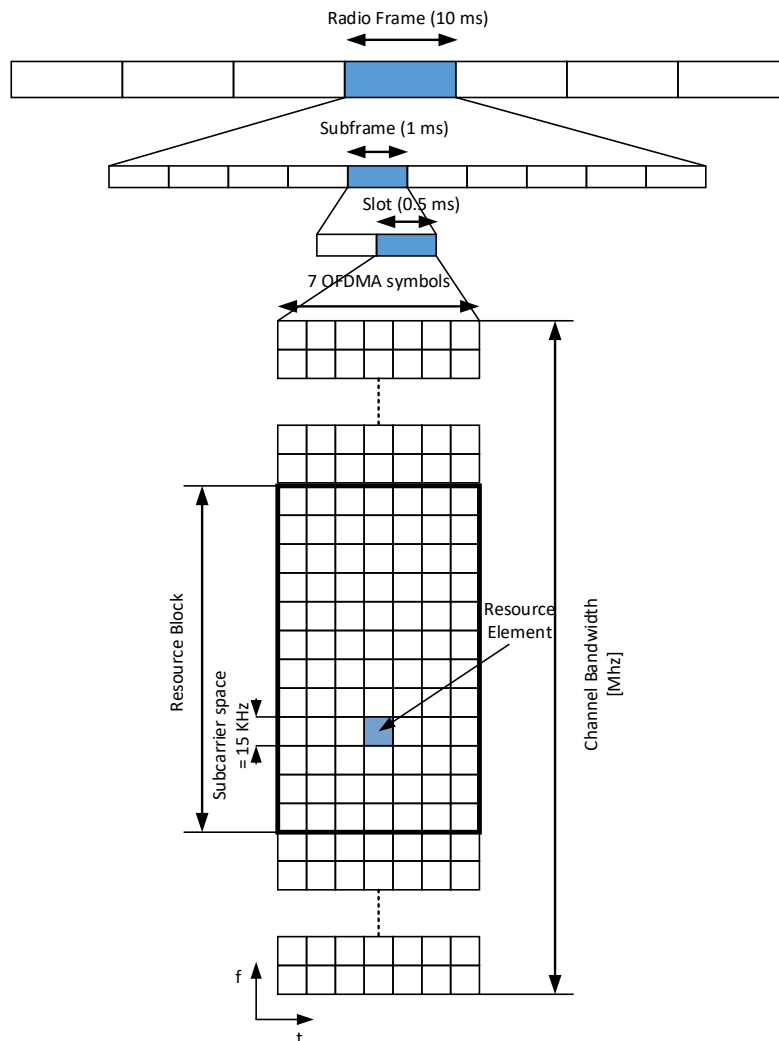
Fig. 1.3: Frame structure in time and frequency domain [2].

In the frequency domain, according to the used bandwidth, radio frame consists of number of subcarriers. The group of 12 subcarriers in each slot is called resource block. The smallest element is called resource element. The length of the resource element is one symbol in the time domain and one subcarrier in the frequency domain. The subcarrier spacing between two consecutive subcarriers is $\triangle f = 15$ kHz or $\triangle f = 7.5$ kHz depends on the parameter in OFDMA signal generation. LTE Advanced (Release 10) define six bandwidths (1.4, 3, 5, 10, 15, 20 MHz) which are

Tab. 1.1: Normal and extended cyclic prefix.

Configuration	Cyclic prefix length $N_{CP,l}$
Normal cyclic prefix $\triangle f = 15kHz$	160 for $l = 0$
	144 for $l = 1, 2, ..., 6$
Extended cyclic prefix $\triangle f = 15kHz$	512 for $l = 0, 1, 2, ..., 5$
Extended cyclic prefix $\triangle f = 7.5kHz$	1024 for $l = 0, 1, 2$

corresponding to the following number of resource blocks (6, 15, 26, 50, 75, 100). The whole structure of the radio frame is shown in Fig. 1.3

1.1.3 Demodulation Reference Signal

In this section, the basic structure of the uplink DMRS [10] in LTE is described. Then the additional properties are added to fit LTE Advanced requirements. The exact position of the single PUSCH DMRS symbols in each uplink slot depends whether a normal or extended cyclic prefix (CP) [10] is used. In the case of transmission, the demodulation reference signal in the PUSCH channel is done within the fourth and eleventh symbol of each uplink subframe if this channel has a normal CP and the third and tenth symbols in the case of extended CP [14]. To support a large number of user equipment, a huge number of reference signal sequences $r_{u,v}^{(\alpha)}(n)$ [10] should be generated. These sequences are defined by a cyclic shift α of a base sequence $\overline{r}_{u,v}(n)$ according to Eq. 1.3.

$$r_{u,v}^{(\alpha)}(n) = e^{j\alpha n}.\overline{r}_{u,v}(n); 0 \le n < M_{sc}^{RS} \tag{1.3}$$

where $u \in 0, 1, 2, ..., 29$ refers to 30 reference signal sequences of each sequence length; v: base sequence number within the group; M_{sc}^{RS} is the number of subcarriers in the reference signal. However, this DMRS considers only User equipments (UEs) with a single transmit antenna; α is a cyclic shift in a slot n_s given as $\alpha = 2\pi n_{sc}/12$ [10] where:

$$n_{cs} = (n_{DMRS}^{(1)} + n_{DMRS}^{(2)} + n_{PRS}(n_s)) mod 12 \tag{1.4}$$

Where the value of DMRS parameters $(n_{DMRS}^{(1)}, n_{DMRS}^{(2)})$ are given according to the table 5.5.2.1.1-2 in [10] and related to the cyclic shift parameter provided by a higher layer. $n_{PRS}(n_s)$ [10] is given by:

$$n_{PRS}(n_s) = \sum_{i=0}^{7} c(8N_{symb}^{UL}.n_s + i).2^i \tag{1.5}$$
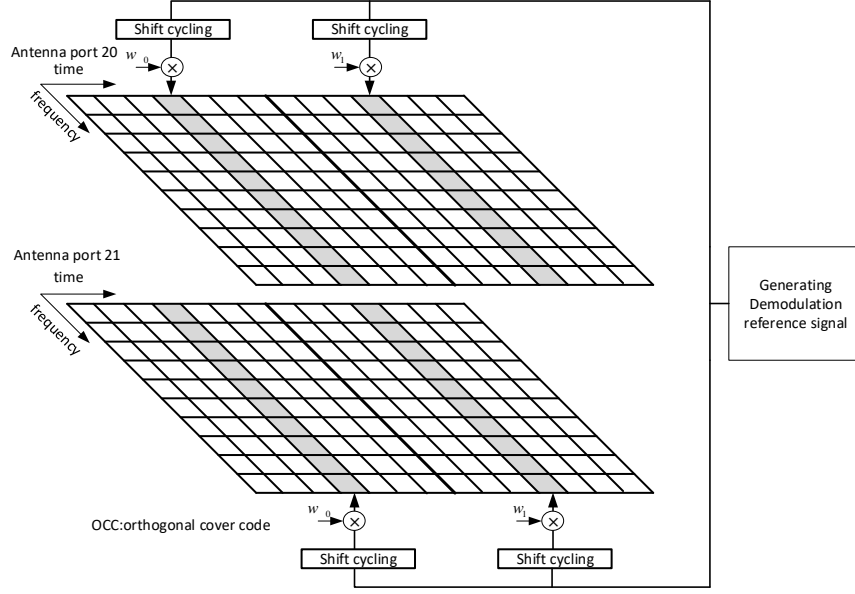
Fig. 1.4: Design of pilot pattern in a 2x2 MIMO SC-OFDM.

The demodulation reference signal sequence in LTE system $r^{PUSCH}(.)$ for PUSCH is defined by Eq. 1.6.

$$r^{PUSCH}(m.M_{sc}^{RS} + n) = r_{u,v}^{(\alpha)}(n) \tag{1.6}$$

To provide mechanisms of orthogonally multiple DMRS transmission in MIMO spatial multiplexing schemes, LTE Advanced defines DMRSs $r_{PUSCH}^{(\lambda)}(.)$ associated with layer $\lambda \in \left\{1, 2, ..., \lambda\right\}$ as shown in Eq. 1.7 [2].

$$r_{PUSCH}^{(\lambda)}(m.M_{sc}^{RS} + n) = w^{(\lambda)}(m).r_{u,v}^{(\alpha_\lambda)}(n) \tag{1.7}$$

The whole process of generating demodulation reference signals for two layers depicted in Fig. 1.4. If Eq. 1.6 is compared with Eq. 1.7, two main differences between DMRSs in LTE and LTE Advanced can be distinguished. The first one is the orthogonal sequence $w^{(\lambda)}(m)$ which is given by Table 5.5.2.1.1-1 in [2] and separates the generated DRMS signal in two slots of one subframe. The second one is n_{cs} generated by the equation 1.8 [2].

$$n_{cs}^\lambda = (n_{DMRS}^{(1)} + n_{DMRS,\lambda}^{(2)} + n_{PN}(n_s))mod12 \tag{1.8}$$

The main difference between equations 1.4 and 1.8 is the $n_{DMRS,\lambda}^{(2)}$ parameter which changes between layers to generate multiple orthogonal reference signals using different phase rotations (cyclic shifts).

1.2 D2D Communication in the LTE Advanced System

D2D communication [15, 16] is an important technology which enables the flow of data not only between humans but also between machines without human intervention. Therefore, D2D communication can be used underlying the cellular networks. The 3GPP LTE advanced technology has been shown to have high performance in spectral efficiency and throughput measurements. LTE Advanced is one of the suitable environments for D2D communication since it is an IP-based network that enables the control of any connected devices using internet protocols. Moreover,
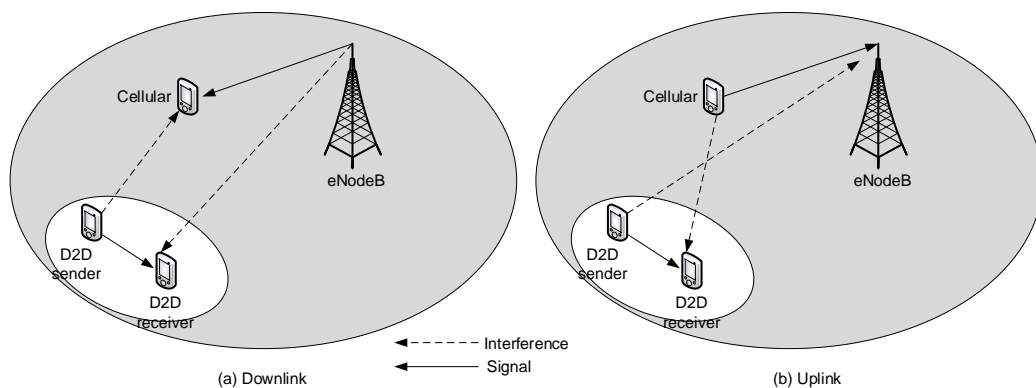
Fig. 1.5: Interference scenarios in cellular network based on D2D communication [17].

it is able to send large amounts of data with high rate and low latency. It is a good solution to reduce the evolved NodeB (eNodeB) traffic load and the end to end delay. However, implementation of D2D communication into cellular systems causes interference between D2D and eNodeB relaying UEs. Interference reduces total cell capacity. Figure 1.5 depicts the interference scenarios in cellular networks with D2D communication. In Fig. 1.5(a), signals transmitted by eNodeB to cellular UEs may cause interference to a D2D receiver. Also, channel quality of eNodeB relaying UEs on downlink can be degraded due to a signal transmitted from a D2D sender [17, 18]. Figure 1.5(b) shows the interference scenario for uplink transmission in a cellular network. In this case, eNodeB and D2D receivers may be interfered by a signal transmitted from a D2D sender and eNodeB relaying UE, respectively.

There are several key mechanisms to mitigate interference among LTE Advanced networks and D2D communication users. The main mechanisms will be mentioned in the next sections.

1.2.1 Mode Selection

In order to achieve an efficient communication system and maximize throughput, four UE operating modes are suggested [8].

- **D2D Silent Mode**: This happens when there is no available dedicated resources for D2D communication. In other words, devices which are a part of D2D communication are incapable of data transmission, "they have to stay silent". Allowing D2D communication will cause harmful interference.
- **D2D Reuse Mode**: D2D communication is possible by reusing uplink or downlink resources of the cellular network.
- **D2D Dedicated Mode**: D2D communication can be done using dedicated cellular spectrum resources. The advantage of this mode is easy interference management. There is no interference between D2D and cellular network users. The disadvantage is inefficient bandwidth utilization to maximize the overall network throughput.
- **D2D Cellular Mode**: D2D communication happens by transmitting their traffic through the base station.

One of the main issues in D2D communication is how to select the optimal transmission mode for D2D links so that the overall network throughput is maximized and the QoS requirements of the communication links are satisfied.

A paper on D2D communication [19] focuses on the location relationship between cellular UE and D2D UEs. It proves that whether D2D communication can reuse the cellular uplink resource or not, it is affected by system parameters. The achieved results show that the reuse mode is preferred when the cellular user is closer to the base station (BS) or relay node (RN) than to the D2D user. In [20],the authors proposed a tractable hybrid network model and discussed its performance in two different cases (overlay and underlay cases). The overlay case is when D2D users have their own dedicated spectrum. Underlay is a more flexible case where D2D users choose between communicating directly or via the base station; the choice depends on the distance between the potential D2D transmitter and the receiver. The underlay case results show that the rate of D2D users is resource-limited and its linear increase can be caused by a linear increase in the spectrum resource. Also, the rate of D2D users is more co-channel cellular interference limited in overlay. Whereas cellular users are sensitive to spectrum reduction in overlay but is more robust against the co-channel D2D interference in underlay.

1.2.2 Power Control and Distributed Resource Allocation

In order to provide a high rate and a high quality hybrid communication network for a large number of users, power control is one of the key mechanisms that should

be considered. Transmitting power should be allocated to satisfy QoS requirements (e.g. Signal-to-interference-plus-noise ratio (SINR)) for all users inside the cell. Applying this mechanism improves spectrum utilization, and as a result the capacity and throughput all over the cell will be improved. Power control is a key research issue for D2D communication which has been considered by various researchers. In [21], a simple power control method for D2D communication which constrains SINR degradation of the cellular link to a certain level is considered. A simple transmit power reduction method for D2D users is proposed. The transmit power of D2D users is reduced so that the cellular user SINR degradation is 3 dB compared to the cellular user Signal-to-noise ratio (SNR) at 5 percentile outage probability. Paper [22] proposes a hybrid method for efficient D2D communication. The proposed method encompasses mode selection, resource allocation, and power control within a single framework. According to the distance between D2D users, the method prioritizes the D2D dedicated mode.

Another paper [23] developed centralized and distributed power control algorithms. Centralized power control ensures that the cellular users have sufficient SINR levels while D2D links increase. The distributed power control method maximizes the sum rate of the D2D links by applying the optimal ON/OFF power control strategy. This means each D2D transmitter chooses its transmit power to maximize its own rate towards its intended receiver, disregarding the interference caused to others. The outputs of the research show that the centralized power control approach improves throughput, meanwhile, the distributed power control approach is not capable of guaranteeing reliable cellular links.

In [24], an optimization method is proposed to maximize the sum rate of both cellular and D2D users which can use the same sub-channels while satisfying the rate requirements of all cellular users. Another algorithm is proposed by [25] to solve channel allocation and the power control problem for both cellular and D2D users. This algorithm maximizes the weighted sum rate (WSR) of D2D pairs while guaranteeing the minimum throughput of all cellular users in a D2D underlay cellular network. D2D users are allowed to reuse all the uplink cellular sub-channels.

1.2.3 Cooperative Communications

Cooperative spectrum sensing is a promising wireless technology to prevent harmful interference and improve the detection performance of D2D communication. D2D users can cooperate in transmitting data to identify the available spectrum, utilize it efficiently, reduce interference levels, and enhance the overall network throughput. The main idea of cooperative sensing is to enhance sensing performance by exploiting the spatial diversity in the observations of spatially located users. By co-

operating, users can share their sensing information for making a combined decision more accurate than the individual decisions. More information about cooperative spectrum sensing and its methods are described in chapter 4.

1.2.4 Interference Cancellation

Interference cancellation is one of the important ways of achieving better capacity and throughput in a cellular system. Therefore, various schemes of frequency reuses are adopted for optimizing the use of the spectral resource. All these schemes are used to guarantee the minimum QoS requirements of D2D communication. Several researches are involved in improving QoS of D2D communication. The authors in [26] proposed a resource allocation scheme for intracell D2D to DL and UL to D2D interference mitigation. In the case of using D2D transmission, the output shows a 2.3 fold increase of median cell capacity compared with the cell capacity when traffic is forwarded through the base station. Compared to random resource allocation, 4.7 dB gain in the 10th percentile of the downlink SINR is achieved. A Greedy Heuristic algorithm is proposed by [27] to solve the problem of radio resource allocation to D2D users. The number of D2D connections is constant (20% of the cell UEs). The results show that cell throughput is higher in the case of using the heuristic algorithm compared with the random algorithm resource allocation. In the case of 30 active UEs per site, normalized cell throughput is 7% higher in the case of the heuristic algorithm than the random algorithm. Resource allocation and interference avoidance issues for D2D communication are also described by [28].The mechanism of sharing the uplink spectrum with a cellular network in a hybrid system is addressed. The authors in [29] also analyzed the interference in a hybrid network that consists of D2D communication and conventional cellular connections. They proposed a time hopping (TH) based radio resource allocation scheme to improve the robustness of the hybrid network. More information about different kinds of interference mitigations are depicted in chapter 3.

1.3 Software Defined Radio

SDR [30]: is a radio communication system which uses software on different PC platforms to perform different hardware functions (e.g. mixers, filters, amplifiers, modulators/demodulators, detectors, etc.). It consists of a configurable radio frequency (RF) front end with a programmable system-on-chip (SoC) to perform digital functions. It helps to develop flexible, inexpensive, cost efficient and easy-to-use communication systems. Currently, there are a variety of different hardware and

software which are usable for SDR system implementation. Fig 1.6 [30] depicts the concept of SDR.
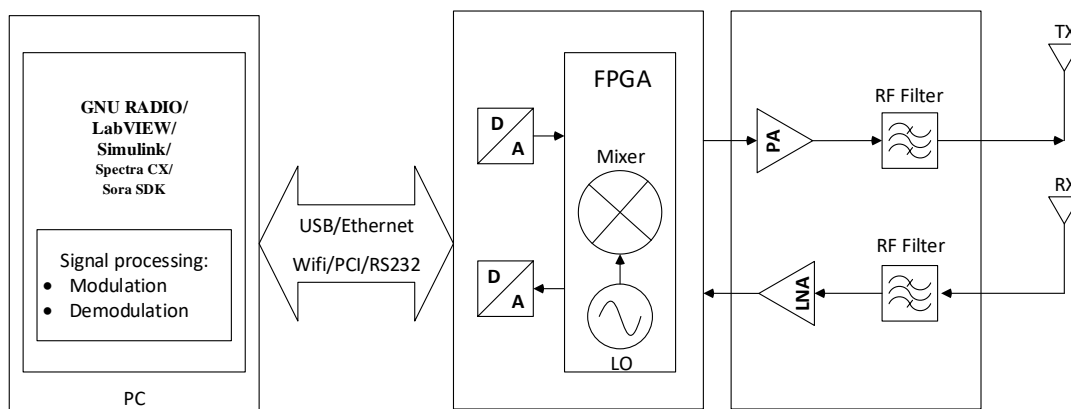
Fig. 1.6: Basic SDR system architecture [30].

At the transmitter side, the signal is generated. That's done using different programs on a Personal computer (PC). According to an SDR system, various signal processing methods can be created using GNU RADIO, LabVIEW, Simulink, Spectra CX, and Sora SDK. The output is a signal in digital domain. The next step is converting the signal to analog domain using a Digital to Analog Convertor (DAC). The analog signal is passed to the signal processing circuit, often FPGA (Field Programmable Gate Array), where the Digital UP Converter (DUC) takes place. Afterwards, the signal is amplified using a power amplifier (PA), then filtered and transmitted.

At the receiver end, the signal is picked up by RX antennas, filtered, and then amplified with a Low Noise Amplifier (LNA). LNA is an amplifier which amplifies a very low-power signal without significantly degrading its signal to noise ratio. Afterwards, the signal is mixed with a Local Oscillator (LO) and converted to an Intermediate Frequency signal. Then the Analog to Digital Convertor (ADC) digitizes the signal and passes it to the baseband processor for further processing; demodulation, channel coding, and source coding.

1.3.1 SDR Platforms

The most commonly used SDR platform is USRP, developed by Ettus Research [31]. The USRP in conjunction with the GNU Radio is a very powerful tool designed for RF applications from 0 to 6 GHz including MIMO systems. It supports up to

160 MHz bandwidth. FMCOMMS5-EBZ [32] Analog Devices are high-speed analog modules designed as a high performance, highly integrated RF agile transceiver intended for use in RF applications. It is a software tunable device across a wide frequency range (70 MHz to 6.0 GHz) with a channel bandwidth of 200 kHz to 56 MHz. FlexRIO [33] offers a flexible and integrated hardware and software solution for rapidly prototyping high-performance wireless communication systems. It consists of a tunable RF transceiver covering 200 MHz to 4.4 GHz up to 200 MHz real-time bandwidth with 80 dB of dynamic range. Spectra DTP4700 [34] is a wideband full duplex RF transceiver which uses SDR development and a test platform. It can support a signal with 40 KHz to 40 MHz bandwidth and up to 20MSps. It is available in either 30 MHz to 1.6 GHz (DTP4700L) or 400 MHz to 4 GHz (DTP4700H) TX/RX frequency range configurations.

Microsoft Research Software Radio (Sora) [35]: it is a Software Defined Radio platform proposed for wireless signal processing functions using wireless standards including WiFi and LTE. It is able to operate on 802.11 a/b/g/n in full data rate, up to 40 MHz channel, up to 64QAM, up to 4x4 MIMO, on both 2.4 GHz and 5 GHz bands. It is able to accomplish 802.11 data rate up to 300 MSps. The Thunder SDR System [36] is a high performance fully-functional, and a reconfigurable radio development platform from DataSoft. It provides adjustable, independent transceivers for RF signal bandwidths covering 40 KHz to 40 MHz with sample rates from 2.4 KSps to 100 MSps. It operates on frequencies 400 MHz to 4000 MHz and 30 MHz to 1600 MHz. Because of availability and the low cost of USRP developed by Ettus Research compared with the above mentioned SDR, it is considered for spectral monitoring and RF recording. This equipment will be used with the GNU Radio software framework.

1.3.2   Universal Software Radio Peripheral

USRP can be described as an interface between the digital host and the analog domain RF. There are different series of USRPs. USRP1 [37] with an Altera Cyclone FPGA contains four 64 MSps 12-bit analog to digital converters, four 128 MS/s 14− bit digital to analog converters, high-speed USB 2.0 interface (480 Mbps), fully coherent multi-channel systems (MIMO capable) and auxiliary analog and digital I/O support complex radio controls such as RSSI and AGC. It is able to process a signal up to 16 MHz bandwidth. USRP2 [38] with a Xilinx Spartan $3 - 2000$ FPGA consists of two 100 MSps 14-bit analog to digital converters, two 400 MSps 16-bit digital to analog converters, Gigabit Ethernet Interface, 2 Gbps high-speed serial interface for expansion, auxiliary analog and digital I/O support complex radio controls such as RSSI and AGC and 1 Megabyte of on-board high-speed SRAM.

It is able to process a signal up to 100 MHz bandwidth. It supports the MIMO technique up to 8 antennas. There are two types of USRPN series [39], USRPN200 and USRPN210. USRP$N2X0$ consists of a Xilinx Spartan 3A-DSP1800 FPGA. USRP$N2X0$ has the same capability as USRP2. In addition, it contains an internal Global Positioning System (GPS) Disciplined Oscillator (GPSDO) that improves both frequency accuracy and enables global synchronization and position location using GPS.

In order to provide a flexible, fully integrated RF front-end, a daughterboard should be mounted to the above mentioned USRPs. There are a variety of available daughterboards which are used for different applications and frequencies. Tab. 1.2 [40] presents these boards and their specifications. All of the above describes the hardware part of SDR. However, the main value of SDR is its software which can replace the missing hardware. Using software instead of hardware reduces manufacturing costs as well as maintenance time, by making the system more flexible and efficient. This part of signal processing is done by the GNU Radio or other different programs. GNU Radio is an open source software toolkit which uses Python and $C++$ as the main programming languages [41]. It runs under several operating systems like Linux, Mac OS X, NetBSD, Windows XP [31]. It provides a library of signal processing blocks for developing Software Defined Radio. It is possible not only to create a structure of different connecting signal processing blocks but also to program custom blocks using $C++$ and Python. Although SDR has a lot of advantages, it has several disadvantages. These disadvantages are due to hardware limitations like LNA bandwidth, ADC/DAC dynamic range, and sampling rates.

Tab. 1.2: Universal Software Radio Peripheral daughterboards

Daughterboard	Operating Frequencies	Bandwidth	Ports
BasicRX	1 - 250 MHz	250MHz	RX-A, RX-B
BasicTX	1 - 250 MHz	250MHz	TX-A, TX-B
LFRX	0 - 30 MHz	30 MHz	RX-A, RX-B
LFTX	0 - 30 MHz	30 MHz	TX-A, TX-B
TVRX/ TVRX2	50-860 MHz	6MHz/1.7, 6, 7, 8, 10 MHz	2 RX
DBSRX/ DBSRX2	800-2300 MHz	8-66 MHz/ 8-80 MHz	RX
WBX/ WBX120	50-2200 MHz	40 MHz/ 120 MHz	TX/RX, RX2
RFX400	400-500 MHz	40 MHz	TX/RX, RX2
RFX900	750-1050 MHz	40 MHz	TX/RX, RX2
RFX1200	1150-1450 MHz	40 MHz	TX/RX, RX2
RFX1800	1.5-2.1 GHz	40 MHz	TX/RX, RX2
RFX2400	2.3-2.9 GHz	40 MHz	TX/RX, RX2
XCVR2450	2.4-2.5 GHz 4.9-6.0 GHz	RX: 15, 19, 28, 36 MHz TX: 24, 36, 48 MHz	J1(TX/RX) J2(TX/RX)
SBX/ SBX-120	400 MHz-4.4 GHz	40 MHz/ 120 MHz	TX/RX, RX2
CBX/ CBX-120	1.2 GHz-6 GHz	40 MHz/ 120 MHz	TX/RX, RX2
UBX/ UBX-160	10 MHz-6 GHz	40 MHz/ 160 MHz	TX/RX, RX2

2 PHYSICAL UPLINK LAYER OF THE LTE ADVANCED SYSTEM

LTE Advanced standard (Release 10) [2] is the next major milestone in the evolution of LTE (Release 8) [10]. The difference between LTE and LTE Advanced is described in chapter 1. This chapter evaluates LTE Advanced system performance. Therefore, the structure of the previously described LTE Advanced transmitter and receiver, with all signal processing stages, is implemented in MATLAB. The generated signal is transmitted over different ITU channels [42]. In the receiver, the transmitted signal is recovered. Channel estimation and signal detection cooperate together to recover the transmitted signal with minimum interference. These techniques should be taken into consideration for the receiver design. The main contributions of this chapter are described in the following few points:

- Test the ability of the LTE Advanced 2×2 uplink physical layer implementation and its evaluation using different channel models, and channel estimation and signal detection techniques.
- BER and throughput evaluations by considering fading channels (Flat Rayleigh, pedestrian A (Ped A) and vehicular A (Veh A)), modulations (64QAM, 16QAM, and 4QAM), channel estimation (least square (LS) and approximate linear minimum mean square error (ALMMSE)) and signal detection techniques (zero forcing (ZF) and soft sphere detection (SSD)).

As an output, the achieved results of performance evaluation in terms of the BER and throughput are depicted. The performances of the LTE Advanced system using the different combinations of channel estimation and signal detection (LS_ZF, ALMMSE_ZF, LS_SSD, or ALMMSE_SSD) in different channel models (Flat Rayleigh and Ped A, Veh A) are compared. The performance values of both Rayleigh and Ped A, are approximately the same when SNR is lower than 28 dB for Channel Quality Indicator (CQI) = 15, lower than 25 dB for CQI = 9 and lower than 17 dB for CQI = 6. It can be observed that in the case of CQI = 15, the lowest BER and the highest throughput are achieved using the combination of ALMMSE and SSD for all studied channels (Flat Rayleigh, Ped A and Veh A). LTE Advanced uplink with (2x2) MIMO outperforms LTE uplink throughput by 98% in Flat Rayleigh and a percentage decrease up to 45% for a more complex channel (Veh A). The throughput improvements are achieved for SNR values greater than 24 dB, 34 dB, 14 dB, and 9dB for Flat Rayleigh/Ped A with 64QAM modulation, Veh A with 64QAM modulation, Flat Rayleigh/Ped A with 16QAM modulation, and Flat Rayleigh/Ped A with 4QAM modulation settings, respectively. More detailed results are presented in this chapter.

This chapter is divided into five sections. It starts with a brief overview about the used radio channels. Then the outlines of channel estimation and signal detection techniques are described. Afterwards, the properties of the implemented system are explained. Finally, the achieved results of performance evaluation in terms of BER and throughput are depicted.

The **Author's bibliography related to this chapter:**

[1] Kasem, E., & Prokopec, J. (2012). The evolution of LTE to LTE-Advanced and the corresponding changes in the uplink reference signals. *Elektrore-vueEng*, ISSN: 1213–1539.

[2] Kasem, E., & Prokopec, J. (2013) Evolution of physical uplink channels in LTE-advanced. *ElektrorevueEng*, ISSN: 1213–1539.

[3] Kasem, E., Marsalek, R., & Blumenstein, J. (2013). Performance of LTE Advanced uplink in a Flat rayleigh channel. *Advances in Electrical and Electronic Engineering*, vol. 11 no. 4, pp. 266–274.

[4] Kasem, E., & Marsalek, R. (2013). The Performance of LTE Advanced Uplink in Flat Rayleigh and Pedestrian Channels. *ElektrorevueEng*, vol.4, no. 3, ISSN: 1213–1539.

2.1 Radio Channels Overview

A radio channel is a part of the communication link between the TX and the RX that carries information in the form of electromagnetic waves. The radio channel is commonly characterized by scattering, attenuation, reflection, refraction and fading [43]. Studying radio channels helps us make an idea about rapid fluctuations of radio signal amplitude over a period of time. In this section, slow fading channels (Block fading) are considered. These kinds of channels keep the same value of attenuation during the whole subframe. Therefore, ITU channel models like Flat Rayleigh, Ped (A,B), and Veh (A,B) are presented.

The **_Flat Rayleigh fading channel_** is the simplest Rayleigh channel which is used for narrowband transmissions over wireless and mobile communication channels. It is called flat because it has a constant attenuation factor during the subframe time and the whole allocated bandwidth, as shown in Fig. 2.1.

Ped and Veh A and B channels are other commonly used channel models. These channel models are specified in the ITU recommendation [42]. These models define two different test environments: outdoor to indoor pedestrian and vehicular high antenna. In both the Ped and Veh channels, A and B letters refer to low and medium delay spreads. For each of these cases, the multipath tap delay model is specified. Moreover, the impulse response (h) of the multipath channel can be
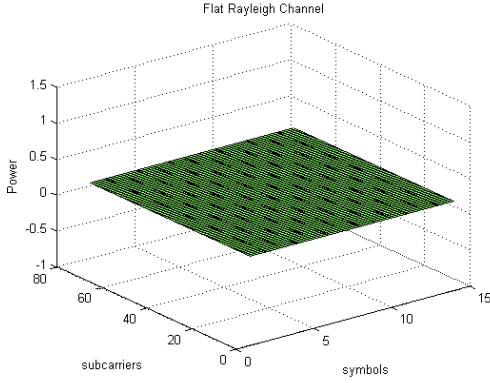
Fig. 2.1: Flat Rayleigh channel charac-
teristics. Source: author.
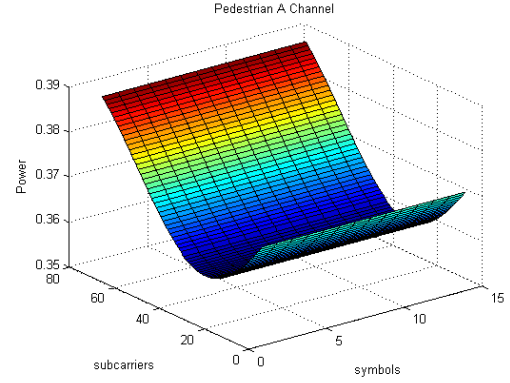
Fig. 2.2: Pedestrian channel character-
istics. Source: author.
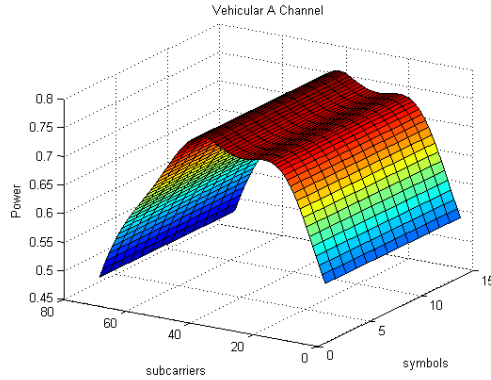
Fig. 2.3: Vehicular channel characteristics. Source: author.

presented according to Eq. 2.1 where a_w , τ_w, and φ_w represent the amplitude, arrival time, and phase, characterizing N_p number of individual paths between the transmitter and receiver [42] [44].

$$h(t, \tau) = \sum_{w=1}^{N_p} a_w(t)\delta(\tau - \tau_w(t))e^{-j\varphi_w(t)} \qquad (2.1)$$

Pedestrian channel models define the environment for indoor and outdoor users, where the indoor coverage is provided by the outdoor eNodeB. The multipath delay profile of this channel is shown in Tab. 2.1[45]. Figure 2.2 depicts the simulation of the Ped A channel matrix. *Vehicular channel models* are well-established empirical channel models used for research purposes in mobile communication systems. Moreover, these models help us to simulate the specification of channel conditions for various operating environments. The simulation of the vehicular channel model is shown in Fig. 2.3. It depicts approximately temporal dispersion of the time-variant wireless propagation channels. The tapped-delay-line parameters and other

Tab. 2.1: ITU channel models.

Tap	Channel A				Channel B			
	Relative delay (ns)		Average power (dB)		Relative delay (ns)		Average power (dB)	
	Ped	Veh	Ped	Veh	Ped	Veh	Ped	Veh
1	0	0	0	0	0	0	0	-2.5
2	110	310	-9.7	-1.0	200	300	-0.9	0
3	190	710	-19.2	-9.0	800	8900	-4.9	-12.8
4	410	1090	-22.8	-10.0	1200	12900	-8.0	-10.0
5	-	1730	0	-15.0	2300	17100	-7.8	-25.2
6	-	2510	0	-20.0	3700	20000	-23.9	-16.0

properties for ITU-R Vehicular channels are shown in Tab. 2.1 [45].

In the case of transmitting the signal over all previous mentioned channels, the received signal can be calculated using Eq. 2.2

$$y = h * x + n \tag{2.2}$$

where n is Gaussian noise and y, x, h are received and transmitted signals in time domain and channel impulse response, respectively.

2.2 Channel Estimation Techniques

Channel estimation is one of the fundamental approaches which should be taken into consideration for LTE Advanced system design. Channel estimation and signal detection are essential solutions to recover the transmitted signal with minimum interference. Channel estimation uses superimposed training sequences or pilot symbols to calculate the channel matrix. In this research, DMRS is used as a pilot sequence for channel estimation. There are different techniques of channel estimation; two of them will be presented.

As previously described, the pilot symbols are inserted periodically over the whole bandwidth. Therefore, block type pilot based channel estimation is an appropriate estimation method for the physical uplink signal in the LTE Advanced system. A lot of researches in channel estimation use LS and minimum mean square error (MMSE) as the main estimation techniques. In [46], a time domain channel estimation of OFDMA systems is discussed. The differences between LS and

MMSE are compared in terms of complexity and performance. The results show that the complex MMSE estimator, which requires a prior knowledge of noise variance and channel covariance, for 16QAM signal, provides a gain up to 4 dB over the LS estimator. [47] research is involved in LS and linear minimum mean square error (LMMSE) channel estimations which are performed on systems with different pilot arrangements. Channel estimation based on block type and comb type pilot arrangements are used. The output is presented as a BER performance of 16QAM, QPSK, DQPSK and BPSK as modulation schemes in multipath Rayleigh fading and AR based fading channels. Other various studies are also performed on MIMO OFDMA systems and used LS and MMSE as an estimation technique [48] [49] [50] [51].

In this section, two typical approaches of channel estimation are used for block type pilots [52], known as LS and ALMMSE [53, 54].

2.2.1   Least Square

The LS channel estimation is the simplest technique of channel estimation characterized by low complexity. It estimates the channel response by computing the division between received and transmitted symbols. The drawback of this approach is that the estimated symbols suffer from a high mean square error. This algorithm minimizes $\left\| X.H_{est} - Y \right\|^2$ which describes the distance between the received signal before and after the estimation. Y is a frequency domain received pilot signal; X is a frequency-domain transmitted pilot signal; H_{est} is a frequency domain estimated channel matrix. After proving this condition, the LS obtained channel estimation algorithm is based on Eq. 2.3 [53]:

$$H_{est} = H_{LS} = (X^H.X)^{-1}.X^H.Y \tag{2.3}$$

2.2.2   Approximate Linear Minimum Mean Square Error

The ALMMSE estimator gives better results than the LS estimator regarding mean square error. The advantage of this technique is better performance of MIMO systems in low SNR environments. This technique gives less complexity than LMMSE and approximately the same performance. One of the ways used for reducing LMMSE complexity is to reduce the size of the correlation matrix R_{h_p,h_p}. This can be achieved by dividing the channel vector into M sub-vectors of length L ($M = N/L$, where $L << N$ and N is the length of the channel vector). More information about ALMMSE can be found in [55, 56]. However, ALMMSE estimation is more complex than the LS technique.

This algorithm minimizes $minE\left\{\left\|H - H_{est}\right\|\right\}$ which describes the distance between the received signal before and after the estimation. After proving this condition, the ALMMSE channel estimation algorithm can be calculated based on Eq. 2.4 [54].

$$H_{est} = H_{ALMMSE} = R_{h,h_p}(R_{h_p,h_p} + \frac{\sigma_w^2}{4}.I)^{-1}.H_{LS} \qquad (2.4)$$

where R_{h_p,h_p} the is the auto-correlation matrix of the channel at the pilot symbols position and R_{h,h_p} is the cross correlation matrix between the channel at the data symbol positions and the channel at the pilot symbol position. Now for the case of the block-type pilot channel estimation $R_{h_p,h_p} = R_{h,h_p}$, Eq. 2.5 can be modified as:

$$H_{est} = H_{ALMMSE} = R_{h_p,h_p}(R_{h_p,h_p} + \frac{\sigma_w^2}{4}.I)^{-1}.H_{LS} \qquad (2.5)$$

2.3   Signal Detection Techniques

After estimating the channel and calculating the approximate value of the channel matrix, the transmitted signal should be recovered. This operation is done using one of the signal detection techniques.

There are a lot of studies involved in implementing various types of signal detection techniques. In [57], the performance of the low complexity ZF detector is evaluated. The multi-user MIMO system with user scheduling is considered. MMSE is another signal detection technique. The performances of MMSE and ZF techniques in addition to MMSE equalization with and without decision feedback (DF) are compared in [58]. The output shows that the performance of the MMSE detector is better than the corresponding ZF detector. As well, the performance of MMSE with decision feedback is better than MMSE without DF. Maximum Likehood Detection (MLD) is the mathematically optimal method used for channel recovery. It calculates the Euclidean distance of the received signal and the product of transmitted signal and the channel matrix. Its receiver has very high computational complexity. The performance of MLD in a wireless MIMO antenna system is evaluated in [59]. Vertical Bell Laboratories layered space time (VBLAST) is also a detection algorithm which is studied in [60] [61] [62]. The VBLAST algorithm decodes the strongest signal then subtracts it from other received signals in order to decode them. It works with MIMO systems. In [63], the authors compare combined methods of ZF-MLD and VBLAST algorithms. BER results show that a simplified combined ZF-MLD method provides good results as a complex MDL method which outperforms even the VBLAST method. The Sphere Decoding algorithm is another type of decoding method. This algorithm seeks to achieve the performance of the

Maximum Likelihood Detector with reduced complexity. It uses the same Euclidean distance (ED) of MLD as a metric of signal detection. However, it considers only a mall set of transmitted vectors within a given sphere rather than all possible transmitted signal vectors. The sphere decoding algorithm and a lot of improvements on it are presented in [64] [65] [66]. In this section, ZF and SDD are evaluated.

2.3.1 Zero Forcing

ZF detection is the simplest signal detection technique. The detection matrix G is given by the pseudo-inverse of H_{est}. The disadvantage of this technique is that it does not take into account the correlation of the transmitter (user equipment) and the receiver (eNodeB), so it has the highest error calculation. It cannot totally remove inter-stream interference. ZF is less complex compared to the other techniques. More information about ZF can be found in [67].

2.3.2 Soft Sphere Detection

The main goal behind the SSD algorithm is to reduce the number of candidate symbol vectors during the codeword search. It is more complex than ZF, but it gives better performance results. More information about SSD can be found in [68] [69] [70]

2.4 Testbed Description

The system was implemented by modifying the LTE uplink link level simulator developed at the Institute of Communications and Radio Frequency Engineering (INTH- FT), the Vienna University of Technology [71]. The LTE uplink link level simulator is a one layer simulator. The structure of its transmitter corresponds to the blue blocks in Fig. 1.1. The transmitter generates the data for given CQIs [72, 73], SNR and the number of subframes. CQI is an indication of channel quality experienced by cellular users. Each CQI value of all sixteen combinations represents the corresponding modulation scheme and coding rate. It gives us two kinds of information which are related to modulation order (4QAM, 16QAM, or 64QAM) and Effective Code Rate (ECR). In this case, a thousand data subframes were generated to get more accurate simulation results. This data is transmitted over the above described radio channel models. In the receiver, channel estimation and signal detection take place to retrieve the original transmitted signal. Then the signal is decoded to generate an acknowledgment (ACK/NACKs) that is sent back

Tab. 2.2: LTE Advanced system simulation parameters.

Parameters	*values*
Bandwidth	1.4MHz
FFT size (N)	128
Number of data subcarriers(N_{tot})	72
CP length	normal
Subcarrier spacing	15 kHz
Transmission setting	2×2
Channel model	Flat Rayleigh, Ped A, Veh A
Channel estimator	LS, ALMMSE
Detector	ZF, SSD
Channel quality indicator	6, 9, 15
Modulation schemes	4QAM, 16QAM, 64QAM

to the transmitter. In the original LTE uplink link level simulator [74], perfect channel knowledge is exploited and zeros are used instead of reference signals.

The modified version [75, 76] has the same basic structure of LTE uplink link level simulation. Several modifications are made to support the new features of LTE advanced. These modifications can be clearly described in both the transmitter and receiver. In the transmitter, two codewords instead of one are generated. Then two additional stages (layer mapper and pre-coding) are implemented to deal with two streams and two layers and receives the signal more efficiently. Afterwards, demodulation reference signals for LTE Advanced are generated. All features of the DMRS signal are taken into consideration. In the receiver, the reverse functions of the transmitter stages take place. Moreover, estimation and detection techniques are modified to allow the application of (2x2) MIMO. This modification can be summarized in received signal filtering for both antennas to extract two transmitted signals, separately. In other words, all the differences which are mentioned in Fig. 1.1 as white blocks are implemented in the LTE Advanced simulator.

Furthermore, LTE Advanced uplink performance in terms of UE throughput is presented. In this system [75, 76] two estimators (LS and MMSE) and detection techniques (ZF and SSD) are employed. Different combinations of channel estimation and signal detection techniques are applied to compare the performance of (2x2) MIMO and single input single output (SISO) systems. In order to verify the performance of the LTE Advanced system, different CQIs are used. For more details, the simulation parameters are summarized in Tab. 2.2.

2.5   Results and Discussion

The simulation results are described as a relation between BER or throughput and SNR. All the figures describe the BER and the throughput for different modulation schemes (QPSK, 16QAM and 64QAM) and different channel models (Flat Rayleigh, Ped A, and Veh A). Two different combinations of channel estimations (LS and ALMMSE) and signal detections (ZF and SSD) are used. The results of simulations
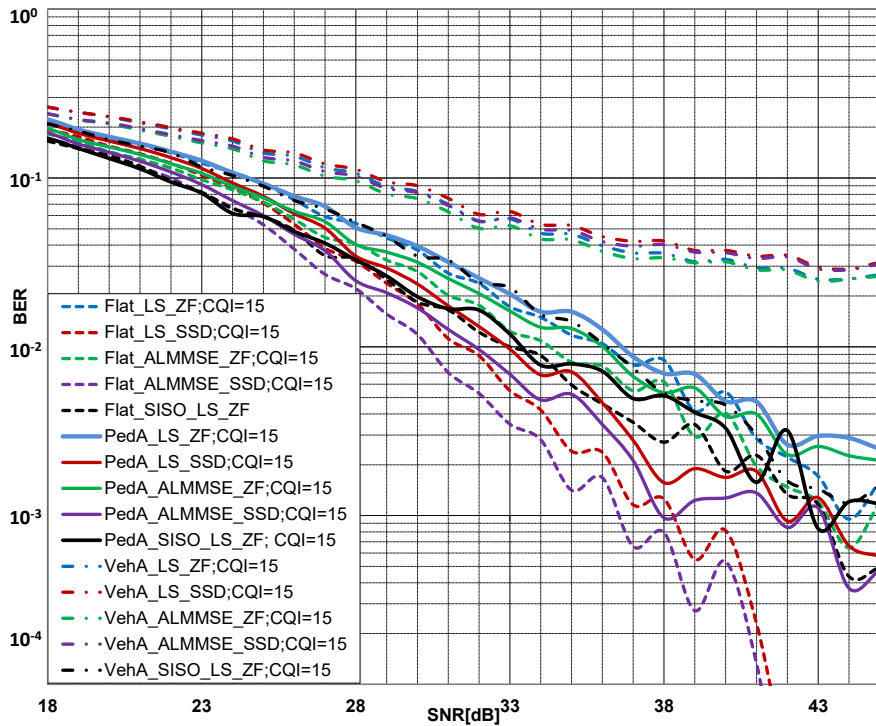
Fig. 2.4: BER curves using 64QAM modulation in Flat Rayleigh, Ped A and Veh A channels for different channel estimation and signal detection combinations. Source: author.

obtained with the modified LTE simulator supporting LTE Advanced features with parameters set up according to Tab. 2.2 are shown in Fig. 2.4 to Fig. 2.9. All the figures show that the best results are achieved when a combination of MMSE and SSD is used, but that makes the system more complex. For lower complexity but suboptimal results, other combinations can be applied.

Figures 2.4, 2.5 and 2.6 show BER results for different channel models. In other words, the figures describe the BER for Flat Rayleigh, Ped A and Veh A channel,
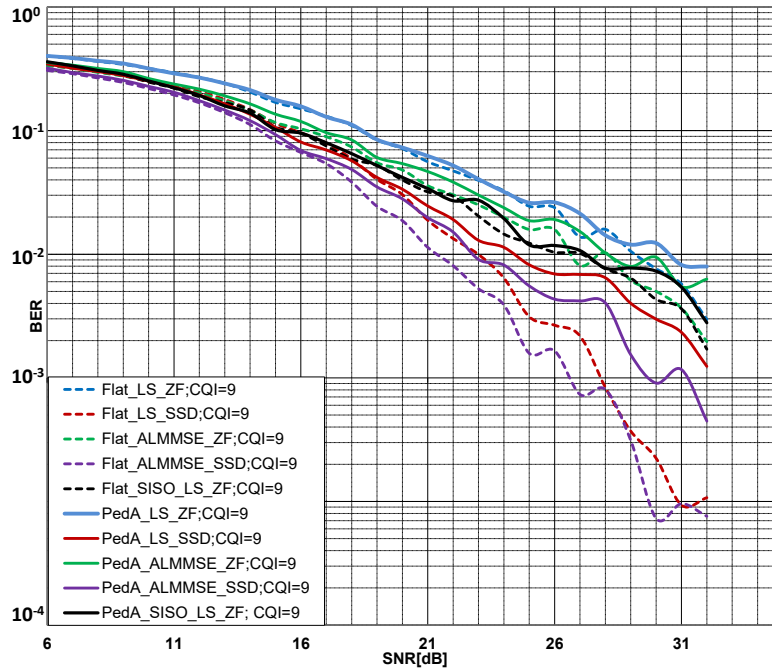
Fig. 2.5: BER curves using 16QAM modulation in Flat Rayleigh and Ped A channels for different channel estimation and signal detection combinations. Source: author.

respectively. These results are compared to uplink results presented in [74] and shown on the same figure. When the performances of the LTE Advanced system in three previous channels is compared, it can be distinguished that the best results are achieved in the Flat Rayleigh channel which is not such a realistic channel. The vehicular channel and pedestrian channel is more realistic but the performance is worse. The performance of the LTE Advanced system can be improved in pedestrian and vehicular channels using more complex channel estimation and signal detection techniques.

For example, in the Flat Rayleigh channel to achieve BER=2×10^{-2} the required SNR differs by approximately $2-3$ dB. Whereas in Ped A channel for the same BER value, the range of SNR is $1-2$ dB. The range of SNR values also depends on the used modulation schemes (64QAM, 16QAM, QPSK). If the performance of the LTE Advanced system using the same combination of channel estimation and signal detection (LS_ZF or ALMMSE_ZF) in different channel models (Flat Rayleigh and Ped A, Veh A) are compared, the performance of both Rayleigh and Ped A, is approximately the same when SNR is lower than 28 dB for CQI = 15,
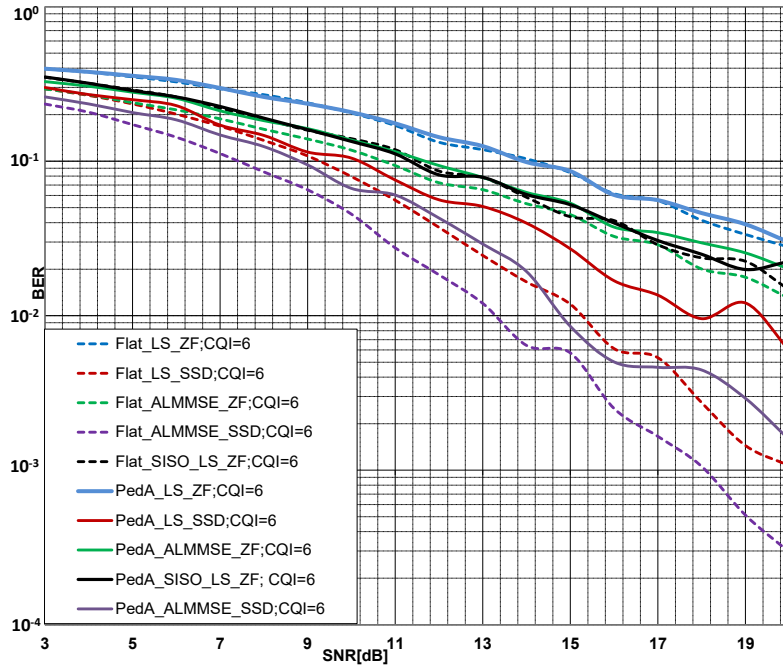
Fig. 2.6: BER curves using 4QAM modulation in Flat Rayleigh and Ped A channels for different channel estimation and signal detection combinations. Source: author.

lower than 25 dB for CQI = 9 and lower than 17 dB for CQI = 6. As can been observed, the best BER value for Flat Rayleigh, Ped A and Veh A channels can be achieved by applying an ALMMSE estimation technique and an SSD detection signal technique at the receiver. If the BER performance is compared between the mentioned channels for CQI = 15, the range of BER value differences can be observed as BER=1.3×10^{-2} to 5×10^{-4} , BER=6.9×10^{-2} to 3.1×10^{-2}, and BER=5.5×10^{-2} to 3×10^{-2} for Flat Rayleigh and Ped A, Flat Rayleigh and Veh A, and Ped A and Veh A, respectively. The overall achieved results from Fig. 2.4 show that BER performance is a little bit better for Flat Rayleigh than for Ped A. Whereas, Veh A channel shows the worst BER values in the case of all used signal estimation and detection techniques.

Figure 2.7, Fig. 2.8 and Fig. 2.9 present the throughput performance results as a function of SNR for different CQI values. As for the BER case, the black curves depict the LTE uplink throughput using a combination of LS and ZF techniques [74]. The other curves show the throughput of LTE Advanced system with various combinations of channel estimation and signal detection techniques. Apparently,
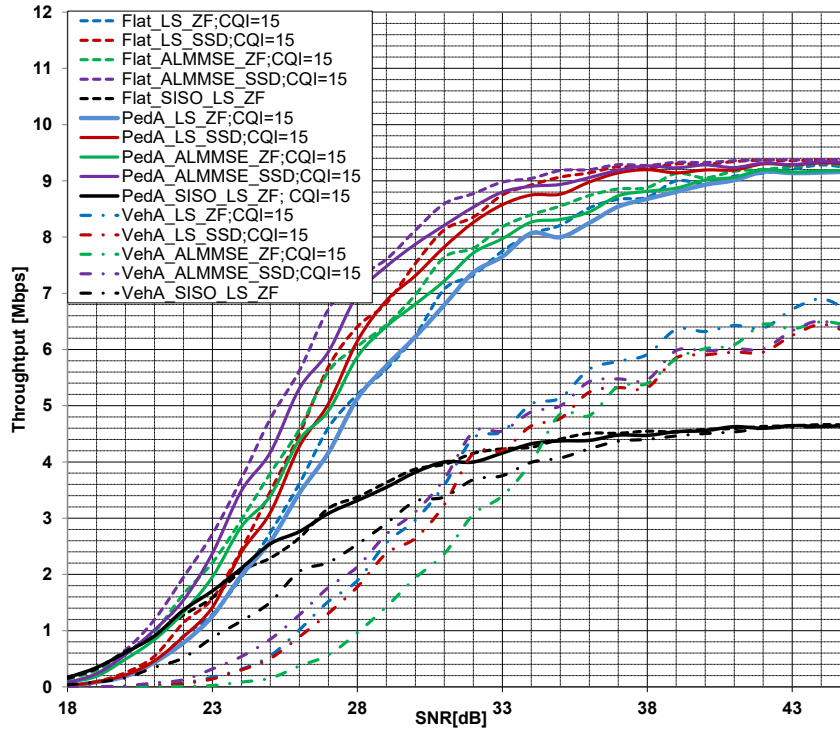
Fig. 2.7: Throughput curves with 64QAM modulation in Flat Rayleigh, Ped A and Veh A channels for different channel estimation and signal detection combinations. Source: author.

the achievable throughput increases with SNR.

The results for the CQI = 15 and thus 64QAM modulation are presented in Fig. 2.7. The ALMMSE estimator shows slightly better performance than the LS estimator especially for lower SNR conditions (below 24 dB). This SNR value also delimits the usefulness of the (2x2) MIMO modes in comparison with the SISO system. Figure 2.8 compares the LTE and LTE Advanced throughput performance for CQI = 9. A maximum value of 4 Mbps for SNR above 26 dB can be achieved. In the case of using the simple LS and ZF combination, the MIMO system should be enabled when SNR is above 14 dB in order to be beneficial. The throughput performance for CQI = 6 is illustrated in Fig. 2.9. In the case of 4QAM modulation (i.e. CQI = 6), and the combination of LS and ZF methods, the value of throughput for MIMO enabled surpasses the case of SISO for SNR higher than 9 dB. Other combinations of channel estimation and signal detection with MIMO transmission give
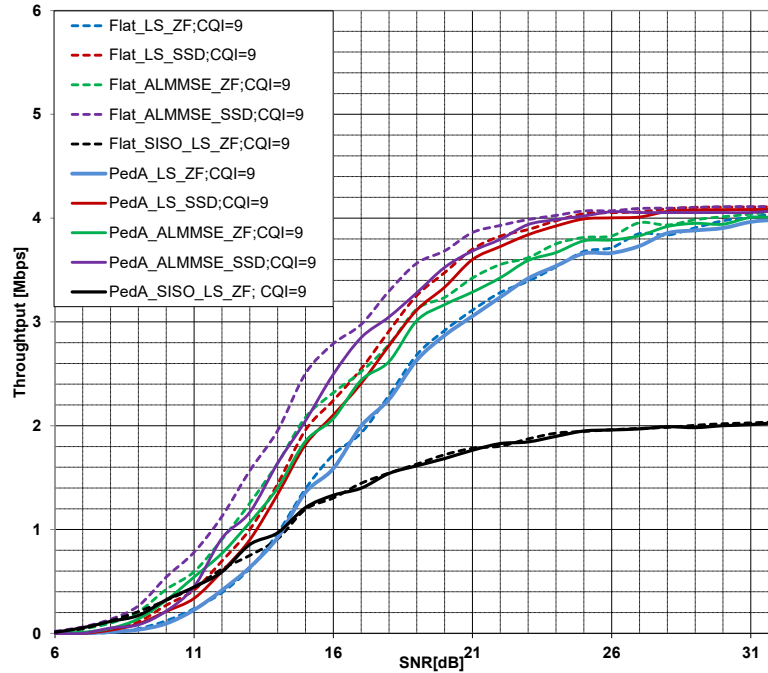
Fig. 2.8: Throughput curves using 16QAM modulation in Flat Rayleigh and Ped A channels for different channel estimation and signal detection combinations. Source: author.

us higher throughput performance than SISO with ZF and LS even for SNR equal to 3 dB. Above 18 dB for SNR, the LTE Advanced performance is approximately doubled compared with the LTE throughput.

2.6   Conclusion

In this chapter, the extension of the LTE Release 8 system by the (2 x 2) MIMO scenario of LTE Advanced is described. It concentrates on the result achieved by testing the implemented LTE Advanced uplink link layer. The implementation of all previous blocks for the transmitter, receiver and channel models are done using MATLAB codes. This simulator is a developed version of the Vienna LTE uplink level simulator. Different channels are used (Flat Rayleigh, Ped A, and Veh A channel models) to simulate the performance of the system with different CQI configurations. Two channel estimation and signal detection techniques are presented. The result contains BER and throughput performance. It shows the
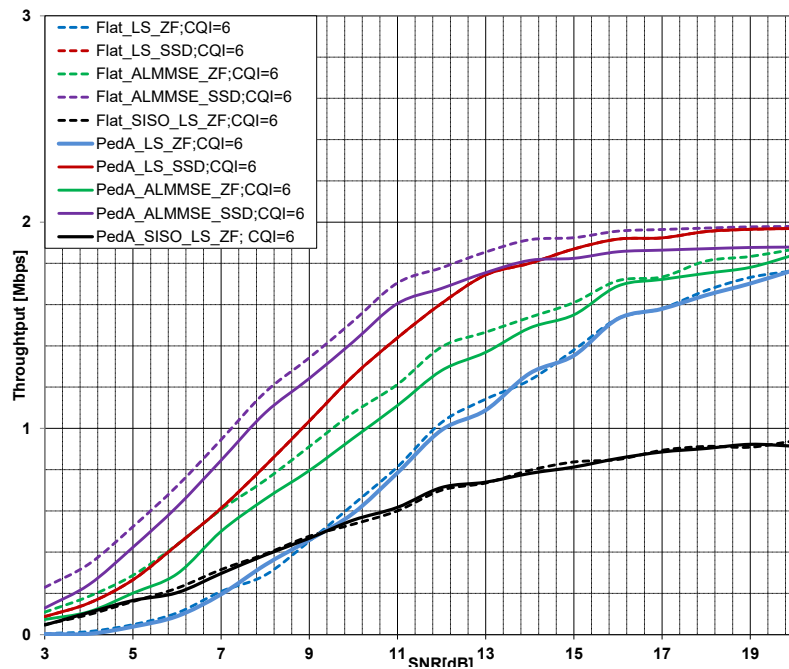
Fig. 2.9: Throughput curves using 4QAM modulation in Flat Rayleigh and Ped A channels for different channel estimation and signal detection combinations. Source: author.

superior performance of the (2 x 2) MIMO LTE Advanced system over the LTE with SISO configuration. It can also be observed that using the combination of ALMMSE channel estimation and the SSD signal detection technique will provide the system with the best performance. Depending on the combination of channel estimation and signal detection, the SNR threshold value can be determined. This threshold specifies the usefulness of implementing MIMO technology in the uplink layer of LTE Advanced systems.

3 INTERFERENCE MANAGEMENT IN LTE ADVANCED

One of the main important factors that affects the throughput performance in cellular system is Inter-cell Interference (ICI) [77]. To mitigate ICI, many frequency reuse schemes have been proposed. These schemes adopt frequency reuse as a key issue for optimizing the use of the spectral resource. They can be classified into three categories which include CCI cancellation [78], CCI randomization [79] and CCI coordination and avoidance [80, 81, 82].

The main contributions of this chapter are described in the following two points:

- FFR with three power levels method is suggested to be used as a CCI coordination and avoidance method for LTE Advanced systems. The normalized capacity densities of the cells and their regions are also derived.

- The relation between the overall and region capacities and the radius of each region are studied. Three different cases of user distribution (uniform distribution (UD), clustering to the base station (CBS) and clustering to the cell edge (CCE)) are considered.

As an output, the proposed scheme outperforms the results of the traditional Reuse-3 scheme. According to the presented capacity values and user density of the proposed method, the best radius of each region can be determined. This means that we are dealing with adaptive cells which are able to change the power of their regions depending on the users' spread density.

In this chapter, a brief overview of all mentioned ICI mitigation methods is presented. In order to support new technologies like D2D communication underlying the cellular network, new methods of ICI mitigation should be suggested. Therefore, Fractional Frequency Reuse with three power levels is proposed and its capacity performance is derived. Based on the SINR, the overall and region capacity values are extracted. The achieved results are compared with other methods and depicted in the fifth section. The last section concludes the chapter.

Author's bibliography related to this chapter:

[1] Kassem, E., Marsalek, R., & Blumenstein, J. (2016). On the capacity of fractional frequency reuse with three power levels for non-uniform user distribution. In *International Conference on Systems, Signals and Image Processing (IWSSIP)*, IEEE, pp. 1–5.

3.1   ICI Cancellation

The principle of the ICI cancellation techniques is to subtract the re-generated interfering signals from the desired signal. Various ICI cancellation techniques have been proposed in literature. An efficient ICI cancellation method termed as the ICI self-cancellation scheme for OFDM mobile communication systems is suggested in [83]. The work presented in this research concentrates on a quantitative ICI power analysis. The proposed self-cancellation method presents good BER results in the multipath radio channel. Another research [84] presents polynomial cancellation coding (PCC). They propose a mathematical context for PCC to reduce inter-carrier interference in OFDM.

3.2   ICI Randomization

In contrast to ICI cancellation, which tries to eliminate interfering signals in the received signal by canceling the dominant interference, ICI randomization averages interference across the data symbols of the data block or the whole frequency band. The ICI randomization can be achieved by scrambling, interleaving division multiple access (IDMA) and frequency hopping. A hybrid multiple access scheme for LTE uplink is proposed by [85]. SC-FDMA-IDMA combines IDMA and SC-FDMA. The achieved results are concluded as: SC-FDMA-IDMA performs better than OFDM-IDMA in PAPR for LTE uplink, and its BER performance is close to OFDM-IDMA. Various frequency hopping schemes for LTE uplink are described in [86]. The achieved results show that the localized transmission with frequency hopping can provide gain from 0.3 dB to 0.7 dB over localized transmission without frequency hopping.

3.3   ICI Coordination

This category consists of many different techniques which are ranged from conventional frequency reuse (CFR) (reuse-1 and reuse-3) to more efficient and complex techniques.

3.3.1   Conventional Frequency Reuse

CFR is the simplest scheme of frequency reuse. When the Frequency Reuse Factor (FRF) equals 1 [87], the frequency spectrum is reused in each sector with uniform power over the entire system bandwidth. This type of Frequency Reuse (FR) suffers from heavy interference from the neighboring cells. In order to decrease interference,

a CFR with FRF=3 [87] was suggested. In this case, the bandwidth is divided into 3 sub-bands; each of them is assigned to a cell. This scheme improves inter-cell interference, however, it suffers from inefficient use of the bandwidth and large capacity loss. Both schemes are depicted in Fig.3.1 and Fig.3.2.
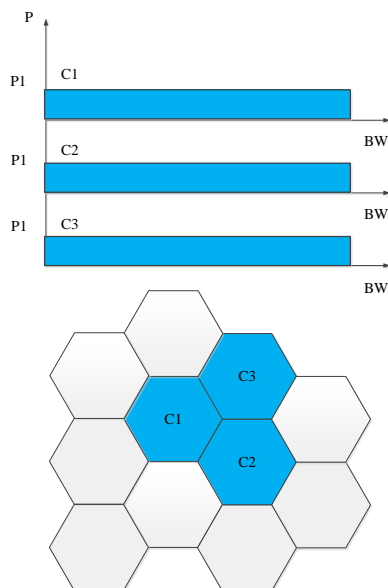
Fig. 3.1: Conventional Frequency Reuse with FRF=1. [91].
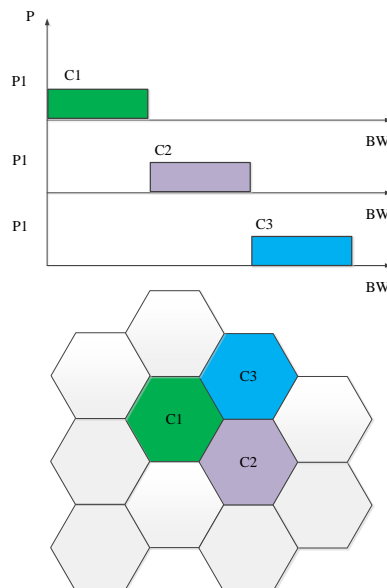
Fig. 3.2: Conventional Frequency Reuse with FRF=3. [91].

3.3.2 Fractional Frequency Reuse

This group consists of two schemes. The main idea is dividing the cell into two main regions, the cell-center region and cell-edge region. Each region has its own combination of frequencies. One of these schemes is Soft Frequency Reuse (SFR) which has been explained in [88, 89]. Another technique is Partial Frequency Reuse (PFR) which has been presented in [88, 90]. These schemes split the bandwidth into two parts: the Full Reuse (FR) part and Partial Reuse (PR) part. These two sub-bands use different frequency reuse factors (FRF). The FR part uses FRF=1 for all cells in the network. Whereas the PR part is allocated to the cell edge users and uses FRF= 3.

Partial Frequency Reuse

In PFR [91], the cell-center region of all cells have the same set of frequencies. Therefore, the Frequency Reuse Factor FRF=3. All cell-edge regions of the neighbor cells have different sets of frequencies. This means that the frequency reuse factor

is equal to 3. The power allocation of the cell-edge regions should be coordinated among the neighboring cells. In PRF the users at cell-edge are fully protected from adjacent cell interference. It can be considered as a solution to improve the cell-edge SINR, while maintaining a good spectral efficiency. Figure 3.3 gives an illustrated view of the PFR scheme.
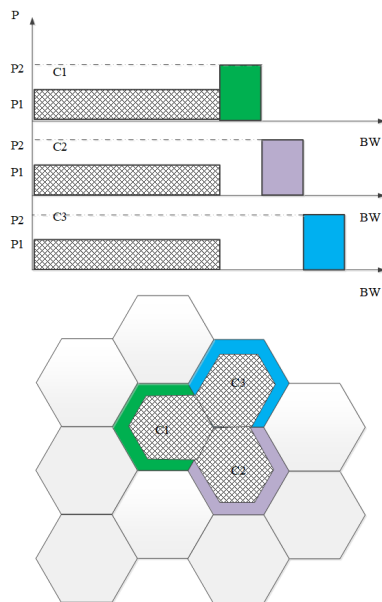
Fig. 3.3: Partial Frequency Reuse (PFR). [91].
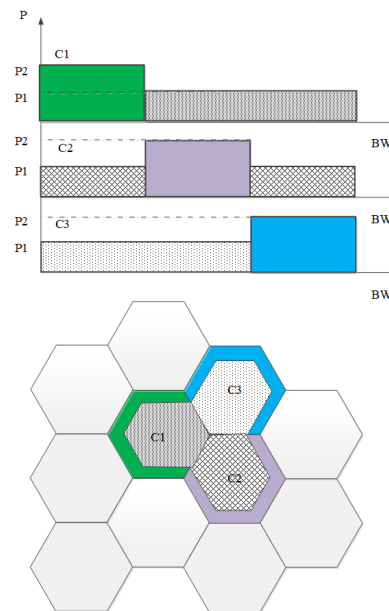
Fig. 3.4: Soft Frequency Reuse (SFR). [91].

Soft Frequency Reuse

The SFR scheme [91, 92] was suggested for utilizing the assigned bandwidth better. In SFR, each sector is transmitting the whole assigned band. The cell-edge region uses 1/3 of the available spectrum. Note that each cell-edge band is orthogonal to those in the neighboring cells. The cell-center region takes the remaining frequency band of each cell. Therefore, each cell can utilize the entire bandwidth as well as reduce the interference to its neighbors. Figure 3.4 depicts the frequency band allocation for the SFR scheme.

All above mentioned schemes are basic schemes of frequency reuse. There have been a lot of improvements suggested during the last decades. A modified scheme of Soft frequency reuse is proposed by [88]. The basic idea of the proposed scheme is to select better signal quality either from a partial reuse scheme or a soft handover scheme for the cell edge users. The achieved results show significant improvements in cell edge throughput gain over the CFR. It provides a significant cell edge throughput gain ($20 - 95$ %) over the PR scheme. It also outperforms the partial reuse scheme

in total cell throughput by $(6 - 10 \%)$. Another research [89], was conducted to improve the cell edge throughput as well as the average cell throughput, compared to a network with frequency reuse factor 1. Two different schemes of soft frequency reuse with dynamic cell center/edge partitioning are suggested. Compared to the reuse factor 1 scheme, the suggested schemes have more than a 10 % gain for the 5th percentile of cell throughput.

The optimal frequency reuse partitioning that maximizes the capacity on the downlink of the cellular system is derived by [90]. That was done by calculating the optimal solution of the partitioning cell radius. As a result of the research, the optimal frequency reuse partitioning radius r versus the total power P_{tot} is plotted. The variation of the maximum achievable capacity per cell versus the partitioning radius for different values of P_{tot} is also presented. The optimal frequency reuse partitioning radius varies between $0.55 - 0.75$, according to the total applied cell power $(1 - 10$ W$)$. Two FFR schemes, the Strict FFR and the SFR, are evaluated by [93]. A comparison among these frequency reuse schemes, in addition to the conventional frequency reuse scheme is performed. Monte Carlo, which depends on considering performance metrics such as SINR, capacity and throughput, is applied. The results show that SFR increases the cell-edge SINR and users throughput by increasing the power control factor. However, this comes at a cost of a corresponding decrease of these metrics in the inner region, thus making a tradeoff between inner and cell-edge throughput.

An interference management FFR mechanism that calculates the per-user SINR, capacity and throughput is proposed by [94]. The mechanism selects the optimal size of the inner and outer regions. The LTE system with 10 MHz bandwidth divided into 25 sub-carriers each having a bandwidth of 375 KHz is considered. Thirty users are distributed uniformly. The inner region with 93.5 m radius contains 3 users while the remaining cell area contains 27 users. The highest values of the mean throughput are observed for inner region radius between 80 m and 150 m and for inner region bandwidth between 6 MHz and 10 MHz. However, the FFR scheme that maximizes the cell mean throughput occurs for an inner region radius equal to 93.5 m and an inner region bandwidth equal to 10 MHz.

The authors in [95] propose a dynamic fractional frequency reuse (D-FFR) in unequal and time-varying traffic loads in an OFDMA network. It enables adaptive spectral sharing as per cell-load condition. By applying this scheme, the authors offer significant performance improvement. The achieved output can be formulated as follow: D-FFR outperforms FFR by 12 % in cell throughput and 33 % in service rate, and outperforms Reuse-3 by 70 % in cell throughput and 107 % in service rate.

3.4   Testbed Description

3.4.1   Fractional Frequency Reuse with Three Power Levels

FFR with three power levels differs from other techniques by working with multiple power levels. In this technique, the cell capacity density depends on cell design.
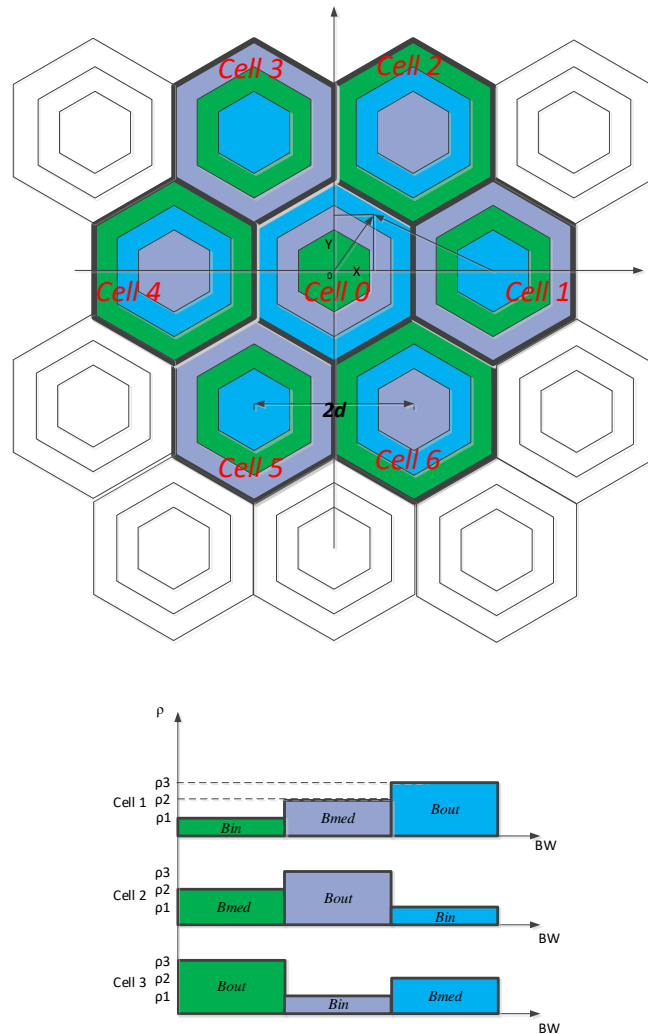
Fig. 3.5: Principles of FFR with three level control. Source: author.

Figure 3.5 depicts the cell cluster model which consists of a cell in the center and six neighbors around it. The base stations (BSs) are located in the middle of each cell, offering coverage over a regular hexagon. BS_0 is the base station of the center cell (Cell 0). Whereas BS_k is the base station for one of the six neighboring cells, depending on the value of index k; $k = 1, 2, ...6$.

The base station is equipped with three Omni direction antennas. The distance between any two adjacent BS's is $2d$ with $d = 0.5\sqrt{3}R$. The total available bandwidth in each cell B_{tot} is split into three bandwidths, the interior band B_{int}, the medium band B_{med} and the edge (outer) band B_{out} which are clarified in Fig. 3.5. All bands are reused with a low reuse factor 1. However, they are covered by transmitting signals with different powers P_1, P_2, and P_3, respectively. In order to calculate the overall cell capacity using Shannon's formula [96], the SINR expression for each cell region is educed. By considering that the base station BS_0 which is serving the studied cell (Cell 0) is trying to communicate with UE, the SINR for the three regions can be calculated according to Eq. 3.1 [96].

$$SINR = \frac{P_r}{P_{intra,cell} + P_{inter,cell} + N_0} \tag{3.1}$$

where P_r is the received power, $P_{intra,cell}$ is the interference caused by the same cell users. $P_{inter,cell}$ is the interference caused by the neighboring cell users. N_0 is the noise spectral density. Since this research is dealing with LTE OFDMA [14], the intra-cell interference equals 0. Therefore, the SINR value can be defined in Eq. 3.2:

$$SINR = \frac{P_r}{P_{inter,cell} + N_0} \tag{3.2}$$

In order to calculate the received power and the interference which is caused by the neighboring cell users, the path loss model should be chosen. In this research, the Free Space Path Loss (FSPL) model [90, 97] is used. The received power density from the user can be described in Eq. 3.3[90].

$$P_r = pL(r) \tag{3.3}$$

where p is the power spectral density which is given as the ratio of the total power and the total bandwidth $p = P_{tot}/B_{tot}$. $L(r)$ denotes the loss indicated by the FSPL path loss model.

$$L(r) = \frac{L_0}{r^n} \tag{3.4}$$

where n is the path loss exponent which varies depending on the environment, cell size and the frequency reuse distance. In rural environments with large cell size and frequency reuse distance, the path loss exponent takes values between 2 and 3. In urban environments with small cell size and reuse distance, the path loss exponent takes values between 3 and 4. More information about the path loss model depending on cell size and reuse distance can be found in [98]. Since, the urban environment

is considered, a value between 3 and 4 of the path loss exponent can be used. L_0 is given by the following expression:

$$L_0 = \left(\frac{\nu}{4\pi f}\right)^2 \tag{3.5}$$

where ν is the velocity of light in free space and f is the center carrier frequency.

The proposed model contains three discussed cases of UE position (interior, medium and edge (outer)). Therefore, three cases of SINR will be formulated. The first position can be achieved when $UE(X, Y)$ is located in the interior area at the distance $r = \sqrt{(X^2 + Y^2)}$ from the cell center. It receives on a chosen frequency, a useful signal from BS_0, an additive white Gaussian noise as well as interference from other BS's which are transmitting on the same frequency. Therefore, UE in the interior region of the center cell is interfered by the signal of the medium area of the first, third and fifth neighboring cells and the outer region of the second, fourth and sixth cells. In this case, the SINR can be presented using Eq. 3.6.

$$\Gamma_1(X, Y) = \frac{p_1 L_0 / r^\alpha}{N_0 + \sum_{k=2m-1}^{n} p_2 L_0 / r_k^\alpha + \sum_{k=2m}^{n} p_3 L_0 / r_k^\alpha} \tag{3.6}$$

where r_k, $(k = 2m - 1$ or $k = 2m$, $m = 1, 2, 3)$ are the distances between the UE and the base station of the first, third and fifth or second, fourth and sixth neighboring cells, respectively. To simplify the calculations, the Cartesian coordinates (X, Y) are normalized to the cell radius R and denoted by (x, y). So the average SINR with normalized coordinates is given by Eq. 3.7.

$$\gamma_1(x, y) = \frac{\Gamma_{e,int}}{(x^2 + y^2)^{\alpha/2}[1 + \Gamma_{e,med}S_{odd}(x, y) + \Gamma_{e,out}S_{even}(x, y)]} \tag{3.7}$$

where $\Gamma_{e,int}, \Gamma_{e,med}$ and $\Gamma_{e,int}$ are the edge region SNRs (without considering interference) caused by three levels of power and defined by Eq. 3.8.

$$\begin{aligned} \Gamma_{e,int} &= \frac{p_1 L}{N_0 R^\alpha} \\ \Gamma_{e,med} &= \frac{p_2 L}{N_0 R^\alpha} \\ \Gamma_{e,out} &= \frac{p_3 L}{N_0 R^\alpha} \end{aligned} \tag{3.8}$$

The sum of the path loss distances r_k from the first, third and fifth and from the second, fourth and sixth neighboring cells are denoted by $S_{odd}(x, y)$ and $S_{even}(x, y)$, respectively and calculated using Eq. 3.9.

$$\begin{aligned} S_{odd}(x, y) &= \sum_{k=2m-1}^{n} [(x - x_k)^2 + (y - y_k)^2]^{-\alpha/2} \\ S_{even}(x, y) &= \sum_{k=2m}^{n} [(x - x_k)^2 + (y - y_k)^2]^{-\alpha/2} \end{aligned} \tag{3.9}$$

According to Fig. 3.5 by considering that the BS_0 located at the center $(0,0)$, x_k and y_k for the neighboring cells can be calculated as follow:

- 1st neighboring cell: $x_k = 2d/R = \sqrt{3}$ and $y_k = 0$
- 2nd neighboring cell: $x_k = d/R = \frac{\sqrt{3}}{2}$ and $y_k = (R + \sqrt{R^2 - d^2})/R = \frac{3}{2}$
- 3rd neighboring cell: $x_k = -d/R = -\frac{\sqrt{3}}{2}$ and $y_k = (R + \sqrt{R^2 - d^2})/R = \frac{3}{2}$
- 4th neighboring cell: $x_k = -2d/R = -\sqrt{3}$ and $y_k = 0$
- 5th neighboring cell: $x_k = -d/R = -\frac{\sqrt{3}}{2}$ and $y_k = -(R + \sqrt{R^2 - d^2})/R = -\frac{3}{2}$
- 6th neighboring cell: $x_k = d/R = \frac{\sqrt{3}}{2}$ and $y_k = -(R + \sqrt{R^2 - d^2})/R = -\frac{3}{2}$

After applying these calculations, $S_{odd}(x, y)$ and $S_{even}(x, y)$ can be given by Eq. 3.10.

$$
\begin{aligned}
S_{odd}(x,y) &= [(x - \sqrt{3})^2 + y^2]^{-\alpha/2} + [(x + \frac{\sqrt{3}}{2})^2 + (y + \frac{3}{2})^2]^{-\alpha/2} \\
&\quad + [(x + \frac{\sqrt{3}}{2})^2 + (y - \frac{3}{2})^2]^{-\alpha/2} \\
S_{even}(x,y) &= [(x + \sqrt{3})^2 + y^2]^{-\alpha/2} + [(x - \frac{\sqrt{3}}{2})^2 + (y - \frac{3}{2})^2]^{-\alpha/2} \\
&\quad + [(x - \frac{\sqrt{3}}{2})^2 + (y + \frac{3}{2})^2]^{-\alpha/2}
\end{aligned}
\tag{3.10}
$$

Secondly, if $UE(X, Y)$ is located in the medium area at the distance r, where $r = \sqrt{(X^2 + Y^2)}$, it will also receive on a given frequency a useful signal from BS_0, additive white Gaussian noise, and interference from other BS's which are transmitting on the same frequencies. According to Fig. 3.5, the UE in the medium region of the center cell is interfered by the signal of the outer area of the first, third and fifth neighboring cells and the interior region of the second, fourth and sixth cells. In this case, SINR can be calculated using Eq. 3.11.

$$
\gamma_2(x,y) = \frac{\Gamma_{e,med}}{(x^2 + y^2)^{\alpha/2}[1 + \Gamma_{e,out}S_{odd}(x,y) + \Gamma_{e,int}S_{even}(x,y)]}
\tag{3.11}
$$

Thirdly, in the case where $UE(X, Y)$ is located in the outer (edge) area at the distance $r = \sqrt{(X^2 + Y^2)}$ from the base station of the center cell, according to Fig. 3.5, the UE in the outer region of the center cell is interfered by the signal of the interior area of the first, third and fifth neighboring cells and the medium region of the second, fourth and sixth cells. In this case SINR can be calculated using Eq. 3.12:

$$
\gamma_3(x,y) = \frac{\Gamma_{e,out}}{(x^2 + y^2)^{\alpha/2}[1 + \Gamma_{e,int}S_{odd}(x,y) + \Gamma_{e,med}S_{even}(x,y)]}
\tag{3.12}
$$

These three cases of SINR can be concluded in the following general equation

Eq. 3.13

$$\gamma_\beta(x,y) = \begin{cases} \frac{\Gamma_{e,int}}{(x^2+y^2)^{\alpha/2}[1+\Gamma_{e,med}S_{odd}(x,y)+\Gamma_{e,out}S_{even}(x,y)]} & (x,y) \in Interior - Area \\\\ \frac{\Gamma_{e,med}}{(x^2+y^2)^{\alpha/2}[1+\Gamma_{e,out}S_{odd}(x,y)+\Gamma_{e,int}S_{even}(x,y)]} & (x,y) \in Medium - Area \\\\ \frac{\Gamma_{e,out}}{(x^2+y^2)^{\alpha/2}[1+\Gamma_{e,int}S_{odd}(x,y)+\Gamma_{e,med}S_{even}(x,y)]} & (x,y) \in Edge - Area \end{cases}$$

(3.13)

In order to simplify the equations, the research assumes that the frequency reuse partitioning boundaries of the interior and medium areas take a circular shape, therefore $\beta_1(\theta) = \rho_1$ and $\beta_2(\theta) = \rho_2$ for all θ. By considering a circular cell boundary of radius R and defining $x = r, y = 0$ (polar coordinates with $\theta = 0$), where r and ρ are normalized to R, the SINR for the three regions can be simplified and presented in Eq. 3.14.

$$\gamma_\rho(r) = \begin{cases} \frac{\Gamma_{e,int}}{r^\alpha[1+\Gamma_{e,med}S_{odd}(r)+\Gamma_{e,out}S_{even}(r)]} & 0 < r \leq \rho_1 \\\\ \frac{\Gamma_{e,med}}{r^\alpha[1+\Gamma_{e,out}S_{odd}(r)+\Gamma_{e,int}S_{even}(r)]} & \rho_1 < r \leq \rho_2 \\\\ \frac{\Gamma_{e,out}}{r^\alpha[1+\Gamma_{e,int}S_{odd}(r)+\Gamma_{e,med}S_{even}(r)]} & \rho_2 < r \leq 1 \end{cases}$$

(3.14)

where $S_{odd}(x,y) = S_{odd}(r)$ and $S_{even}(x,y) = S_{even}(r)$ are defined in Eq. 3.15.

$$s_{odd}(r) = (r - \sqrt{3})^{-\alpha} + 2[(r + \frac{\sqrt{3}}{2})^2 + \frac{9}{4}]^{-\alpha/2}$$
$$s_{even}(r) = (r + \sqrt{3})^{-\alpha} + 2[(r - \frac{\sqrt{3}}{2})^2 + \frac{9}{4}]^{-\alpha/2}$$

(3.15)

According to all above, the capacity density of the center cell (or any other cell) can be written as an aggregation of the capacity density of the three cells' areas.

$$c_{cell}(r) = c_{int}(r) + c_{med}(r) + c_{out}(r)$$

(3.16)

3.4.2 User Distribution

The user distribution plays an important role in the performance evaluation of a cellular system. Usually, a uniform distribution of users is assumed [90, 99, 100]. However, such distribution is not realistic for the majority of actual scenarios. In a realistic cellular network, user distribution is determined by the physical topography of the land and other factors like roads, buildings, parking and so on. Therefore, different non-uniform distributions are required for better simulation of different environments.
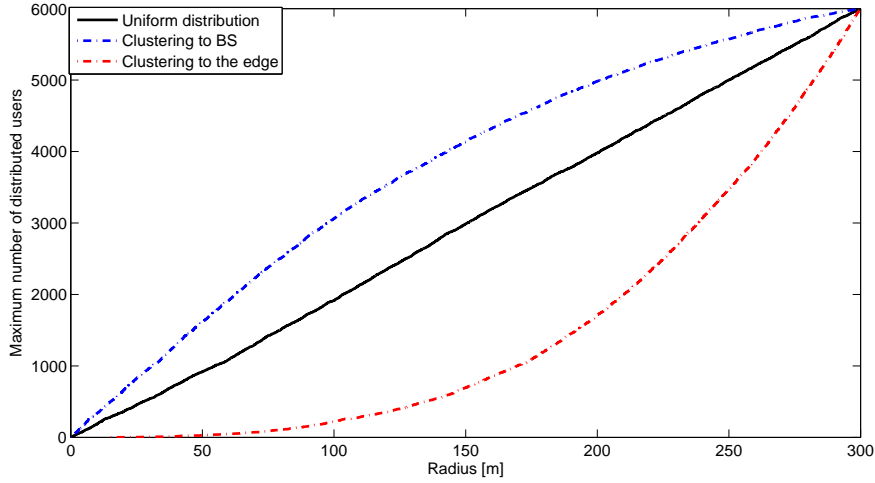
Fig. 3.6: Three different user distribution all over the cell. Source: author.

The user distribution model in [99] divides the cell area into two regions. The outer area near the cell boundary, contains uniformly distributed users. Whereas, the internal area consists of semi-Gaussian distribution with a concentrated region near the base station. The area of these two regions can be controlled using several described parameters. In [100], the authors proposed a rotationally symmetrical two-dimensional probability user distribution function. In this research, I have considered three different user distribution models used for cell region optimization. Besides the default UD, two non-uniform distributions with CBS and CCE are used. In order to achieve N non-uniformly distributed users with CBS, Eq. 3.17 is used [101].

$$P_i(r_i) = \frac{(\alpha - r_i)^2 . \beta + \alpha^2}{\sum_{k=1}^{N}[(\alpha - r_k)^2 . \beta + \alpha^2]} \tag{3.17}$$

where $P_i(r_i)$ is the probability density function of this distribution. α, r_i, β are the cell side length, the distance of the user i and the strength of user clustering, respectively. The probability density function of CCE user distribution is computed using Eq. 3.18 [101].

$$P_i(r_i) = \frac{r_i^2 . \beta + \alpha^2}{\sum_{k=1}^{N}[r_k^2 . \beta + \alpha^2]} \tag{3.18}$$

The sign of β is related to the type of non-uniform distribution. In the case of UEs CBS, Eq. 3.17 is applied and β takes negative values. Whereas using non-uniform

user distribution with CCE, positive values of β should be applied to Eq. 3.18. It should be noted that when $\beta=0$ and using Eq. 3.18, UD is generated.

In Fig.3.6 the relation between the radius of the region and the maximum number of distributed users inside the corresponding covered area is plotted. The black line depicts uniform user distribution. Whereas, the blue and red curves show non-uniform distribution: clustering to the base station and clustering to the cell edge, respectively.

3.5 Setup and Results

The results are demonstrated on this particular setup: number of users $N = 6000$ distributed over the cell with radius $R = 250\ m$. Without losing generality, the results are evaluated for the center cell $BS0$, while the six neighbor cells serve as the interferers. Three different types of distribution are taken into consideration; UD, CBS and CCE. For more details, all required parameters are summarized in Tab. 3.1 [102].

By using the normalized SINR Eq. 3.14 and the data given in Tab. 3.1, the possible frequency partitioning radiuses versus overall cell capacity are studied. This research is done for LTE Advanced OFDMA [1, 14].

Tab. 3.1: Simulation parameters

Symbol	Quantity	Values
R	Cell radius	250 m
B_{tot}	The total bandwidth	20 MHz
N_0	Noise spectral density	-174 dBm/Hz
α	Path loss exponent	3.6
P_{tot}	Total transmitted power	20 W
f	Center frequency	2 GHz
D	Distribution	UD, CBS, CCE

The blue curves of Fig. 3.7, Fig. 3.8 and Fig. 3.9 depict the per-user capacity in the medium region for uniform distribution, clustering to the base station and clustering to the cell edge, respectively. It can be observed that the medium region is affected by changing the interior and medium radiuses of the neighbor cells. As mentioned in Fig. 3.5, the medium region of the studied cell is interfered by the interior or outer regions of the neighboring cells. Due to this fact, by increasing the radius of the interior region, in other words, by increasing the power P_1, the interference caused by the interior region of the neighbor cells will be increased so
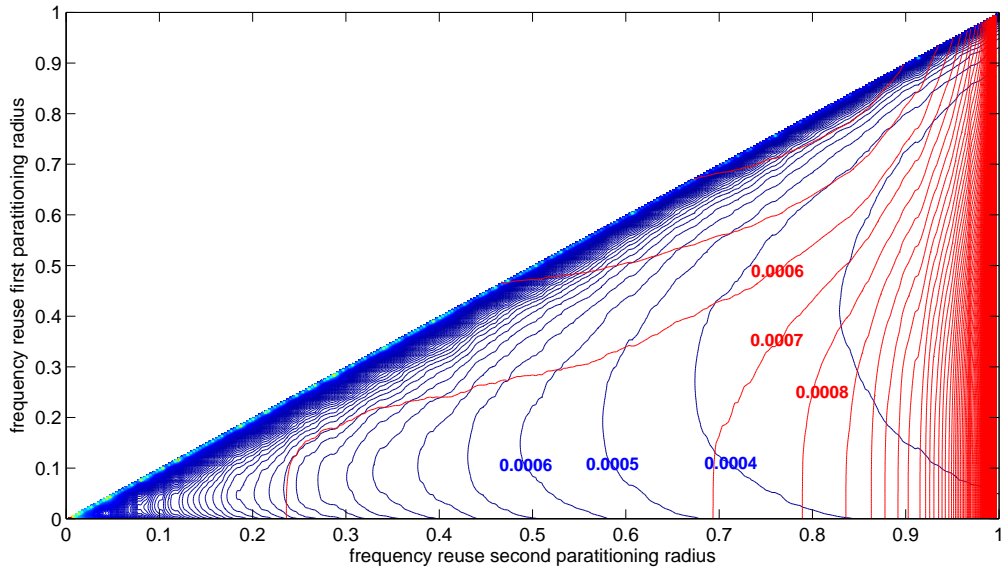
Fig. 3.7: Normalized per-user capacity to the total bandwidth in the medium and the outer regions for uniformly distributed users (UD). Source: author.

per-user capacity of the medium region of the studied cell will be decreased. That's what happens when r_{int} is between $0 - 0.4$, $0 - 0.15$, and $0 - 0.45$ for UD, CCB, CCE, respectively. This impact happens because the number of users rarely changes compared with the increasing interference from the surrounding cells. This effect is expounded by the low density of users near the cell center. In order to cancel this effect, the number of users inside the cell should be significantly raised. That led to markedly increasing user density all over the cell. It is also clear, that this effect becomes smaller in the case of CCB comparing with UD and CCE. However, when r_{int} increases more than the previous mentioned ranges, the capacity of the medium area also increases. This happens because increasing r_{int} increases the number of users in the interior region so the number of users in the medium region decreases. On the other hand, by increasing r_{med}, the number of users of the studied medium region and the interference from the outer region of previous mentioned cells increase, therefore, per-user capacity in the medium region decreases.

The red curves of Fig.3.7, Fig.3.8 and Fig.3.9 present the per-user capacity in the outer region of the studied cell in the case of uniform distribution, clustering to the base station and clustering to the cell edge, respectively. It can be observed that increasing r_{int} negatively affects the capacity results. That happens because increasing r_{int} increases the power of the interior region P_1. Increasing the power P_1, in turn, increases the interference on the outer region of the studied cell. However,
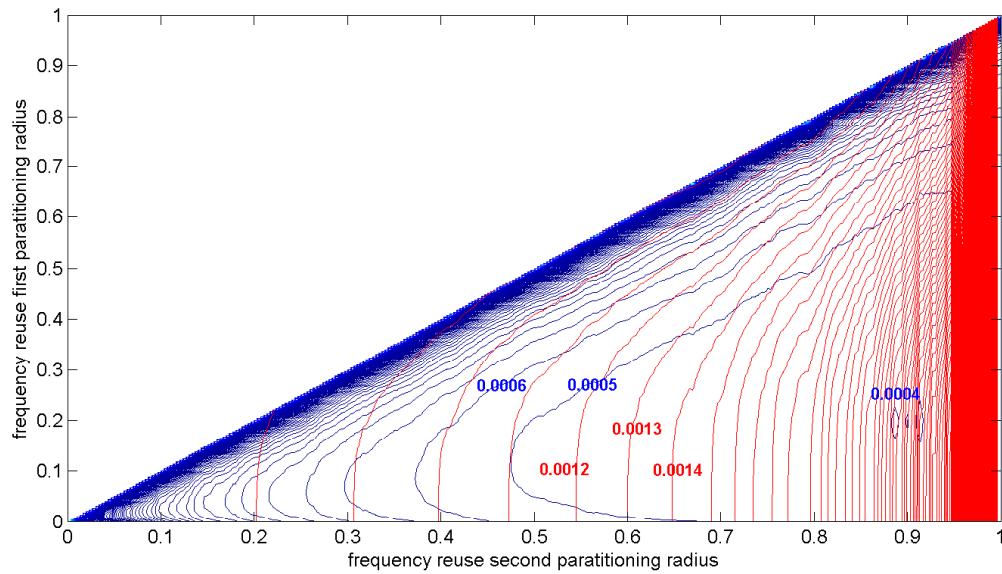
Fig. 3.8: Normalized per-user capacity to the total bandwidth in the medium and the outer regions for non-uniform distribution CBS. Source: author.
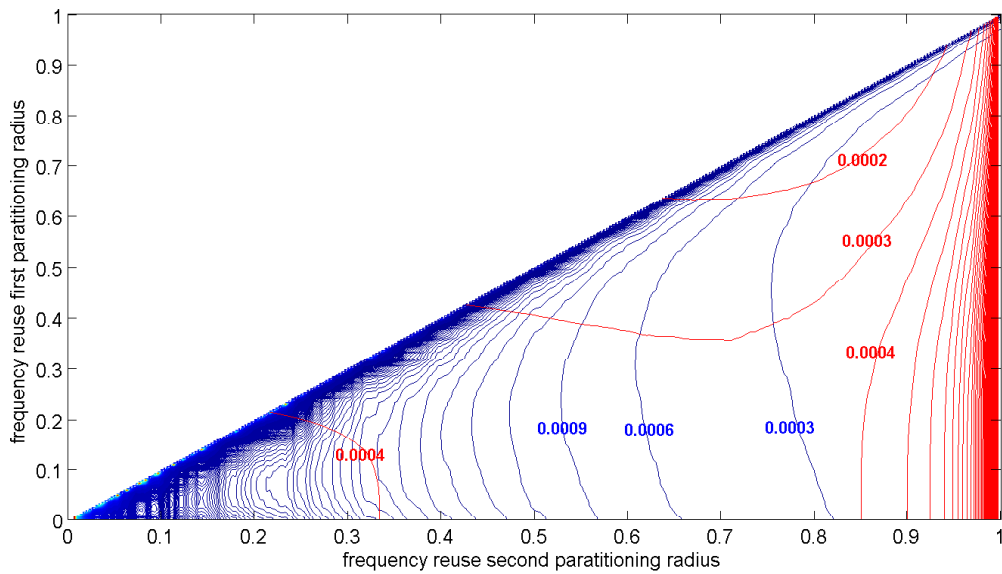
Fig. 3.9: Normalized per-user capacity to the total bandwidth in the medium and the outer regions for non-uniform distribution CCE. Source: author.

increasing the radius of the medium region r_{med} increases the number of uniformly distributed users which are placed in the medium area, so the number of users

in the outer area decreases. By decreasing the number of users inside the outer region, we are increasing the per-user capacity. It can also be distinguished that the interference caused by the medium region of the neighbor cells is negligible compared with the effects of the user number decreasing. From these figures, it can be concluded that per-user capacity of the medium and outer regions are inversely proportional to each other. This fact can help us to determine the best r_{int} and r_{med} to achieve approximately the same per-user capacity in both regions or prioritize one region over another. Also, it should mentioned that choosing the best r_{int} and r_{med} not only depends on the highest achieved per-user capacity but also on the number of users inside each region. In this research, the relation between the maximum number of users inside each region and the regions' radiuses are presented and plotted in Fig. 3.6. After determining the best r_{int} and r_{med}, the transmitting power of the interior and the medium regions P_1 and P_2 can be calculated. These calculations can be done using Eq. 3.3 where the minimum received power on the edge of the interior and medium regions $P_{rmin} = -113$ dBm. Depending on the previous selected radiuses, the overall capacity of the cell can be determined. Note
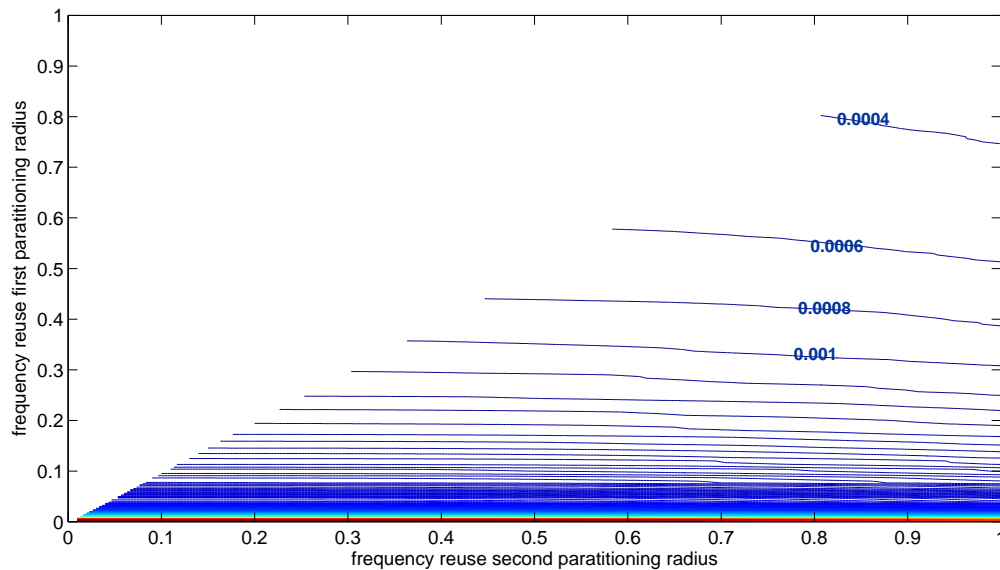
Fig. 3.10: Normalized per-user capacity to the total bandwidth in the interior region for UD. Source: author.

that in Fig. 3.7 and Fig. 3.8, the capacity curves for both the medium and outer regions (blue and red curves) are separated by the value of 0.0001 bit per second per user per hertz. In Fig. 3.9 the separation is 0.0003 bit per second per user per hertz for the medium region (blue) and 0.0001 bit per second per user per hertz for

the outer region (red).
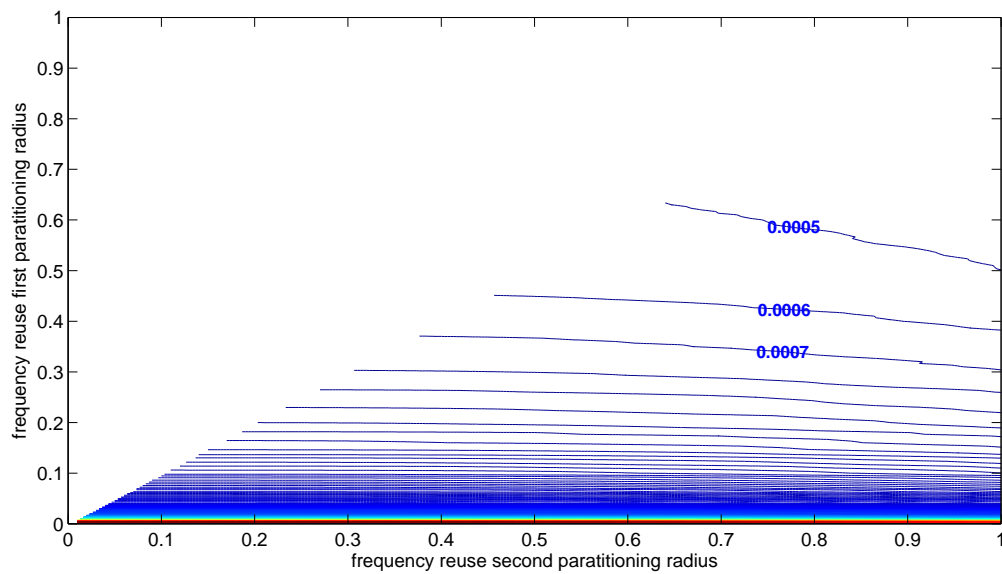
Fig. 3.11: Normalized per-user capacity to the total bandwidth in the interior region for non-uniform distribution CBS. Source: author.
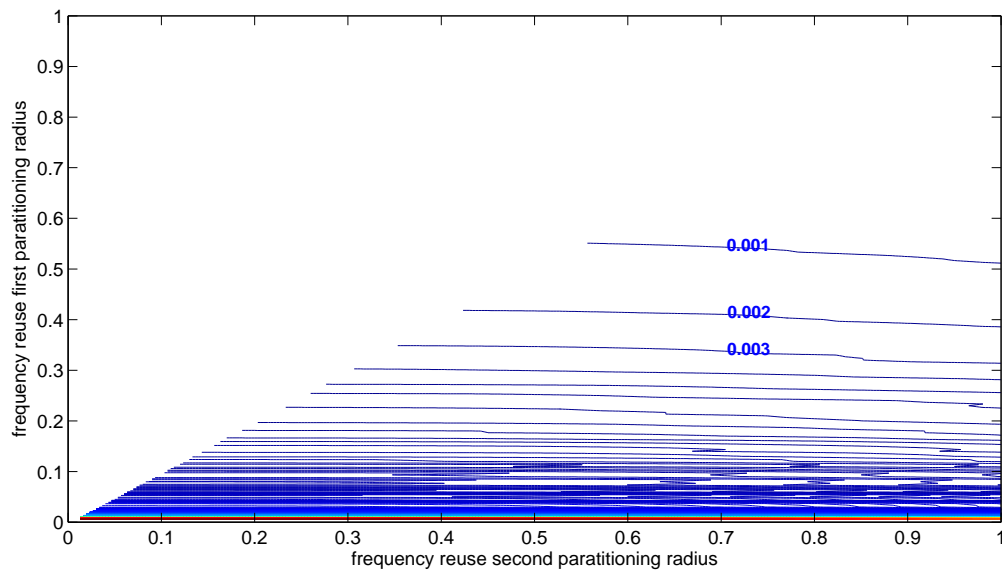
Fig. 3.12: Normalized per-user capacity to the total bandwidth in the interior region for non-uniform distribution CCE. Source: author.

From Fig. 3.10, Fig. 3.11, and Fig. 3.12, it can be distinguished that increasing the medium region has a small effect on the capacity of the interior region. Increasing the power of the medium region of the first, third and fifth cell causes interference in the interior region of the studied cell, which is operating on the same bandwidth. Because of the big distance between these two regions, interference is very small and can be omitted. As we mentioned in Fig. 3.5, the interior region is interfered also by the outer regions of the second, fourth and sixth neighbor cells. Increasing the radius of the interior region negatively affects the average capacity of its users. This happens due to two reasons. The first one can be explained as: increasing the interior radius increases its area so the number of users inside this area will be increased. Since the capacity of each area is constant, per-user capacity is decreased. The second reason is that the border of the interior users became more interfered by the power of the outer region of neighbor cells. Increasing r_{int} increases the interior area so the interior border users become closer to the interference effects of the outer region of the surrounding cells.
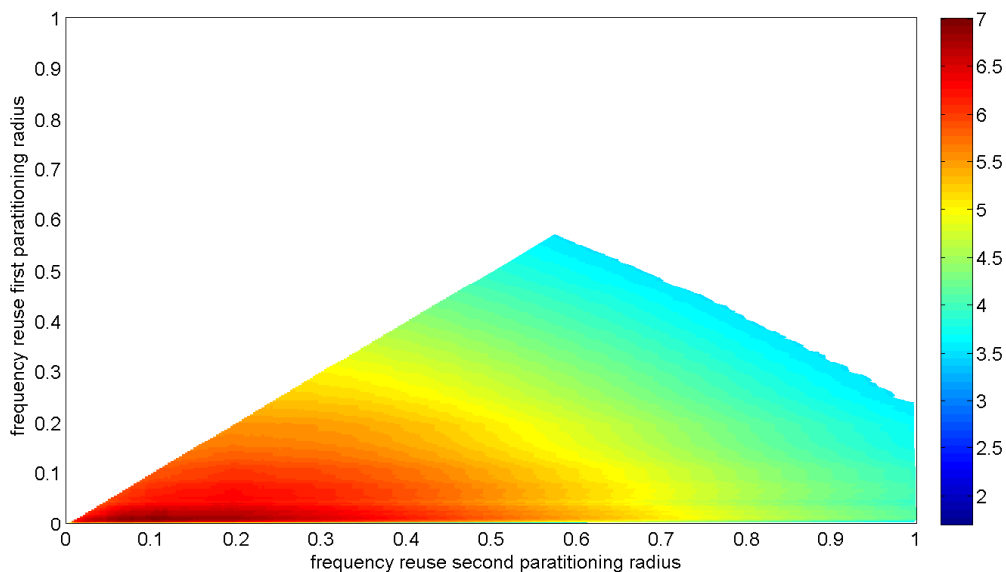
Fig. 3.13: Overall cell capacity normalized to the total bandwidth [bps/Hz] for UD. Source: author.

Depending on the previous selected radiuses, the overall capacity of the cell can be determined. Figures 3.13, 3.14, and 3.15 show the overall cell capacity, depending on the normalized interior and medium radiuses for the three previous mentioned distributions. The overall cell capacity is normalized to the total bandwidth B_{tot}. When $r_{int} = 0$ and $r_{med} = 0$, the total bandwidth B_{tot} is divided into three sub-bands
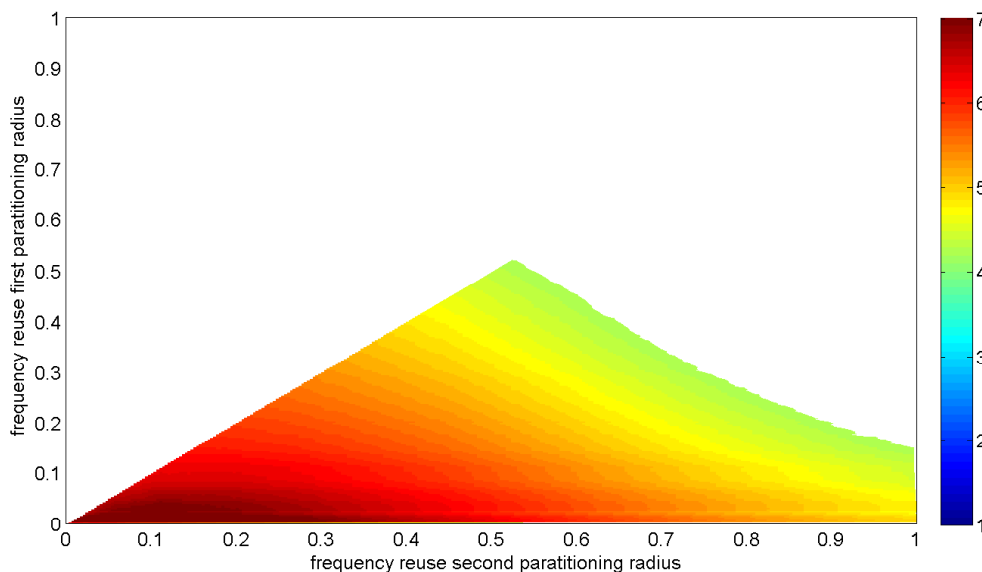
Fig. 3.14: Overall cell capacity normalized to the total bandwidth [bps/Hz] for non-uniform distribution, CBS. Source: author.

with $FRF = 3$. For this case, the overall capacity is also calculated. This capacity is captured as a flat surface in each of above mentioned figures. It is flat because in the case of $FRF = 3$, each cell uses $1/3$ of the total bandwidth and it doesn't suffer from the neighbor cell interference. It is depicted as a default surface to be compared with the achieved capacity of the studied case. Fig. 3.13 depicts the overall normalized capacity of the selected cell Cell 0 calculated for different values of interior and medium radiuses with uniform user distribution. It presents only the values leading to higher capacity than $FRF = 3$. According to the presented results, the FFR with three power levels is a useful method for all values of interior and medium radiuses except those that make the total capacity less than the minimum capacity ($r_{int} = 0$ and $r_{int} = 0$).

Fig. 3.14 and Fig. 3.15 depict the overall normalized capacity of the selected cell (Cell 0) calculated for different values of interior and medium radiuses with non-uniform user distribution. Fig. 3.14 corresponds to the case of UEs cluster towards the BS, while Fig. 3.15 to the UEs cluster towards the cell edge. Similarly to the previous case of uniform user distribution, only the values leading to capacity higher than $FRF = 3$ capacity are shown. Fig. 3.13, Fig. 3.14 and Fig. 3.15 can help us to identify the capacity depending on the maximum number of users in each region, by taking into consideration the relation between the number of users in each region and its radius (presented in Fig. 3.6).
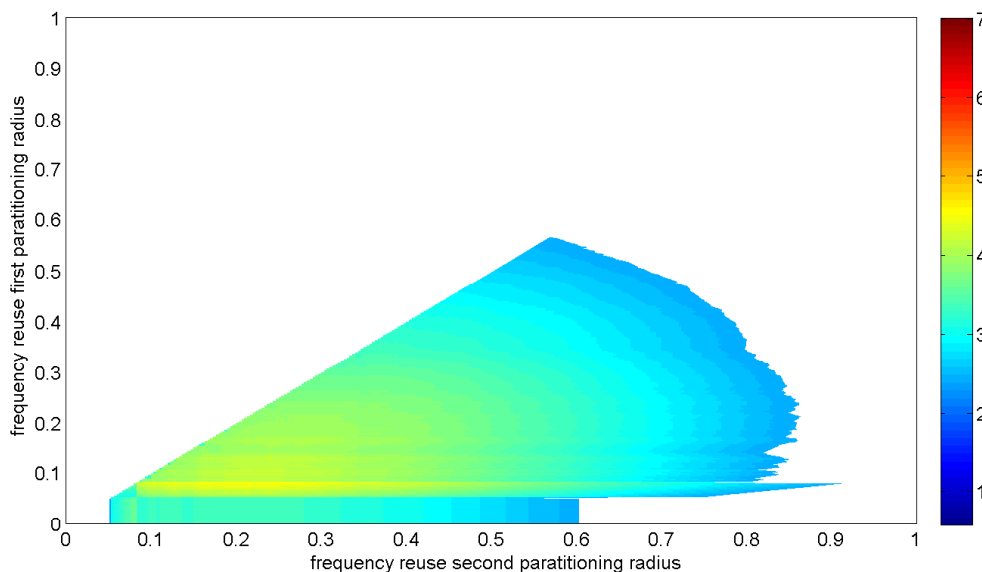
Fig. 3.15: Overall cell capacity normalized to the total bandwidth [bps/Hz] for non-uniform distribution, CCE. Source: author.

According to all mentioned information above, it can be concluded that FFR with three power levels is a useful method compared with the default one $FRF = 3$ or Frequency Reuse Partitioning which is presented in [90] and reach a value of 2.7 [bps/Hz] as a maximum overall cell capacity normalized to the total bandwidth.

3.6 Conclusion

Inter-cell interference is one of the most important issues facing the planning of OFDMA-based networks. It becomes very critical in the case of D2D users under LTE Advanced networks. In this research, FFR with three power levels is suggested. In order to prove the efficiency of this method, the capacity of each region is calculated. Then the relation between the radiuses of the regions and the total normalized capacity for different user distribution has been investigated. Depending on the user distribution and the number of users inside each region, the radiuses of the interior and medium region can be easily determined. In order to make this research more realistic, three different cases of user distribution inside the cells are considered. Two of them are non-uniform user distributions which are compared with the performance of the widely used UD. The achieved results of the proposed scheme outperform the results of traditional Reuse-3 for specific radiuses of each region. These radiuses are suggested to be used for the best performance in terms

of channel capacity. Finally, the main advantage of this method is using the whole bandwidth in each cell compared with other methods which use only part of the assigned bandwidth. Therefore, using this method will improve network performance and its efficiency. However, the drawbacks are extra hardware and software modifications. These modifications will give the cell the flexibility to change the distribution of power and bandwidth among its regions according to real user distribution. This feature can be called a breathing cell property.

4 COOPERATIVE SPECTRUM SENSING FOR D2D COMMUNICATION

Cooperative spectrum sensing is one of the most effective methods for preventing harmful interference and improving detection performance through identifying the free available spectrum. Therefore, it is one of the methods that can be used for interference mitigation in the D2D communication underlay LTE Advanced network. This method helps us to identify the available spectrum for future utilization.

One of the main approaches of spectrum management is allocating a fixed spectrum to specific services. In this case, the allocated spectrum for primary users (PU) can't be used by others (secondary users (SU)). Usually, these frequency bands are not used all of the time by the primary users. According to these facts, this assignment can cause poor spectrum utilization. In order to solve this drawback, the cognitive radio network (CRN) was proposed [103, 104, 105]. These networks are characterized by the spectrum sensing technique - the functionality to determine unoccupied frequency bands (spectrum holes, whitespaces). The CRN can contain two types of users: the primary users (PU or LTE Advanced users) and the secondary users (SU or D2D communication users). Spectrum sensing can help D2D users in preventing harmful interference that can effect LTE Advanced users. This leads to an increase in the spectral efficiency. Making a decision depends on the required reliability expressed by the probability of detection and the probability of false alarm. However, many factors can affect the detection performance, such as multipath fading, shadowing and receiver uncertainty issues. In order to mitigate the impact of these undesirable effects, cooperative spectrum sensing has been proposed as the most effective approach [104, 105, 106]. The main idea of cooperative spectrum sensing is to enhance sensing performance by exploiting spatial diversity in the observations of spatially located SUs (D2D users). By cooperation, the D2D users can share their sensing information to make a combined decision more accurately than in the case of the individual devices.

In this chapter a brief evaluation of the cooperative spectrum sensing methods is presented. Three merging rules (OR, AND, MAJORITY) [103] are used. This happened by applying both ED and KS tests. The evaluation is achieved by testing a TX-RX system not only with different transmitted signals but also with various channel models. The implemented system is tested in real channel conditions (indoor-indoor, indoor-outdoor, outdoor-indoor and outdoor-outdoor) using USRP devices. The achieved results are described as a correlation between probabilities of detection and false alarm of D2D users. Therefore, in the case where probability of false alarm is equal to 10%, the probability of detection by applying cooperative

sensing rules are increased by up to 30% compared with sensing by individuals. The percentage increase depends on the transmitted signal, detection technique and the applied cooperate sensing rule. It can also be observed that cooperative sensing of real channels with the AND rule give better results than with the OR rule, whereas the MAJORITY rule outperforms both the OR and the AND rules. Therefore, in the case of 10% probability of false alarm, the detection probabilities reach 90%, 97%, and almost 100% for the OR, the AND, and the MAJORITY rules, respectively. All these findings and a lot of others are described in this chapter.

Author's bibliography related to this chapter:

[1] Kasem, E., Lekomtcev, D., & Marsalek, R. (2015). Cooperative spectrum sensing in real channel conditions. In *13th International Conference on Telecommunications (ConTEL)*, IEEE, pp. 1–6.

[2] Lekomtcev, D., Kasem, E., & Marsalek, R. (2015). Matlab-based simulator of cooperative spectrum sensing in real channel conditions. In *25th International Conference Radioelektronika (RADIOELEKTRONIKA)*, IEEE, pp. 209–212.

4.1 Spectrum Sensing Methods

The main idea of cooperative sensing in D2D communication, is that a D2D user can use a vacant band as long as LTE Advanced does not occupy it [107, 108, 109]. But once a D2D user detects the emergence of a new LTE Advanced user, which is looking for a channel, it must release this channel immediately and find another alternative band in order not to cause interference. If a D2D user detects another D2D user using the same band, there are different mechanisms for using a spectrum fairly [107]. The main idea of cooperative sensing is to enhance the sensing performance by exploiting spatial diversity in the observations of spatially located D2D users. Many methods of spectrum sensing have been already investigated as:

- Energy detector
- Cyclostationary detector
- Cyclic prefix correlation for OFDM
- Matched filter detector
- Eigenvalue detector
- Statistical tests (like KS), etc . . .

This research concentrates on evaluating the ED and the KS tests. LTE users are mentioned as PUs, whereas D2D users are described as SUs.

4.1.1 Energy Detector

The simplest and the most common method of spectrum sensing is the ED. Moreover, sensing devices do not need any knowledge of the PU signals. In order to make a decision about the presence or absence of a signal, a predefined threshold γ , which varies depending on the noise variance σ_n^2, is used. This threshold is compared with the test statistic $T(r)$ that can be defined either in the time or frequency domain. In the time domain, test statistics are based on Neyman-Pearson criterion and given in Eq. 4.1 [108].

$$T(r) = \frac{1}{N} \sum_{n=1}^{N} (r(n))^2 \tag{4.1}$$

where N presents the number of samples used for detection. $r(n)$ is the received signal by SU. For the frequency domain, the energy detector principle is based on measuring the power $P(f)$ of the signal at the output of a band pass filter with bandwidth BW using, for example, the periodogram method [108].

4.1.2 Kolmogorov Smirnov Test

The KS test checks the accordance between the empirical (measured) and the theoretical distribution functions, whereas the distribution parameters of the theoretical distribution are known in advance. The null hypothesis H_0 (the absence of the PU transmitted signal) is assumed to be valid when the empirical and theoretical probability distributions are not statistically significantly different and the alternative hypothesis H_1 (the presence of the PU transmitted signal) is assumed when these distributions are significantly different. Firstly, the empirical cumulative distribution function (CDF) of the received signal should be calculated [110]. This function is defined by Eq. 4.2.

$$F(x) = \frac{1}{N} \sum_{n=1}^{N} J(x(n) \leq x) \tag{4.2}$$

where J denotes the indicator function, which takes the value "1" if the input is true, and the value "0" otherwise, N denotes the number of data samples from each given signal segment. The largest absolute difference between the empirical and the theoretical CDFs is used as the goodness-of-fit statistic and given by Eq. 4.3 [111].

$$T_{KS} = sup_{x \in R} \{F(x) - G(x)\} \tag{4.3}$$

where $G(x)$ is the known (expected) theoretical CDF. In accordance with the above described, the difference between theoretical and empirical CDF can be expressed

by Eq. 4.4 [111].

$$T_{KS} = max_i \{F(x_i) - G(x_i)\} \tag{4.4}$$

where $F(x_i)$ denotes the value of the CDF evaluated at the point x_i. To calculate the empirical CDF for a complex signal and additive white noise, which real and imaginary parts have normal distribution, the chi-square distribution with two degrees of freedom is used [112]. In MATLAB this can be implemented by calling the function presented in Eq. 4.5. It computes the chi-square CDF at each of the values in p using the corresponding degrees of freedom in ν (in our case $\nu = 2$).

$$G(x_i) = chi2cdf(p, \nu) \tag{4.5}$$

The hypothesis H_1 is accepted at the significance level α (the false alarm probability) when the value of the test statistic T_{KS} is lower than the critical value $k(\alpha, N)$. There are tables for the values of $k(\alpha, N)$ for $5 \le N \le 50$ in literature. As in our investigation $N \ge 50$, the critical values can be approximated in Eq. 4.6.

$$k(\alpha, N) = \sqrt{\frac{1}{N}.ln(\frac{2}{\alpha})} \tag{4.6}$$

4.1.3 Cooperative Sensing

In order to improve signal detection, cooperative spectrum sensing can be used [104, 113]. In the prospective scenario, there are M SUs that sense one PU. Each of the SUs makes its own decision regarding the presence or absence of the PU, and forwards the binary decision ('1' or '0') to the fusion center (FC) for further processing. It is known that the distance between D2D users is far less than the distances between these D2D users and the Base Station of LTE advanced. Therefore, the located SUs are negligible to each other compared to the distance from them to the PU. Thus from a long-term perspective, the primary signal received by all the SUs has the same local mean signal power. For simplicity, the noise, fading statistics and average SNR are the same for each SU, and the channels between SUs and FC are ideal (i.e. there is no loss of information). A final decision on the presence of the PU is made by k out of M SUs and can be described by binomial distribution based on Bernoulli trials where each trial represents the decision process of each SU. The generalized formula for the probability of detection at the fusion center is given by both Eq. 4.7 and Eq. 4.8 [104, 113].

$$P_{fa} = \sum_{l=k}^{M} \binom{M}{l} P_{fa,i}^l (1 - P_{fa,i})^{M-l} \tag{4.7}$$

$$P_d = \sum_{l=k}^{M} \binom{M}{l} P_{d,i}^l (1 - P_{d,i})^{M-l} \tag{4.8}$$

where $P_{d,i}$ and $P_{fa,i}$ are the probabilities of detection and false alarm respectively for each SU. In this research, three rules of the hard combination scheme are discussed.

Logical OR Rule

In this rule, a decision that the PU is present is made if any of the SUs detects the PU. The cooperative probability of detection (false alarm) using the OR fusion rule can be evaluated by setting $k = 1$ as in Eq. 4.9 and Eq. 4.10.

$$P_{fa} = 1 - \prod_{l=1}^{M} (1 - P_{fa,i}) \tag{4.9}$$

$$P_d = 1 - \prod_{l=1}^{M} (1 - P_{d,i}) \tag{4.10}$$

Logical AND Rule

In this rule, a decision that the PU is present is made if all SUs have detected the PU. The cooperative probability of detection (false alarm) using the AND fusion rule can be evaluated by setting $k = M$ as in Eq. 4.11 and Eq. 4.12.

$$P_{fa} = \prod_{l=1}^{M} P_{fa,i} \tag{4.11}$$

$$P_d = \prod_{l=1}^{M} P_{d,i} \tag{4.12}$$

Logical MAJORITY Rule

In this rule, a decision that the PU is present is made if half or more of the SUs detect the PU. The cooperative probability of detection (false alarm) using the MAJORITY fusion rule can be evaluated by setting $k = M/2$ as in Eq. 4.13 and Eq. 4.14:

$$P_{fa} = \sum_{l=M/2}^{M} \binom{M}{l} P_{fa,i}^l (1 - P_{fa,i})^{M-l} \tag{4.13}$$

$$P_d = \sum_{l=M/2}^{M} \binom{M}{l} P_{d,i}^l (1 - P_{d,i})^{M-l} \tag{4.14}$$

4.2 Testbed Description

4.2.1 MATLAB-Based Simulator

In order to evaluate the performance of cooperative spectrum sensing in real fading channels, a MATLAB-based simulation environment has been created. The simulation scenario is described in Fig. 4.1. The system consists of one PU and several SUs. PU is an LTE Advanced user, whereas SUs are D2D communication users. SUs can be both static or vehicular devices. Each of the channels between the PU and the individual SUs can be configured to one of the models described in Tab. 4.1. Various communication signals can be used as a signal transmitted by the PU.
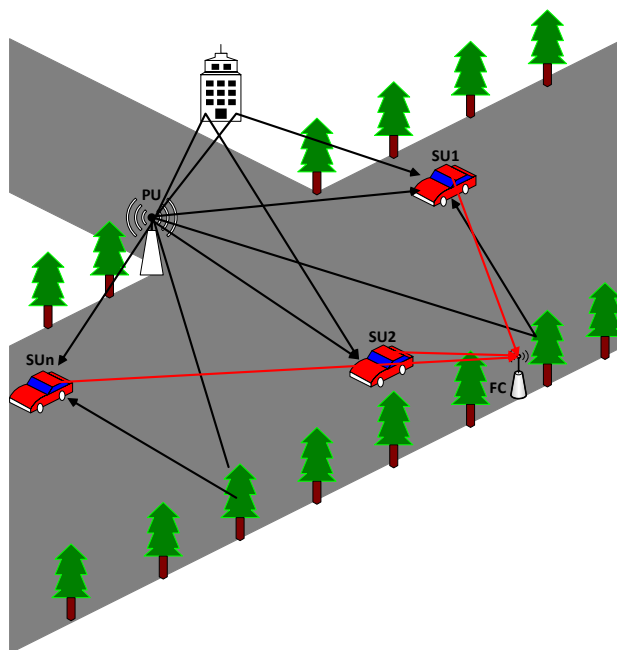
Fig. 4.1: The cooperative spectrum sensing detectors. Source: author.

The simulator was created to support two different spectrum sensing tests. The ED method decision making which is based on the power of the received signal, and KS test that checks the accordance between the empirical (measured) and the theoretical distribution functions.

Tab. 4.1: Spectrum sensing simulation parameters

Parameters	Values
Bandwidth	200 kHz
Transmitted signals	FM, 8PSK
Number of receivers	4
Channel models (SU1-SU4)	Ped A, Veh A, Veh B, Ped B
Spectrum Sensing modes	ED, KS tests
Carrier Frequency	845 MHz

In order to evaluate the performance of these spectrum sensing tests, an example setup with two distinct PU signals (frequency modulation (FM), 8PSK) was prepared. They are transmitted over four different channel models (Ped A, Veh A, Veh B, Ped B). The transmitted signals are received at four different receivers - SUs. In each receiver, two spectrum sensing tests are applied on the same acquired signal. Afterwards, in accordance with the cooperative spectrum sensing technique, each SU makes its own decision about the presence or absence of the PU signal for each sensing method (ED, KS) and sends these results to the FC. In the FC, the cooperative spectrum sensing rules (OR, AND, and MAJORITY) are applied. More details about the used channel model characteristics between the PU and different SUs are summarized in Tab. 2.1.

To evaluate the performance of a particular method of (cooperative) spectrum sensing, key characteristics such as detection probability P_d and false alarm probability P_{fa} are used [114]. The Receiver Operational Curve (ROC) graph is depicted visually. It shows the dependence between both P_d and P_{fa} parameters. Using the above mentioned simulation setup, the dependence of P_d and P_{fa} on channel type for each secondary user will be analyzed. Afterwards, spectrum sensing by individual SUs, with the respective cooperative version obtained according to three fusion rules (AND, OR, MAJORITY), will be compared. The performance evaluation for both ED and KS spectrum sensing detectors and for the two considered communication signals will be discussed. Note that for all measurements, the SNR value 6 dB is considered. All achieved results compared to real channel sensing are described in the "Results and Discussion" section.

4.2.2 Real Channel Measurements

In order to verify the above described MATLAB simulator [110, 115], real channel measurements are conducted. Therefore, a system based on USRP devices depicted in Fig. 4.2, is used. It consists of two PCs and three USRP N200 devices. One

of these USRPs is implemented as a transmitter. It is carrying out the PU role by transmitting one of the two above mentioned signals. It is connected to a PC through a Gigabit Ethernet port (blue line). The second and the third USRP $N200$ are implemented as the receivers. The first of them is carrying out the SU1 (SU3) role and is connected to the PC through a Gigabit Ethernet port (blue line). Another one (which is carrying out the SU2 (SU4) role) is connected to the first
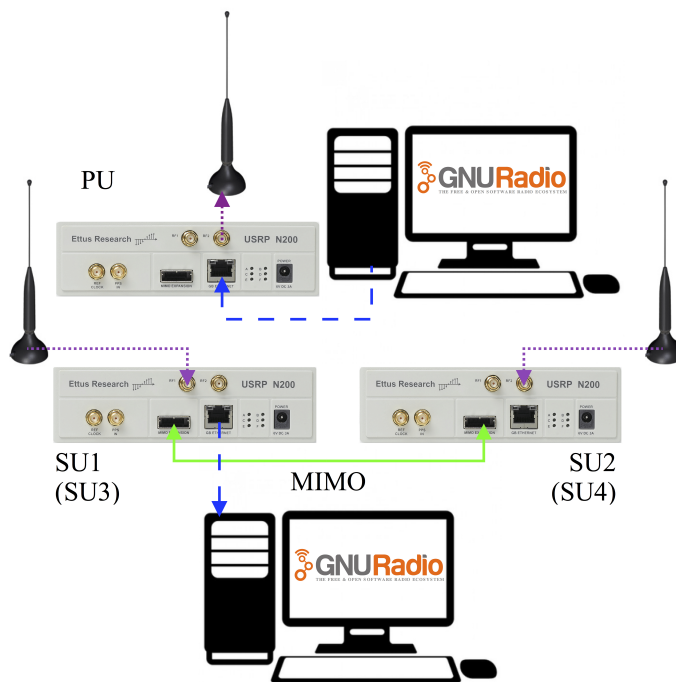
Fig. 4.2: Experimental setup. Source: author.

USRP through a MIMO cable (green line) to build a synchronized received system.

Note that the precise synchronization between the SUs must be realized in order to realize the cooperative scheme. In this research, synchronization between the transmitter and the receiver is achieved by transmitting an orthogonal code (Large area synchronous code) [116], which is transmitted at the beginning of each burst of the signal. In the setup, each USRP contains the WBX daughter board (front-end). For different channel model realizations, the receiver and transmitter antennas were located in various environments (indoor or outdoor).

The primary user signal is an 8PSK (or FM) signal with bandwidth 200 kHz (bandwidth corresponding to wireless microphones bandwidth) centered on 845 MHz carrier frequency, which corresponds to one of the uplink FDD LTE Advanced channels). Each SU scans the channel twice: first when it is not an occupied channel, second when it is a channel where PU transmits. Note that although the channel

is vacant, it is possible to suppose that the character of the received signal is not exactly white Gaussian as it can contain interference from neighboring bands.

The PC is running Fedora 16, the signal processing applications are done using open-source GNU Radio version 3.7.2.1. PU transmits the same signal (8PSK or FM) as was used for MATLAB-based simulator [115]. These signals are generated in MATLAB and recorded into the data files for transmission in GNU Radio. Each SU sensed the channel of interest. By applying GNU Radio, the sensing results are recorded into data files for subsequent processing. Afterwards, based on the recorded data files, the P_d and P_{fa} values are calculated for each SU in order to estimate corresponding ROC curves. The equations to estimate these quantities are depicted in Eq. 4.15 and Eq. 4.16.

$$P_d = \frac{Number\ of\ segments\ that\ have\ Y > \gamma\ |\ H_1}{Number\ of\ observed\ segments} \tag{4.15}$$

$$P_{fa} = \frac{Number\ of\ segments\ that\ have\ Y < \gamma\ |\ H_1}{Number\ of\ observed\ segments} \tag{4.16}$$

In accordance with fusion rules for cooperative sensing, a final decision about a vacant channel is made. These results are presented below.

4.3 Results and Discussion

In order to evaluate the performance of the previous described system, methods of the cooperative spectrum sensing technique are applied. By using key characteristics as P_d and P_{fa} [114], all the following results are presented. First, the dependence of P_d and P_{fa} on channel type for each secondary user is analyzed. Afterwards, spectrum sensing using individual SUs with cooperative version which is obtained according to the three fusion rules (AND, OR, MAJORITY) are compared. In this section, the comparison between system performance in real and simulated environments for different transmitted signals and detectors are discussed.

Figure 4.3 depicts the difference between the performance of the spectrum sensing technique in real and simulated channels for the FM signal using the KS detector. It can be observed that using sensing by individuals SU3 and SU4, Ped B and Veh B channels results have better detection performance than other models. While Veh A (SU2) shows the worst simulated results. It can also be seen that most real channel detection performance is worse than for the simulated model in the case of individual detection.

It should be noted that for the channel with indoor located PU and SU the ROC curve graph is close to MATLAB-simulated channels. Probably, the reason for this
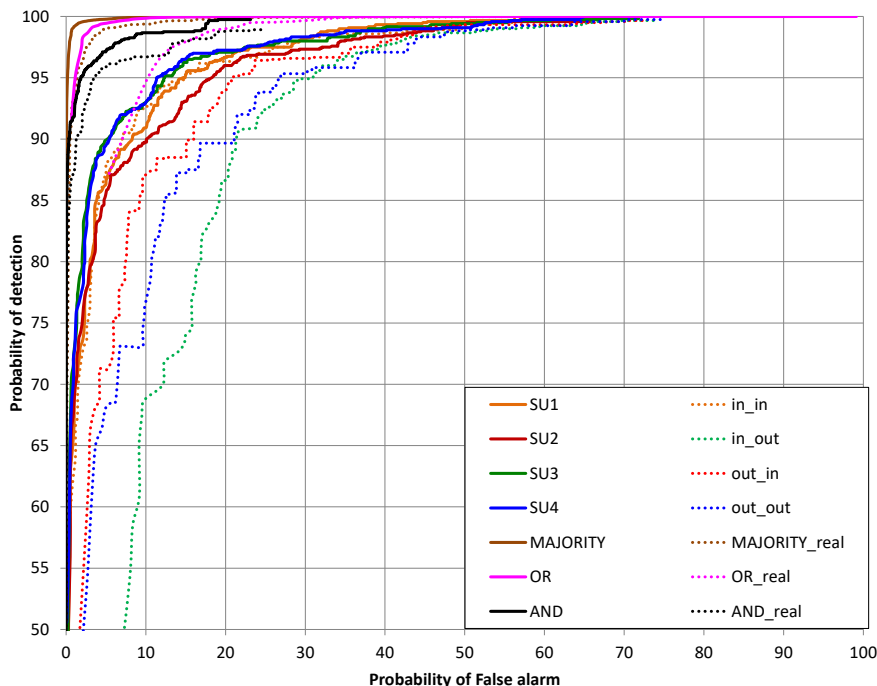
Fig. 4.3: ROC curves for FM received signal using KS test detector in real and simulated channels. Source: author.

is that measurement conditions in the laboratory were almost ideal (without big interference from outside). As well, it shows approximately the same performance for real channels, in the case where cooperative sensing technology is applied. That can prove the effectiveness of our simulator in the case of an FM transmitted signal and the KS detection technique. It can also be observed that cooperative sensing of real channels with the AND rule give better results than with the OR rule, whereas the MAJORITY rule outperforms both the OR and AND rules. It is also clear that in the case of probability of false alarm is equal to 10 %, the probabilities of detection are 90 %, 97 %, and almost 100 % for the OR, AND, and MAJORITY rules, respectively.

Fig. 4.4 presents the cooperative sensing technique for an FM signal by applying the ED detector at the receiver side. As expected and evident, in the case of simulated channels, all cooperative fusion rules give better detection performance than sensing by individual users. However, simulation models provide better detection than USRP-based (indoor and outdoor channels). The worst performance for an
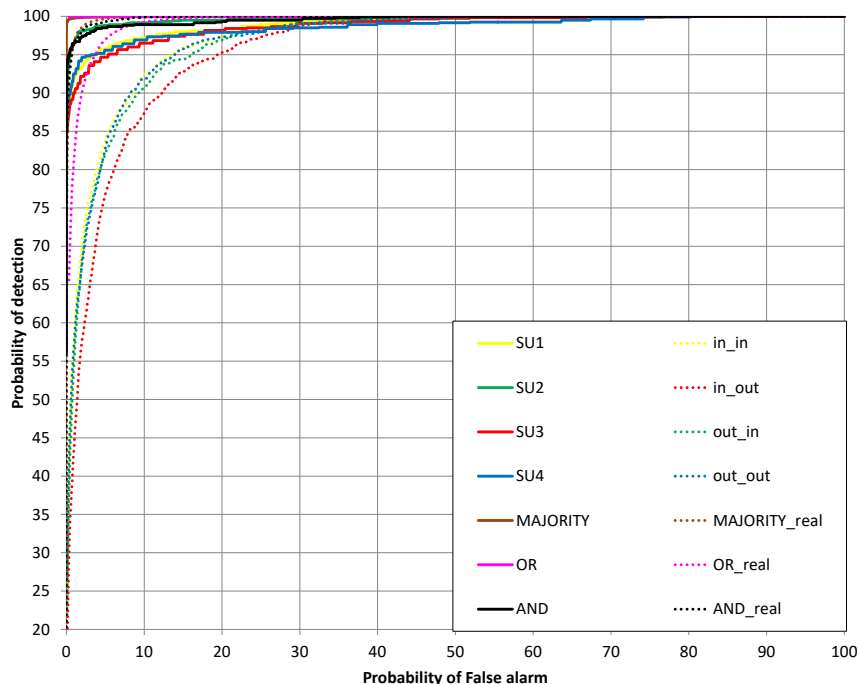
Fig. 4.4: ROC curves for FM received signal using ED test detector in real and simulated channels. Source: author.

individual user is achieved when PU is located outdoors whereas SU is indoor. Co-operative sensing gives very good results for all channel models. It can be observed that when the probability of false alarm equals 10 %, the probabilities of detection are 99.5 % for the OR rule, whereas it is approximately 100 %, for the AND, and MAJORITY rules. It can also be noted, that the performance of all cooperative fusion rules, after 4 % of false alarm probability, outperforms the simulated channels for individuals.

Fig. 4.5 and Fig. 4.6 describe the performance of individual and cooperative sensing in the case of transmitting an 8PSK signal in both the real and simulated channels using KS and ED detectors, respectively. In both cases, the results are quite good for cooperative sensing but it can be concluded that ED detection is more suitable for an 8PSK signal than the KS test.

As expected and evident from all presented figures, all cooperative fusion rules gave better detection performance than sensing by individual users. The MAJORITY rule results in slightly higher detection performance than AND and OR rules.
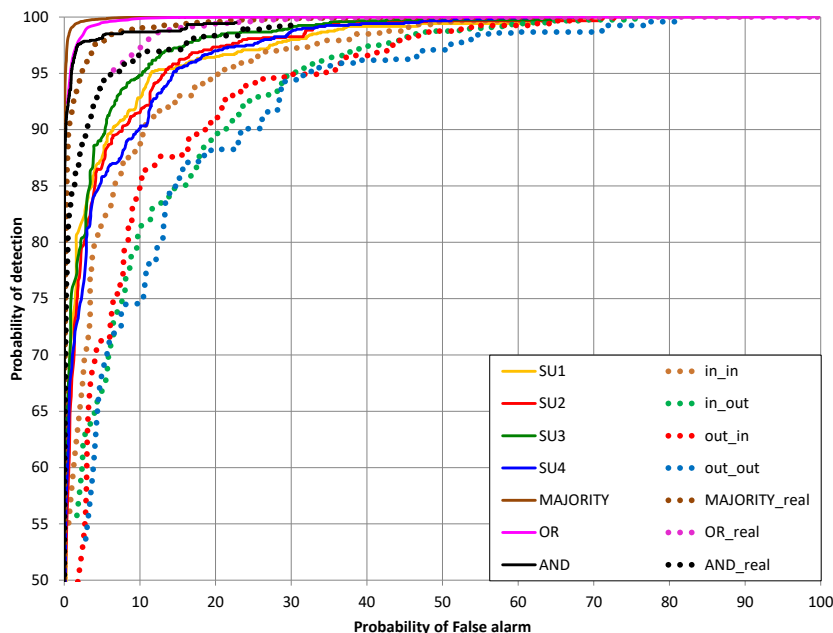
Fig. 4.5: ROC curves for PSK received signal using the KS test detector in real and simulated channels. Source: author.

For the MATLAB-based simulator, ED provides better detection than the KS detector for an 8PSK signal, whereas an FM signal gives the opposite results [115]. Whereas for the USRP-based setup, ED provides much better detection than the KS test for both signals (8PSK and FM). According to these results, two or more sensing techniques at the receiver side should be used. As is known, for the IEEE 802.22 standard, P_d should be 90 % or higher at $P_{fa} = 10$ % [117]. In our experiment, ED (SU2) for FM for the MATLAB-based simulator signal and KS detectors (SU2-SU4) for both FM and 8PSK for USRP-based setup do not meet these requirements, but all cooperative schemes operate in accordance with the requirements of the standard.

4.4 Conclusion

In this research, the usefulness of the spector sensing methods are declared. It is one of the promising technologies that can be used by D2D communication users in the LTE Advanced network to prevent harmful interference effects. It is able
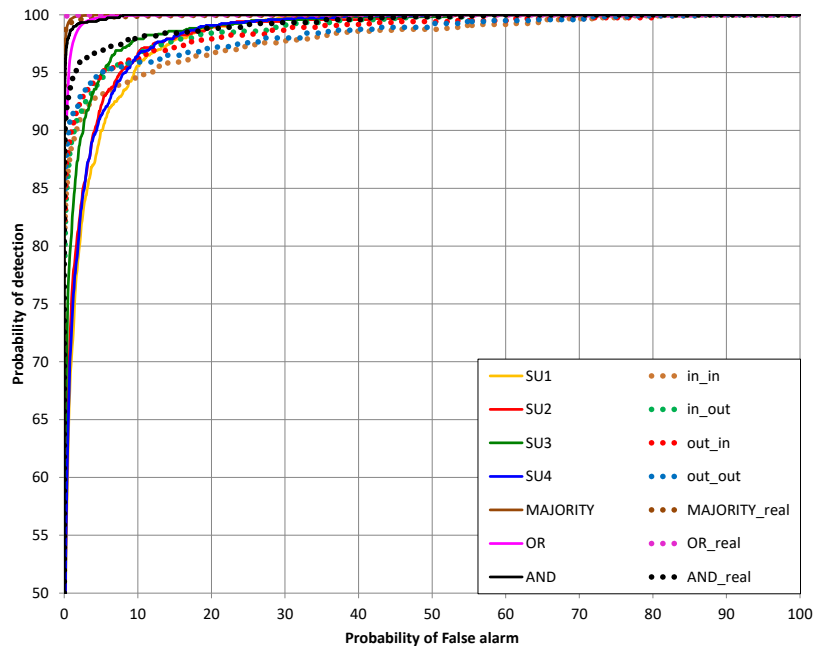
Fig. 4.6: ROC curves for PSK received signal using the ED test detector in real and simulated channels. Source: author.

to improve the quality of both D2D and LTE Advanced communication as well as utilizing the shared spectrum effectively. That leads to a higher overall network throughput. In order to test different methods of cooperative sensing and their effects on decision making, a MATLAB-based simulator in fading channel conditions has been created and presented. Its usefulness has been demonstrated by performance evaluation of two types of spectrum sensing detectors (ED and KS tests). In order to prove the trustworthiness of the implemented system, as a sample, two different signals were transmitted using the USRP devices. Different channel conditions, simulated (Ped A, Ped B, Veh A, Veh B) and real ones (indoor-indoor, indoor-outdoor, outdoor-indoor and outdoor-outdoor), are tested. The cooperative sensing system can be parametrized to a higher number of users for better decision making results. It can also transmit different signals.

5 D2D COMMUNICATION CHANNEL SOUND-ING

As a result of high speed data transmission, wireless services have grown very rapidly and become increasingly attractive. Therefore, wireless communication systems are deployed in various environments. In order to develop a good wireless Device to Device communication network [118, 119, 120], an accurate description of the channel impulse response (CIR) measurements should be presented. CIR describes spreading, or echoing, multipath propagation and Doppler effects that occur when an impulse is sent between the TX and the RX. Knowledge of the CIR characteristics enables system designers to ensure that inter symbol interference (ISI) does not dominate and hence lead to an excessive irreducible bit error rate [121].

Most of the channel sounding technique implementations in literature make use of expensive equipment such as a vector network analyzer, spectrum analyzer, and spread spectrum channel sounder [122, 123]. Therefore, part of this research will focus on developing an inexpensive, efficient and easy-to-use method for channel sounding. For these purposes, low cost hardware, USRP [124, 125], with open source software, GNU Radio [124], are deployed. This hardware is a part of SDR systems [126]. SDR reduces the value of the hardware by transferring its functions to software. Replacing signal processing, which is done by expensive hardware, by software requires only a personal computer. Therefore, it makes the process more effective and reconfigurable. However, the temporal resolution of the estimated CIR is limited by the small bandwidth of USRP [127, 128, 129]. For this reason, this device will be more effective in frequency domain channel sounding than using it in the time domain [130]. A frequency domain channel estimator is implemented the way that the carrier frequency is swept across a wideband channel to get a better temporal resolution of the estimated CIR [131]. Another part will present an outdoor long-range static channel campaign for both UHF and SHF bands with co-polarized horizontal and vertical antenna configurations. It investigates the channel characteristics of D2D communication scenarios underlaying 5G networks by providing detailed research.

There have been myriad studies for USRP channel sounding using different input signals over the past 10 years. As a sample of typical work in an indoor environment, there is a paper employing PN sequence with a length of 4095 chips [132]. This sounder consists of two separate USRPs. The measurements were done for both LOS and NLOS environments. Synchronization was achieved by a cable which connects the clocking port of a master USRP1 to a slave USRP1. Several multipath components were observed. A paper on indoor sounding [128] highlighted

the value of using a frequency domain sounder for measuring 100 MHz bandwidth characteristics. Sinusoidal signals were used as a transmitted signal. $K = 100$ CIR measurements were recorded. The received signal experienced between 43.42 dB and 67 dB of attenuation in different LOS distances (from 1 m to 27 m). Another paper used USRP N and USRP E series for indoor and outdoor channel measurements, respectively [127]. The indoor channel measurements were obtained using the sliding correlator system. Therefore, a pseudo-noise (PN) sequence of degree 10 ($N = 1023$) with a temporal resolution = 60 ns was transmitted. The path loss dynamic range between 45 and 105 dB and 61 ms of maximum multipath delay were observed. The outdoor channel measurements were obtained using the frequency domain channel sounding system. The measurements were performed in 10 discrete steps of 2 MHz and in the frequency band near 700 MHz. The path loss varies only by 5 dB in the 18 MHz band for LOS, while it varies by 20 dB for NLOS across the same frequency band. An open-pit mine campaign performed a 25 MHz wide frequency band sounding immediately below the unlicensed 2.4 GHz ISM band [133]. A continuously repeating maximum-length or m-sequences with $K = 2047$ sequence length was adopted as the transmitted signal. It was transmitted at a rate of 25 Msamples/s. Four measurement realizations of the impulse response with different TX-RX separations that vary between $425 - 1670$ m, were recorded. The delay spread of the channel was often more than 10 μs.

Some USRPs channel sounders constructed and implemented in the above papers use a sinusoidal signal for sounding, which is not suitable for time-varying channels. Since it suffers from relatively slow scanning speed due to sequential scanning of frequency points. Other papers sound the channel using different orthogonal signals in the time domain. However, it is hard to achieve excellent auto and cross correlation properties for CDM based channel sounding. In order to overcome these drawbacks, the frequency domain Zadoff-Chu sequence is proposed. Its center frequency is swapped across the measured bandwidth. In this research it is used for indoor channel sounding.

In the case of outdoor measurements, the number of studies for channel sounding have also been carried out. Outdoor measurements were conducted in an open-area test site at the National Metrology Institute of Germany [145], to study the scattering effects of traffic signs on vehicles moving along a road. The outputs are analytical models, simulations, measurements, and implementation of the bi-static radar cross section (RCS) of the traffic signs. A paper on outdoor sounding [146] highlighted the propagation path loss models for 5G urban micro and macro cellular scenarios. It compares the alpha-beta-gamma (ABG) and the close-in (CI) free space reference distance models. A wide range of frequencies $2 - 73.5$ GHz over $5 - 1429$ m distances were used. The output showed very comparable modeling performance between CI

and ABG models. The CI model offers simplicity and a conservative NLOS path loss estimate at large distances, whereas the ABG model is more complex and offers a fraction of a dB smaller shadow, predicting less loss near the transmitter, and more loss far from TX. Another paper [147], described the achieved results for LOS and NLoS measurements between the UE and the BS in Nanjing Road, Shanghai. The received signals were 20 MHz bandwidth with 2.1376 GHz carrier frequency. The delays and complex attenuations of multipath components have been estimated by applying the generalized expectation-maximization (SAGE) algorithm. The distance between TX and RX in LOS/NLOS scenarios, the life-distance of LOS channel, the power variation at LOS to NLOS transition, and the transition duration were extracted. The authors in [148] presented a sounding system that uses an orthogonal frequency division multiplexing signal at 5.6 GHz with 200 MHz bandwidth. The power delay profiles and the excess delay were presented. A channel measurement campaign was conducted to study the frequency dependence of the propagation channel for a wide range of frequencies $3 - 18$ GHz [149]. Urban macro and micro cellular environments were covered. The RMS delay spreads, coherence bandwidth, path loss, shadow fading, and Ricean factor were characterized. It is mentioned that the path loss exponents vary significantly with frequency (from 1.8 to 2 dB in LOS environment and from 2.71 to 4.34 dB in NLOS). Shadow fading and the Ricean factor increase with frequency, whereas the RMS delay spread values decrease with frequency in the LOS environment. However, the RMS spread delay in the NLOS environment and the coherence bandwidth values in both LOS and NLOS environments do not show significant changes. An outdoor wideband channel sounding at 2.4 GHz is described in [150]. The distance between the transmitter and the receiver varied from 50 to 150 m. The distance-power gradient (2.532), path loss (with 9 dB standard deviation), and small-scale or multipath fading (with 5 dB standard deviation) are reported. The maximum observed multipath fade is 28 dB. Another campaign was conducted in Seoul [151]. The measurements were done using a wideband channel sounder at 3.7 GHz with a 100 MHz bandwidth. Both LOS and NLOS environments were investigated. The output was presented as a spatial correlation coefficient (SCC) of low-height links in urban environment. Wideband propagation channel at 2.45 and 5.2 GHz was presented in [152]. Channel characteristics as power delay profile, the mean delay, and the delay spread were studied. It was mentioned that the parameters are frequency independent, whereas the higher frequency signal shows considerably larger path loss than the lower one. Both the correlator-based and recursive-Bayesian-filter-based ranging estimators were evaluated; both of them provide better performances at 2.45 GHz compared with 5.2 GHz. This difference increases with decreasing the received power. Urban macro environment was investigated in [153]. Wideband MIMO measurements around 800 MHz with 50 MHz

bandwidth were presented. The antennas with 360 degrees of azimuth and 90 degrees of elevation were used for the transmitter and the receiver. The output report contains path loss (path loss exponent n = 3), shadow fading (with 8.4 dB standard deviation), delay spread (with 123 ns mean value and 73.2 ns standard deviation), angular spread (with 30.8 degree mean value and 12.5 degree standard deviation for angular spread of departure and 66.9 degree mean value and 15.1 degree standard deviation for angular spread of arrival), and Ricean K-factor (with 5 dB mean value and 6.7 dB standard deviation). Measurement campaign [154] at the center frequency of 2.35 GHz with 50 MHz bandwidth was conducted in order to evaluate the performance in an outdoor propagation environment. SNR, spatial diversity and capacity of different transmission schemes (direct transmission (DT), amplify-and-forward (AF) and decode-and-forward (DF) relaying) were investigated. Both LOS and NLOS scenarios were involved. The results are depicted in terms of SNR, spatial diversity, and capacity. Both AF and DF schemes improve the SNR, whereas DT improves the capacity in small distances of LOS environment. However, by increasing TX-RX distance, the capacity provided by the DF exceeds that provided by the DT. Spatial diversity was also significantly improved by applying the DF scheme.

The main contributions of this chapter are described in the following few points:

- Present an overview about the LAS code used for TX-RX synchronization.
- Propose a method for channel sounding that can be used with low-cost commercially available SDRs and be able to support D2D communication [128].
- Implement a Zadoff-Chu frequency domain channel sounder using USRP and MATLAB platforms in order to support wide bandwidth and fast channel capturing.
- Test the proposed technique in real indoor channel conditions and compare it with frequency domain sounding.
- Test the ability of deploying a D2D communication underlay 5G network in wideband long-range static channel for both UHF and SHF bands as a part of 5G NR frequency bands allocation.
- For microcell LOS environment (with 315 m distance), we provided the channel frequency response (CFR) variation, path loss, and RMS delay spread distribution in the case of vertical and horizontal polarizations for both 1.3 GHz and 5.8 GHz center frequencies.
- For macrocell NLOS environments (with 2.089, 4.11, and 5.429 km distances), in addition to all previous mentioned parameters, distance dependence of path loss, and RMS delay spread are analyzed. RMS delay spread dependence of the coherence bandwidth is also investigated.

The chapter is organized as follows. Section 5.1 presents a brief overview of

channel sounding methods. The LAS codes used for USRP TX-RX synchronization are also depicted. Then a brief overview about the characteristics of Zadoff-Chu sequences is described. Afterwards, the proposed method of channel sounding is formulated and compared with basic frequency domain sounding. Using the proposed method, the basic channel characteristics like RMS delay spread, mean excess delay and coherence bandwidth are extracted. The path loss of the measured channel is also studied. This approach can be used in e.g. vehicle channels for D2D communication. Finally, wideband UHF and SHF long-range static outdoor channel characterization are depicted. Distance dependency of path loss, RMS delay spread, its dependency to TX-RX distance, and its relation to the coherence bandwidth are derived.

Author's bibliography related to this chapter:

[1] Kassem, E., Marsalek, R., & Blumenstein, J. (2018). Frequency Domain Zadoff-Chu Sounding Technique for USRPs. In *25th International Conference on Telecommunications (ICT)*, IEEE.

[2] (In review) Kassem, E., Blumenstein, J., Povalac, A., Vychodil, J., Pospisil, M., Marsalek, R., & Hruska, J. (2018). Wideband UHF and SHF Long-Range Static Channel Characterization. In *International Journal of Antennas and Propagation.*

5.1 Channel Sounding Methods

The channel sounding methods are time domain, frequency domain and code domain. Time division multiplexing will not be covered because of poor real time measurements and absolute time synchronization between transmitter and receiver is required.

5.1.1 Code Division Multiplexing (CDM)-based

Code division multiplexing sounders is considered as an efficient way for measuring fast fading channels. Several codes can be used as a probing signal for the CDM sounder like loosely synchronous, Large Area LA, Large Area Synchronized LAS, CAZAC, Kasami [136], and Chaotic sequences.

Large Area codes $LA(L_{LA}, M_{LA}, K_{LA})$ is a set of codes which consist of ± 1 or 0 elements where large area sequence with a total code length L_{LA}, K_{LA} number of ± 1 pulses, and minimum spacing of M_{LA} chip durations between non-zero pulses. However, the main drawback of these sequences is their relatively low duty ratio, quantifying the density of the nonzero pulses, since this limits the number
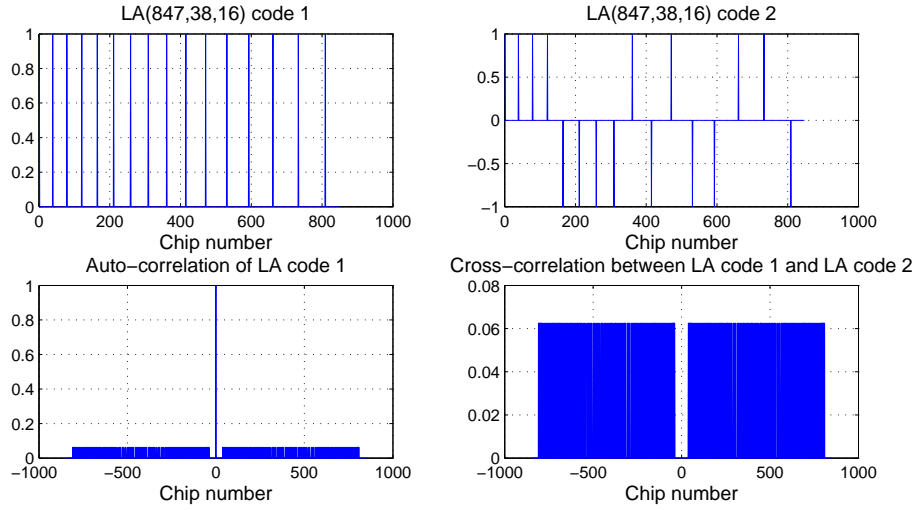
Fig. 5.1: Two orthogonal LA codes with the same length, number of pulses, and chip durations and their characteristics (both auto-correlation and cross correlation). Source: author.
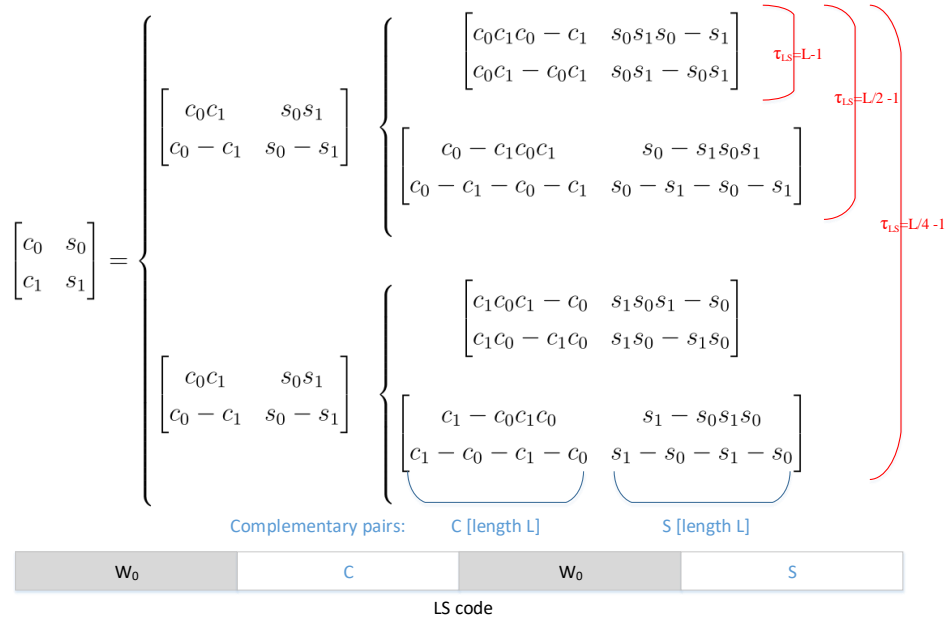
Fig. 5.2: Description of complementary and loosely synchronous codes generation where C and S are complementary codes, W_{LA} the number of zeros, and τ_{LS} is an interference free window.

of codes available, therefore the number of users are also limited [116]. For example, LA(847,38,16) code is 847 chips long, the minimum separation between nonzero elements is 38 and the number of impulses is 16. This code is described in Fig. 5.1.
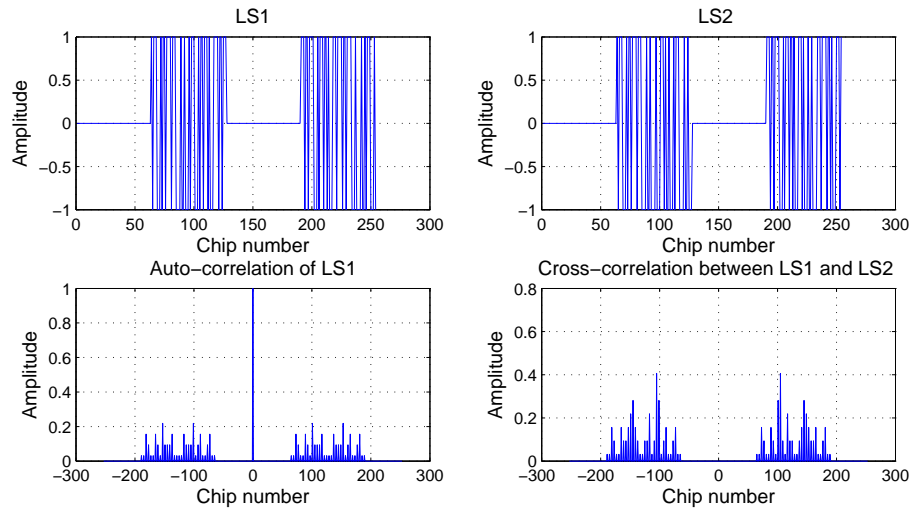
Fig. 5.3: Two orthogonal loosely synchronous codes with the same length equal to $N_{com} = 64$, number of zeros $W_{LA} = 63$, and their characteristics (both auto-correlation and cross correlation). Source: author.
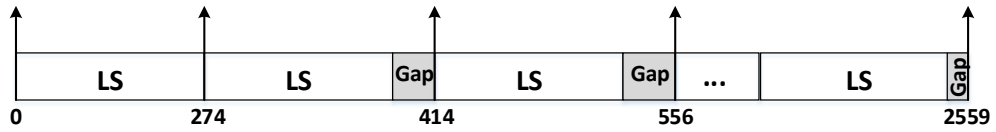
Fig. 5.4: Generation of LAS code with a length equal to 2559 chips. Source: author.
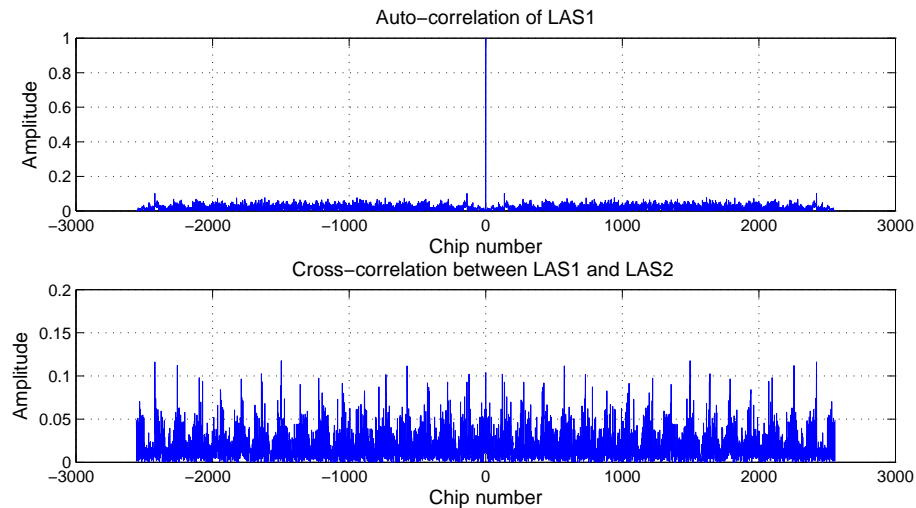
Fig. 5.5: Auto and cross correlation characteristics of LAS codes. Source: author.
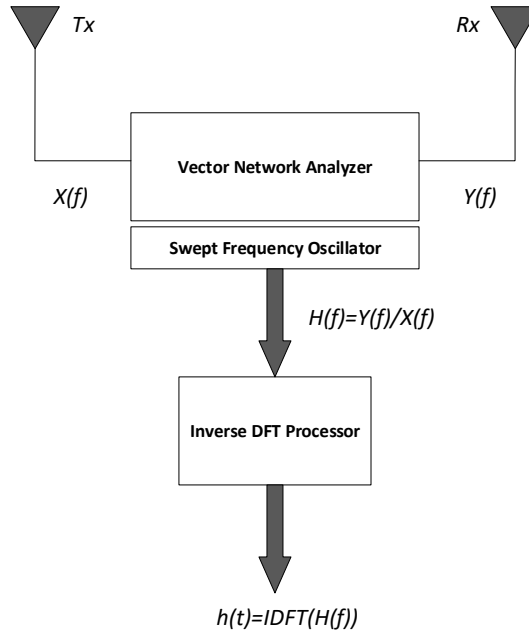
Fig. 5.6: Frequency domain channel impulse response measurement system [134].

Loosely synchronous code is based on orthogonal and complemented Golay complementary pairs (C0,S0) and (C1, S1). It can eliminate the associated ISI as well as the multiple access interference (MAI) properties. This code can be given as $LS(N_{com}, P_{LS}, W_{LS})$, where N_{com} length of complementary codes, W_{LA} is the number of zeros which separates between two pairs of complementary codes, and P_{LA} is a dimension of the Walsh-Hadamard (WH) matrix which can be applied to generate an orthogonal complementary code sets. Figure 5.2 describes loosely synchronous codes generation procedure, whereas Fig. 5.3 depicts their characteristics.

LAS code [135] is a combination of both LA code and loosely synchronous code. In order to design LAS code, loosely synchronous code is inserted into zero space of LA code, so it enhances the duty ratio of LA code, and optimizes the feature of "Zero Interference Window". Figure 5.4 describes LAS code structure, whereas Fig. 5.5 depicts their auto and cross correlation properties.

5.1.2 Frequency Domain Sounding

The frequency response can be measured directly by collecting the measurements of radio propagation characteristics in the frequency domain. It can also be calculated by applying the Fourier transformation on the time domain measurements expressed in Eq. 2.1. The result could be given by Eq. 5.1 [44].

$$H(f,t) = \int_{-\infty}^{\infty} h(t,\tau) \cdot e^{-j\omega\tau} d\tau$$
$$= \sum_{w=1}^{N_p} a_w(t) e^{-j\varphi_w(t)} e^{-j\omega\tau_w(t)} \tag{5.1}$$

where ω is the carrier frequency in radians per second. In a slowly time-varying channel, the multipath parameters of the channel remain constant during fractions of the coherence time of the channel, so that the frequency response can be measured as follows:

$$H(f) = H(f,0) = \sum_{w=1}^{N_p} a_w e^{-j\varphi_w} e^{-j\omega\tau_w} \tag{5.2}$$

In practice, however, the measurement systems are band-limited. Therefore, the frequency response is defined in Eq. 5.3.

$$H(f) = H(f,0) = W(f) \cdot \sum_{w=1}^{N_p} a_w e^{-j\varphi_w} e^{-j\omega\tau_w} \tag{5.3}$$

where $W(f)$ represents the frequency domain RF filter characteristics used in the measurement system [44].

Practically, the channel response is measured by using a network analyzer that sweeps a transmitted RF frequency with fixed power over the bandwidth of interest. Then it measures the amplitude and the phase of the received signal passed through the radio channel [44, 127, 128]. This frequency response is used for calculating the time domain response and multipath parameters using inverse discrete Fourier transform (IDFT). Figure 5.6 depicts the block diagram of the frequency domain sounding system.

The number and spacing of the frequency step impacts the time resolution of the impulse response measurement. This system is more suitable for indoor non real-time measurements. Hence, it is not suitable for time-varying channels unless the sweep times are fast enough.

5.2 Zadoff-Chu Sequence

Zadoff-Chu [137, 138] is a complex-valued mathematical sequence, when applied to radio signals, gives rise to an electromagnetic signal of constant amplitude. The u root Zadoff-Chu sequence is defined by Eq. 5.4 [139, 140, 141].

$$x_u(n) = \begin{cases} \exp\left(-j\frac{\pi u n(n+1)}{N_{ZC}}\right) & \text{for odd u} \\ \exp\left(-j\frac{\pi u n^2}{N_{ZC}}\right) & \text{for even u} \end{cases} \tag{5.4}$$

where N_{ZC} is the length of the Zadoff-Chu sequence. This sequence is a CAZAC se-
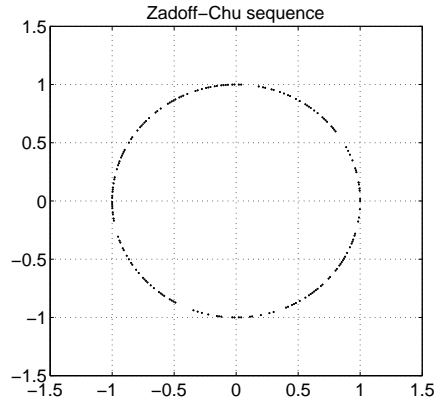
Fig. 5.7: Constant amplitude property of Zadoff-Chu sequence. Source: author.

quence [142, 143] (constant amplitude zero auto-correlation waveform) [143]. There-
fore, it has several important properties. Constant amplitude means that it has flat
frequency domain response. Figure 5.7 demonstrates the constant amplitude of the
Zadoff-Chu sequence with $u = 29$ and the length of the sequence $N_{ZC} = 353$. This
property of the Zadoff-Chu sequence formulates the basis of this research. Zero auto-
correlation: Zadoff-Chu sequences are one of the best poly-phase sequences. Their
periodic auto-correlation function is perfect. That means, the auto correlation is zero
for all time lags except for the zero lag. These sequences exhibit the useful property
that cyclically shifted versions of themselves are orthogonal to one another. If two
Zadoff-Chu sequences are created, one of them is a shifted copy of another by N_{sh}
(N_{sh} can be 1,2, ..., $N_{ZC} - 1$). The correlation between these sequences will be zero.
Therefore, two sequences are orthogonal to each other. It means that you can create
$N_{ZC} - 1$ orthogonal sequences just by shifting a Zadoff-Chu sequence. Zadoff-Chu
sequences are used in 3GPP LTE Long Term Evolution [139] air interface in the
Primary Synchronization Signal (PSS), random access preamble (PRACH), uplink
control channel (PUCCH), uplink traffic channel (PUSCH), DMRS, and sounding
reference signals (SRS).

5.3   Data Processing

The radio channel is commonly characterized by scattering, attenuation, reflection,
refraction and fading [134]. Studying radio channels make us have an understanding
of the rapid fluctuations of the radio signal amplitude over a period of time. In digital
communications, the additive white Gaussian noise (AWGN) channel is assumed as
a basic channel model. More advanced models including fading effects, e.g. the
ITU path loss models [42], are often used in order to better reflect real wireless

environments.

5.3.1   Channel Response

The impulse response h of the multipath channel can be calculated according to Eq. 2.1, where a_w, τ_w, and φ_w, represent the amplitude, arrival time, and phase respectively, and characterizes N_p number of individual paths between the transmitter and receiver [42].

5.3.2   RMS Delay Spread

The RMS delay spread is one of the most important parameters for the delay time extent of a multipath radio channel. It is caused by reflected and scattered propagation paths. It can describe different multipath fading channels and a guideline to design a wireless transmission system. If τ_w is the channel delay of wth path and $P(\tau_w)$ is its power, then the root mean square delay spread can be formulated in Eq. 5.5.

$$\sigma_\tau = \sqrt{\bar{\tau^2} - \bar{\tau}^2} \tag{5.5}$$

where $\bar{\tau}$ is the mean excess delay and it is given by Eq. 5.6.

$$\bar{\tau} = \frac{\sum\limits_{w=1}^{N_p} a_w^2 \tau_w}{\sum\limits_{w=1}^{N_p} a_w^2} = \frac{\sum\limits_{w=1}^{N_p} P(\tau_w)\tau_w}{\sum\limits_{w=1}^{N_p} P(\tau_w)} \tag{5.6}$$

$$\bar{\tau^2} = \frac{\sum\limits_{w=1}^{N_p} a_w^2 \tau_w^2}{\sum\limits_{w=1}^{N_p} a_w^2} = \frac{\sum\limits_{w=1}^{N_p} P(\tau_w)\tau_w^2}{\sum\limits_{w=1}^{N_p} P(\tau_w)} \tag{5.7}$$

5.3.3   Coherence Bandwidth

Coherence bandwidth is a statistical measure of the range of frequencies over which the channel can be considered as a flat channel. In other words, coherence bandwidth is the range of frequencies over which two frequency components have a strong potential for amplitude correlation. In the case where coherence bandwidth is defined as a bandwidth with correlation of 0.5 or above, it can be calculated using the frequency correlation function depicted in Eq. 5.9

$$S(\Delta f) \cong \int_{-\infty}^{\infty} H(f)H^*(f + \Delta f).df \tag{5.8}$$

$H(f)$ is the complex transfer function of the channel, Δf is frequency shift and * denotes the complex conjugate.

$$B_c \approx min(\Delta f : \frac{S(\Delta f)}{S(0)} < 0.5) \tag{5.9}$$

It can also be calculated by applying Eq. 5.10 [44].

$$B_c \approx \frac{1}{5\sigma_\tau} \tag{5.10}$$

5.3.4 Path Loss

The generalized form of the path loss model can be constructed from path loss offset PL_{offset}, the distance between TX and RX d, the reference distance d_0, and the random shadowing effect χ_σ (the deviation of the measured path loss from the linear model), and calculated by Eq. 5.11.

$$PL(d) = PL_{offset} + 10n \cdot \log(\frac{d}{d_0}) + \chi_\sigma \tag{5.11}$$

where n is a path loss exponent and $d_0 = 1$ m and $d_0 = 100$ m for short indoor and long outdoor distances [134].

5.3.5 Channel Frequency Response Variation

Let us consider that $H_s(f_k)$, $k = 1, 2, \cdots N_F$, $s = 1, 2, \cdots, N_T$ is the wideband CFR at a specific time for a specific frequency. N_T is the number of normalized CFR samples and N_F is the number of frequency steps in the measured bandwidth. The influence of variation and small scale fading can be removed by averaging consecutive N_T CFRs [155] according to Eq. 5.12.

$$\overline{\left|H(f_k)\right|^2} = \frac{1}{N_T} \cdot 10 \cdot \log(\sum_{s=1}^{N_T} \left|H_s(f_k)\right|^2) \tag{5.12}$$

However, as is mentioned in [156], averaging keeps some small scale fluctuations in the frequency domain; therefore, the median filter is applied. Note that in order to get a well filtered signal, a proper window size of median filter (that keeps the deep fades effect) should be chosen. In this research, the window size will depend primarily on deep fades where the signal strength can drop by more than 15 dB. Finally, the CFR variation is obtained through subtracting the filtered average CFR from the measured CFR.

$$CFRV = \left|H_s(f_k)\right|^2 - filt(\overline{\left|H(f_k)\right|^2}) \tag{5.13}$$

Tab. 5.1: Parameters summary

Parameters	Values
Bandwidth	100 MHz
Transmitted signals	Sinusoidal, Zadoff-Chu
Channel models	Cable, LOS indoor, NLOS indoor
Sample rate	10 Msamples/s
Frequency	800-900 MHz

5.4 Indoor Testbed Description

The system used to test the suggested sounder is depicted in Fig. 5.8. It consists of two PCs and two USRP2 devices. One of these USRPs is implemented as a transmitter. It carries out its role by transmitting two signals. These signals are: a sinusoidal signal which is used for the frequency domain channel sounding and the Zadoff-Chu sequence for the proposed channel sounding method. The second USRP2 is implemented as a receiver. For 14 different indoor locations, the receiver recorded baseband signal samples at 10 Msamples/s, then the samples are stored in the laptop's harddrive. Both the transmitter and receiver are connected to the PC through a Gigabit Ethernet port (blue line). Note that the precise synchronization between the USRPs must be realized in order to derive high dynamic range channel impulse responses. Synchronization between the transmitter and the receiver is achieved by transmitting an orthogonal code (LAS code) [116] at the beginning of each signal's burst.

In the setup, each USRP is equipped with a WBX RF-board, which covers the 50 MHz - 2200 MHz frequency range. For different channel model realizations, the receiver antennas are allocated in different locations. Three different channel scenarios are considered. The signals are captured in a good isolated cable, an indoor LOS channel, and an indoor NLOS channel. Both transmitter and receiver are located inside the building. The PC is running Fedora 16 and signal processing applications are done using open-source GNU Radio version 3.7.2.1. The Zadoff-Chu sequence, which is generated in MATLAB, is recorded into the data files for transmission in GNU Radio.

The frequency domain channel sounding is done by transmitting narrowband sinusoidal signals which are spaced by $\Delta f = 100$ kHz. In order to measure the whole 100 MHz band (800-900 MHz), the carrier frequency f_{ci} is swept across the bandwidth in N_{step_fr} discrete steps, $i = 1, 2, ..., N_{step\_fr}$ where $N_{step\_fr} = 1000$.
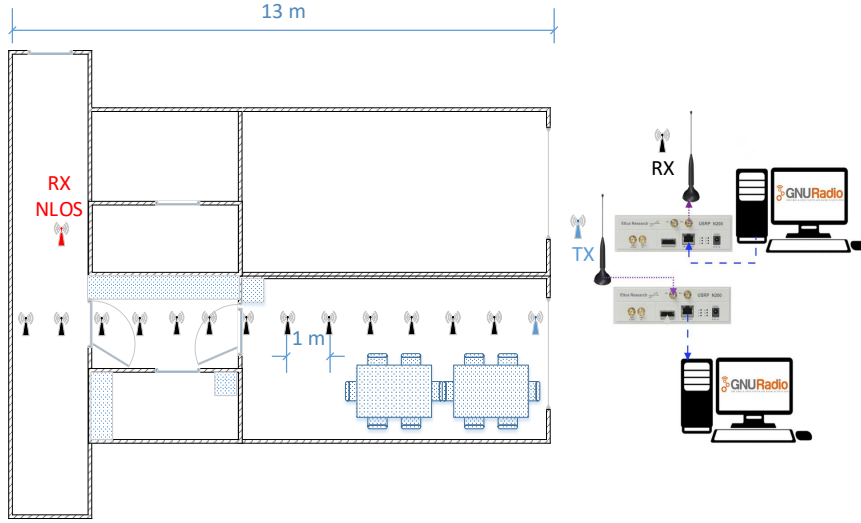
Fig. 5.8: Map of the indoor environment; 3rd floor with one TX location and 14 RX locations. The blue antenna symbol represents the TX location, whereas the black ones represent the RX locations. The red antenna symbol represents the RX location in the case of NLOS. On the top, the equipment used for the transmitter and the receivers are presented. Source: author.

For each frequency step, a signal frame consisting of $N_{fr\_sin} = 2000$ samples is received by USRP. The system initially sets the carrier frequency to f_{c1}=800 MHz and after receiving a frame of N_{fr_sin} samples, it increases the carrier frequency by Δf =100 KHz. The frequency sweep process between both the transmitter and the receiver is synchronized.

On the other hand, the proposed method of channel sounding is achieved by transmitting frames of Zadoff-Chu sequences. Each transmitted sequence covers 2 MHz bandwidth, therefore, the frames are spaced by $\Delta f = 2$ MHz. In order to measure the whole 100 MHz band (800-900 MHz), the center carrier frequency f_{cci} is swept across the bandwidth in N_{step_ZC} discrete steps, $i = 1, 2, ..., N_{step\_ZC}$ where $N_{step\_ZC} = 50$. Each frame consists of $N_{fr\_ZC} = 2000$ samples of 2 MHz signals. By taking into consideration the constant amplitude of this signal, the channel response can be calculated.

Each frame of the above generated signals is detected by the threshold detection of the received signal power. Afterwards, the extracted signal is saved to a data file and sent to the PC. Then the signal is analyzed to extract the magnitude and the phase which characterize the channel response at a specific frequency f_{ci} (frequency sounder) or 2 MHz bandwidth (frequency domain Zadoff-Chu sounder). The $800 - 900$ MHz band is used because it is a part of the 5G NR FDD uplink
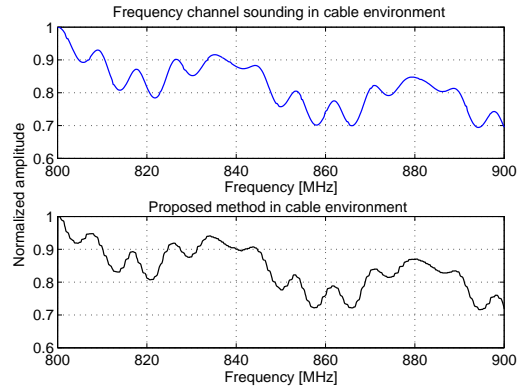
Fig. 5.9: Frequency channel response for both frequency (blue curve) and proposed (black curve) channel sounding method for a cable and WBX boards. Source: author.

frequency bands allocation [144], so it is suitable for D2D underlay LTE Advanced or even 5G networks. However, the proposed method is not limited to this band and its applicability depends mainly on the used RF front-end.

Figure 5.9 describes the frequency channel responses between the transmitter and the receiver which are connected by a cable. The blue curve depicts the results achieved by using the frequency domain channel sounding while the black curve is the same frequency channel response using the frequency domain Zadoff-Chu channel sounding. Both curves are normalized to the maximum response value.

The achieved results in Fig. 5.9 can be useful in order to estimate the frequency characteristics of both the cable and WBX board for the whole range of taken measurements. This response can be easily subtracted from the LOS and NLOS channel responses to get pure channel characteristics without a cable and front end affections.

Figure 5.10 depicts the response of the indoor LOS channel. There is a direct path from the source to the receiver about 13 m length. Figure 5.11 presents the response of indoor NLOS channel where the path between both the transmitter and the receiver is obstructed by a wall. The distance between both sides is also 13 m. Both LOS and NLOS cases are depicted in Fig. 5.8 where the blue antenna is TX and the black and red antennas are RXs. All above presented curves show that the proposed method is able to measure the channel with the same accuracy as a frequency domain channel sounding. The root mean square error is calculated to compare both methods in different environments. The results of $8.7 \cdot 10^{-3}$, $2.4 \cdot 10^{-2}$, and $5.2 \cdot 10^{-2}$ are achieved for cable, LOS, NLOS environments, respectively.

For deeper channel characterizing, several measurements in an indoor environment for different LOS distances (1 m - 13 m) between the transmitter and the
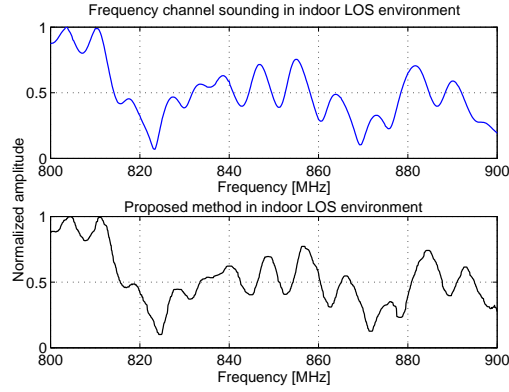
Fig. 5.10: Frequency channel response for both frequency (blue curve) and proposed (black curve) channel sounding method for the LOS indoor environment. Source: author.
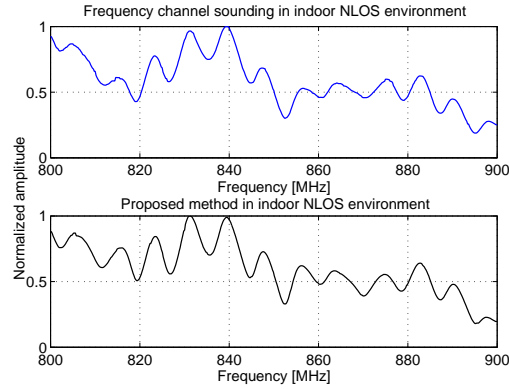
Fig. 5.11: Frequency channel response for both frequency (blue curve) and proposed (black curve) channel sounding method for the NLOS indoor environment. Source: author.

receiver were also conducted. For each distance and frequency between 800 and 900 MHz, 110 CIR measurements are extracted. Figures 5.12 to 5.16 capture channel characteristics by analyzing 110 CIR measurements of 100 MHz band at 3 m, 5 m, 8 m, and 13 m distances.

Figure 5.12 presents the channel impulse response, whereas Fig. 5.13 depicts the variation of channel excess delay (blue curve) for the 110 captures of the measured channel. While the red line depicts the mean excess delay value. The maximum and the minimum observed excess delay values are (2 ns and 0.6 ns), (2 ns and 0.6 ns), (1.765 ns and 0.704 ns), and (1.77 ns and 0.57 ns) for 3 m, 5 m, 8 m, and 13 m distances, respectively. The mean access delay values are 1.24 ns, 1.33 ns, 1.3 ns, and 1.21 ns. Figure 5.14 depicts the variation of RMS delay spread with their mean value of above described channel. The RMS delay spread varies between (3.58 ns
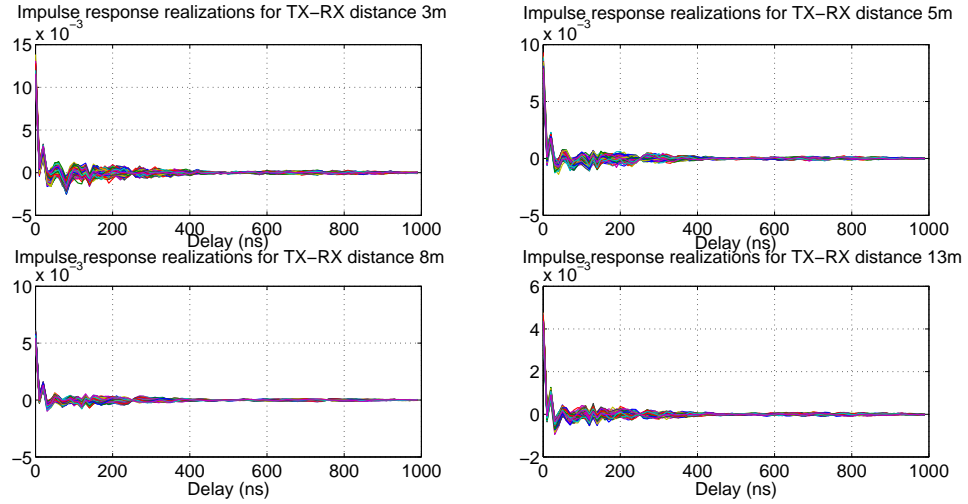
Fig. 5.12: Channel impulse response for 110 CIR measurements of the LOS channel for TX-RX separation d = 3 m, 5 m, 8 m, or 13 m. Source: author.
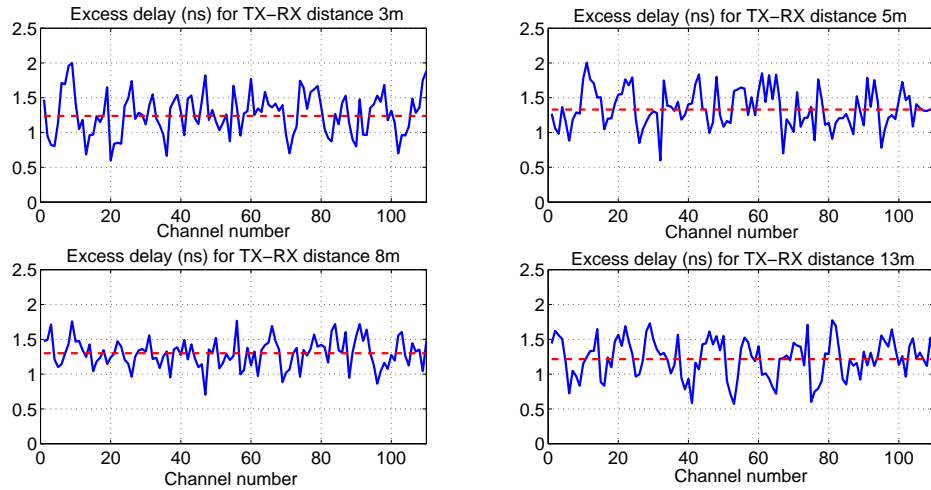
Fig. 5.13: Excess delay for 110 CIR measurements of the LOS channel where TX-RX separation d = 3 m, 5 m, 8 m, or 13 m. The red line represents the mean excess delay. Source: author.

and 6 ns), (3.8 ns and 6 ns), (3.69 ns and 5.67 ns), and (3.33 ns and 5.69 ns) and mean values are 4.693 ns, 4.907 ns, 4.912 ns, and 4.7 ns for 3 m, 5 m, 8 m, and 13 m distances, respectively. Figure 5.16 describes the variation of channel energy with the mean and deviation values captured as green and red lines, respectively. The mean channel energy power values equal to -38.35 dB, -41.94 dB, -45.06 dB, and -47.27 dB for 3 m, 5 m, 8 m, and 13 m distances, respectively.

Using the measured CIRs, the mean excess delay (red curve), mean RMS delay spread (black curve) and coherence bandwidth (blue curve) of the 100 MHz channel
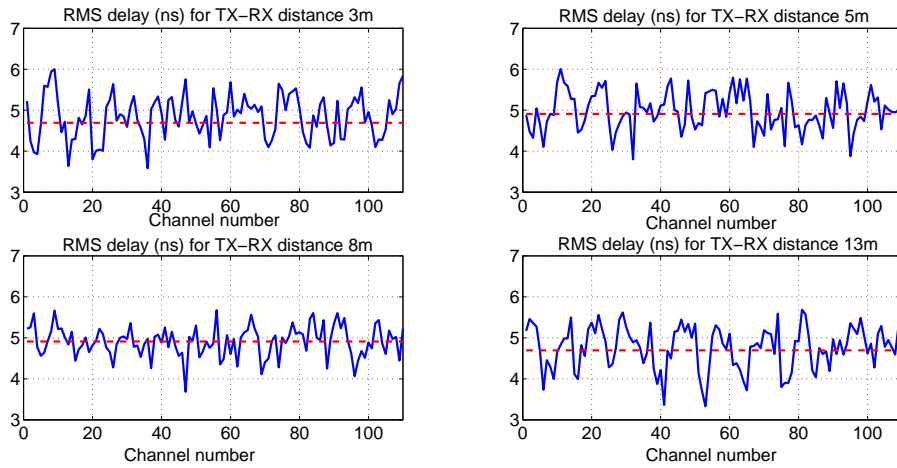
Fig. 5.14: RMS delay for 110 CIR measurements of the LOS channel where TX-RX separation d = 3 m, 5 m, 8 m, or 13 m, are depicted as a blue curve. The red lines represent the mean RMS delay value. Source: author.
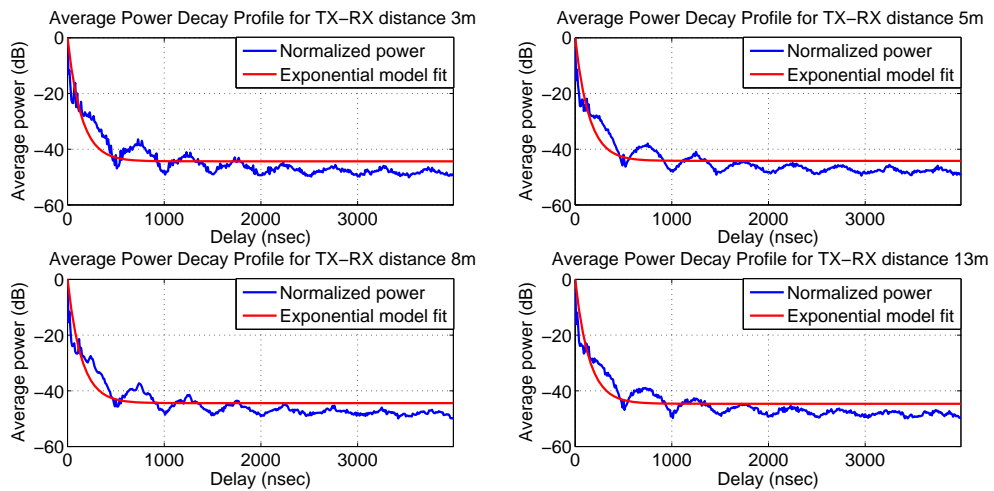
Fig. 5.15: The normalized average power for 110 CIR measurements of the LOS channel, where TX-RX separation d = 3 m, 5 m, 8 m, or 13 m, are depicted as a blue curve. The red curves are the best fit exponential power delay profile. Source: author.

are calculated and captured in Fig. 5.17 as a function of distance. It can be observed that the RMS delay of the channel increases with an increase in distance, causing the coherence bandwidth to decrease significantly.

Figure 5.18 shows the measured path loss (red circles) as a function of distance and the best line fit to the measured values (blue line). The black triangles present the median values of the measured path loss across different TX-RX separations.
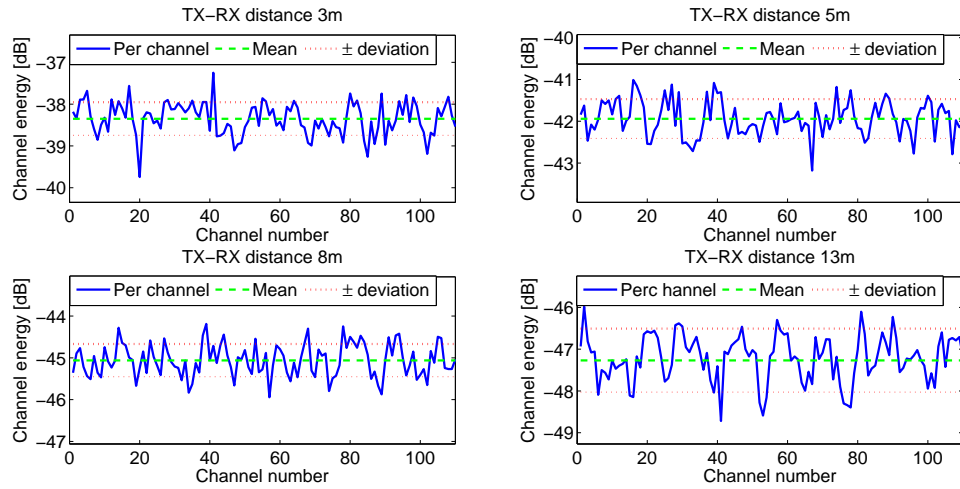
Fig. 5.16: Channel energy values for 110 CIR measurements of the LOS channel where TX-RX separation d = 3 m, 5 m, 8 m, or 13 m are depicted as a blue curve. The green lines represent mean values, whereas the red lines represent the deviation of the energy. Source: author.
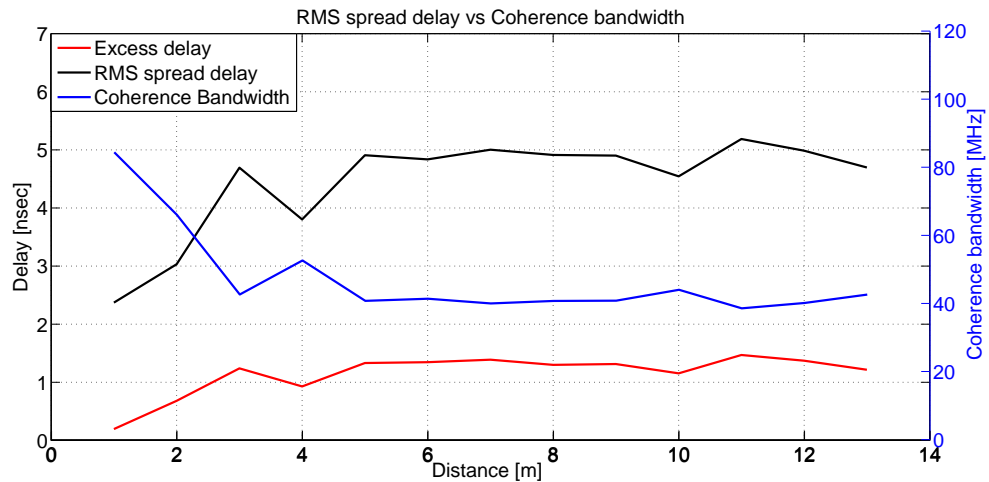
Fig. 5.17: The measured characteristics of 100 MHz channel bandwidth of the indoor LOS environment for TX-RX separations 1 - 13 m. The red, black and blue curves represent the mean excess delay, RMS delay spread and the coherence bandwidth, respectively. Source: author.

The best line fit have been produced using a MATLAB function with a channel exponential $n = 1.67$ and $PL_{offset} = 30.5$ dB. The exponential of the channel $n = 1.67$ is observed to be less than the free-space path loss exponent $n_{FS} = 2$. This could be due to walls of the corridor being close to each other that may cause strong reflections and refractions for LOS scenarios.
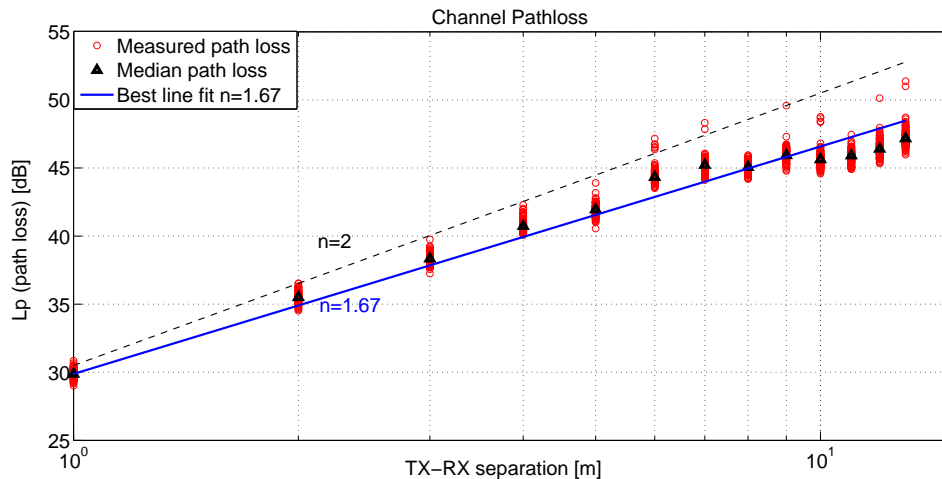
Fig. 5.18: The measured path loss for 100 MHz channel bandwidth of the indoor LOS environment. Each red circle represents the measured LOS path loss value; black triangle represents the median value of the measured path loss for specific distance; the blue line represents the channel path loss model for path loss exponent equaling 1.67 and $d_0 = 1$ m. Source: author.

5.5 Outdoor Testbed Description

These measurements were conducted in the region South Moravia, Czech Republic. Two types of setups, microcell and macrocell, were considered. In the microcell setup, TX1 was placed on a small hill near the Faculty of Electrical Engineering and Communication building, Brno University of Technology (BUT) and mounted on a mast of 10 m height, whereas the receiver was allocated on the rooftop of the building (19 m height). The distance between the transmitter and the receiver for route 1 (R1) is 315 m. Both the transmitter and the receiver are surrounded by a rich scattering environment which consists of buildings, parked cars, moving cars and people. However, because of the highly mounted antennas above the ground, LOS measurements were realized. In the macrocell setup, three different NLOS routes were tested (R2, R3, R4). On the first two routes (R2, R3), the receiver was placed on the rooftop of the Faculty of Electrical Engineering and Communication building. The transmitter was located 2.089 km from the receiver (8 m height) for the R2 route, and 5.429 km far from the receiver of 3 m height in the case of the R3 route. For the fourth route, R4, both the transmitter and the receiver were located in a rural area where the transmitter was surrounded with different levels of buildings (up to 12 m height) and placed on the rooftop of the Racom company building (12 m height) mounted on a mast of 5 m height. The receiver was mounted on a mast of 19 m height in a pure rural area. The transmitter and the receiver positions for all
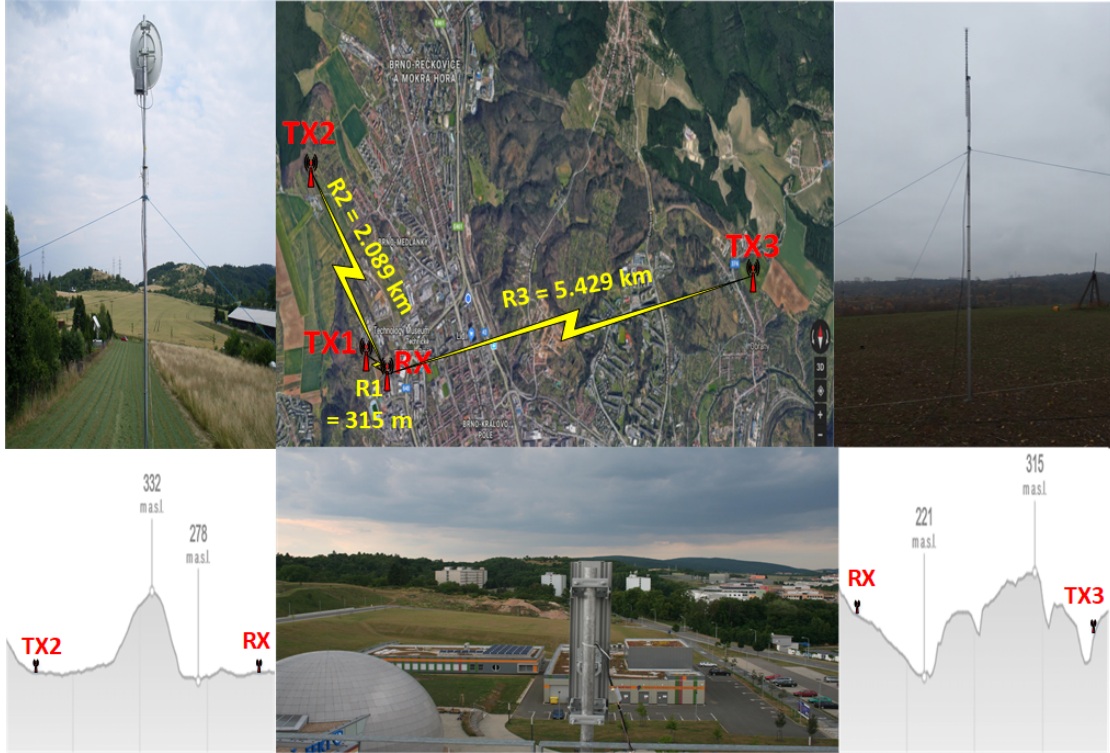
Fig. 5.19: LOS route R1 = 315 m and NLOS route R2 = 2.089 km with SHF band TX2 position on the left-hand side and R3= 5.429 km with UHF band TX3 position on the right-hand side and the position of the sector RX antenna used for SHF signal of TX2-RX measurements. Source: author.

above described routes are depicted in Fig .5.19 and Fig .5.20. Visualizations of the transmitting antennas in the case of R2 and R3 and receiving antenna with their surrounding environments are presented on the left-hand side, the right-hand side, and the center of Fig. 5.19, respectively. The mast of the received antenna of the fourth route (R4) is captured on the right-hand side of Fig. 5.20.

In order to investigate LOS and NLOS radio channel characteristics, two different channel sounder systems for 1.3 GHz and 5.8 GHz have been implemented. These sounders, together with MATLAB and LabVIEW programs, were used for channel evaluation up to 120 MHz and 600 MHz bandwidths for both 1.3 and 5.8 GHz, respectively. The basis of the transmitting station is a programmable RF generator (R&S SMU200A vector signal generator) which can be controlled by MATLAB. The generated signal was filtered using a band pass filter, amplified by a power amplifier, and directed to the directional antenna transmitter using a circular connector. The amplifier module for UHF band (MD220L-1296-48V) was modified to be used as a linear amplifier class A. However, the SHF band transmitter uses Hittite HMC408LP3 and DG0VE PA6-1-8W amplifying modules. The generated UHF
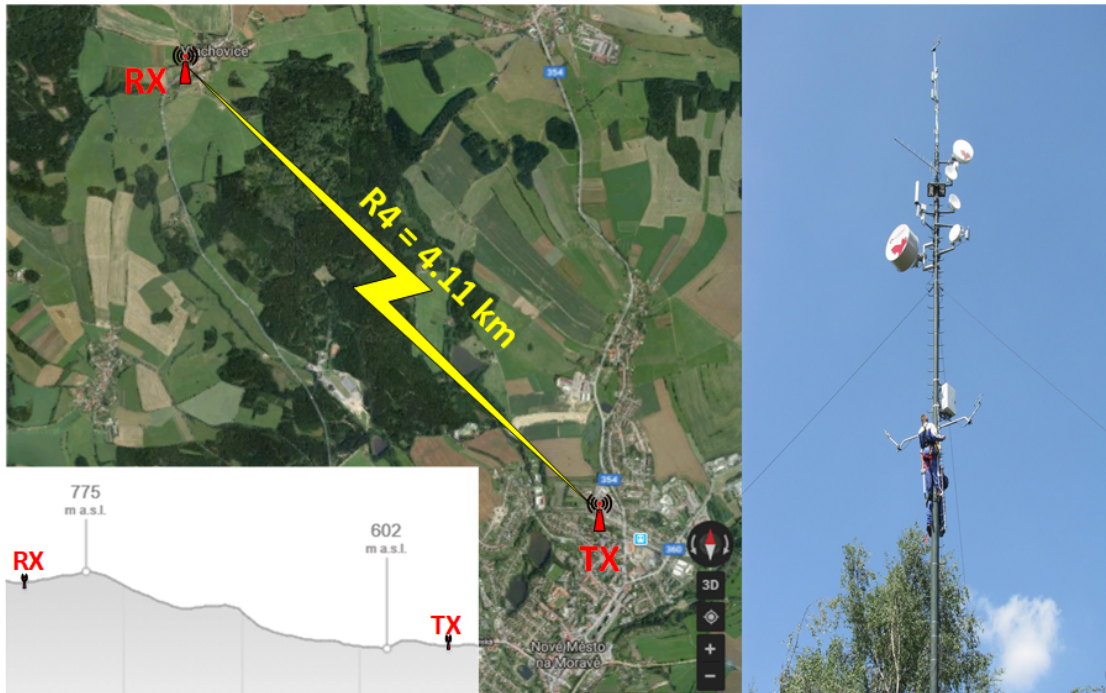
Fig. 5.20: NLOS R4 = 4.11 km route and the position of the RX antenna in the middle of the mast. Source: author.
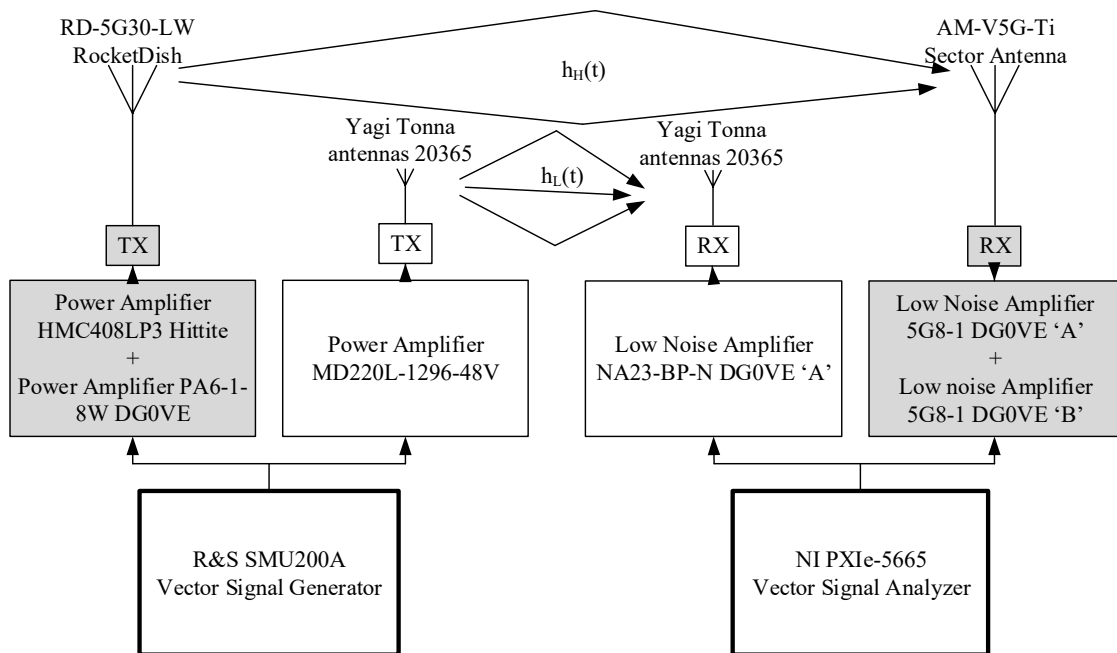
Fig. 5.21: Channel sounding systems diagram with transmitter and receiver for both UHF (white colored) and SHF (grey colored) bands.

(1.3 GHz) signal was transmitted using 35 elements Yagi Tonna antennas 20365 with 20 dBi of gain. The SHF (5.8 GHz) signal was transmitted by parabolic RD-5G30-
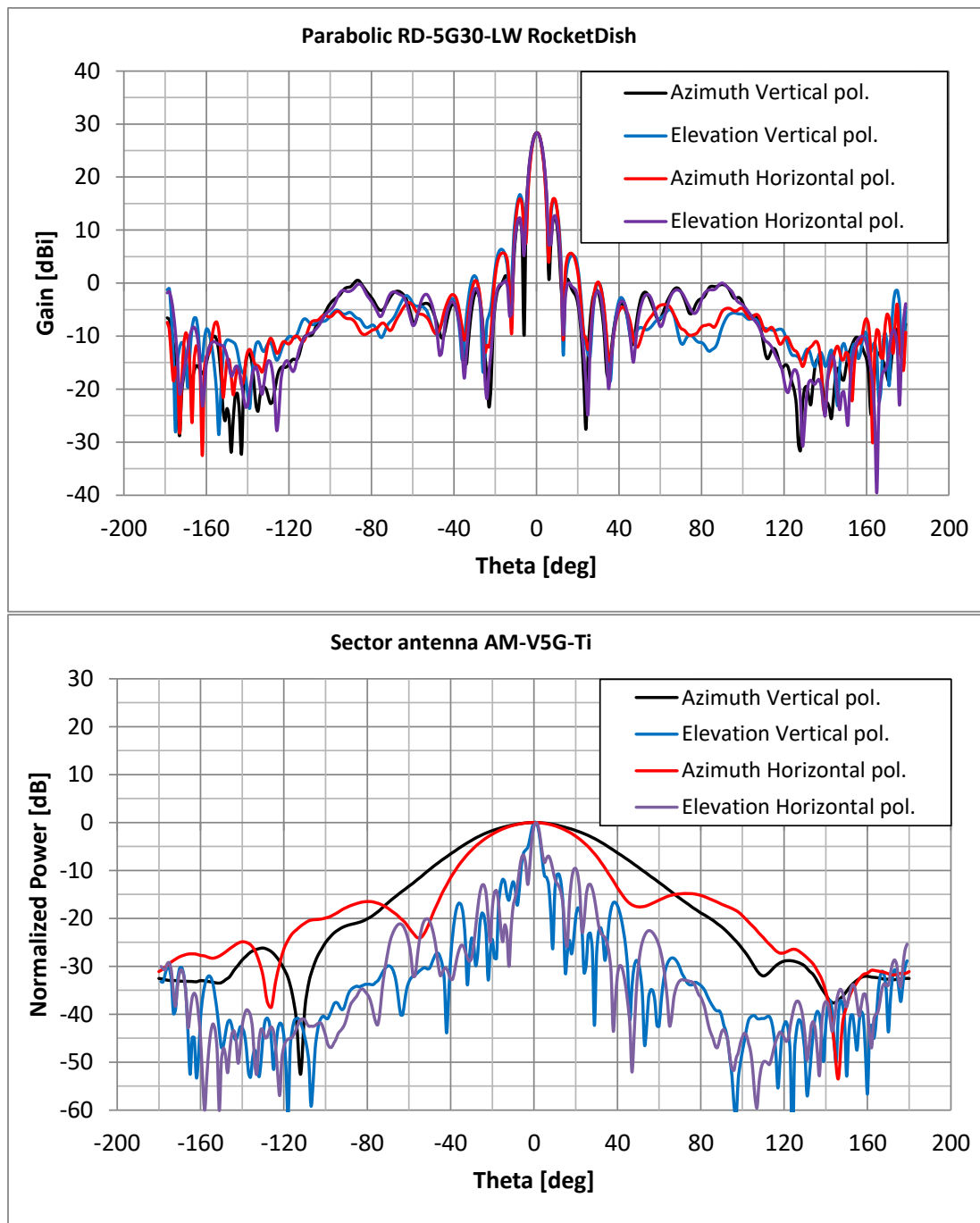
Fig. 5.22: Parabolic and sector antennas rectangular radiation (E and H planes) in the case of vertical and horizontal co-polarizations Source: author.

LW RocketDish with gain equaling 30 dBi. The receiver consists of a directional antenna, low noise amplifier, band pass filter, and signal analyzer. National Instruments PXIe-5665 is used for both UHF and SHF bands. It consists of three basic modules: PXIe-5653 RF synthesizer, PXIe-5605 downconverter, and PXIe-5622

150 MS/s 16-bit digitizer. The UHF and SHF signals were received by 35 elements Yagi Tonna antennas 20365 (20 dBi gain) and sector antenna AM-V5G-Ti (21 dBi gain), respectively. The developed software in LabVIEW environment for National Instruments PXIe-5665 was used for recording and processing the raw data received by the channel sounder. This software is able to record up to 600 MHz of bandwidth via stepped re-tuning by 50 MHz blocks with the ability to be synchronized with the transmitted signal. In order to save the achieved data with 50 MHz instance bandwidth and 16-bits precision, a Redundant Array of Inexpensive Disks (RAID) with a capacity of 12 TB was used. MATLAB was also used for final data processing. The sounding signal is a linear FM chirp returning with a speed of 40 MHz/1ms. Fig. 5.21 depicts the schematics of the sounder for UHF (white blocks) and SHF (grey blocks) bands with a shared vector signal generator and analyzer. More information about our parabolic and sector antenna characteristics, and E and H planes for vertical and horizontal co-polarizations are captured in Fig. 5.22.

As a result of all above mentioned setting, Fig. 5.23 presents the cumulative probability of the path loss for LOS environment. The cumulative probability of path loss values fit well with the Normal distribution with μ mean and σ standard deviation parameters. The path loss values of the R1 LOS route are in the range of $87.6 - 88.5$ dB with a mean value 88.1 dB and standard deviation 0.22 dB for 1.3 GHz with horizontal co-polarization, $88.2 - 89.9$ dB with a mean value 89.04 dB and standard deviation 0.33 dB for 1.3 GHz with vertical co-polarization, $114.9 - 116.1$ dB with a mean value 115.49 dB and standard deviation 0.23 dB for 5.8 GHz horizontal co-polarization, and $116.5 - 117.9$ dB with a mean value 117.1 dB and standard deviation 0.24 dB for 5.8 GHz with vertical co-polarization. The distribution shape is also depicted in Fig. 5.23 and presented in black, blue, magenta, and cyan colors for UHF horizontal co-polarization, UHF vertical co-polarization, SHF horizontal co-polarization, SHF vertical co-polarization, respectively. The shape can provide useful information about the density of the measured path loss. It can be observed that in the case of both 1.3 and 5.8 GHz, the path loss for vertical co-polarization exceeds the path loss of the horizontal one. It is also clear that path loss increases with frequency.

Figure 5.24 presents the measured path loss for 1.3 GHz sounding system in the case of horizontal and vertical co-polarizations. Black circles represent the measured path loss values for horizontally transmitted and received signals, whereas blue circles represent the measured path loss values for vertically transmitted and received signals. The best line fit have been produced using a MATLAB function with path loss exponents equaling 3.9 and 3.7 for horizontal and vertical polarization cases, respectively. These results are comparable with the results specified in [146], where the path loss exponent value for distances up to 1.4 km varies between 2.9 and 3.1
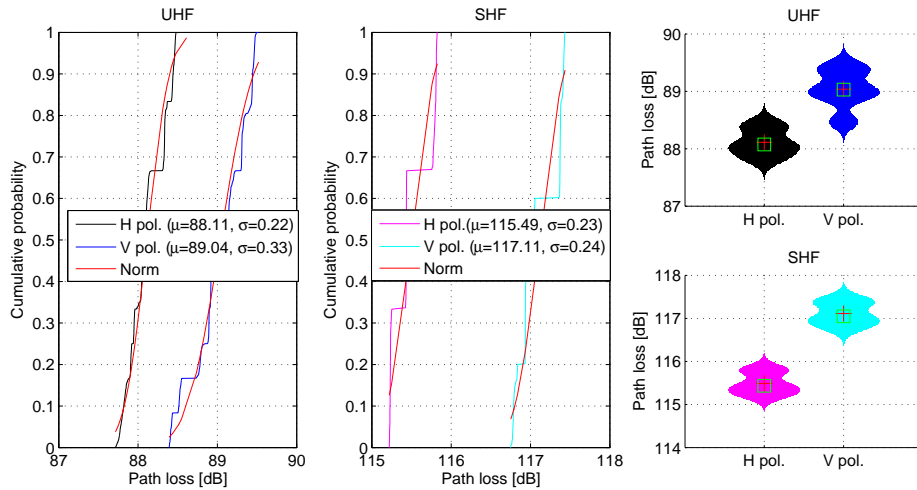
Fig. 5.23: CDF of the measured path loss of both 1.3 and 5.8 GHz transmitted signals in LOS environment with horizontal and vertical co-polarization antenna settings. The curve colored in red represents the Normal distribution. Source: author.
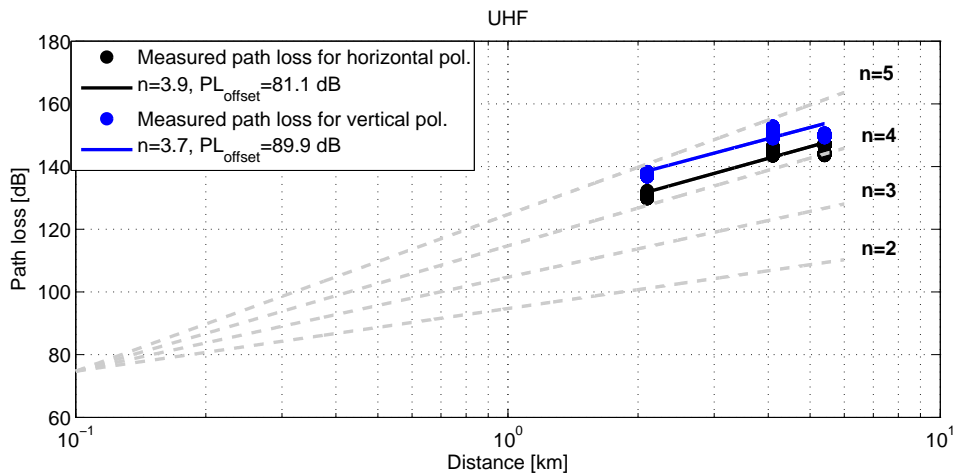
Fig. 5.24: The measured path loss for 1.3 GHz center frequency of the outdoor NLOS environment. The black and blue circles represent the measured NLOS path loss values for horizontal and vertical co-polarization, respectively. Source: author.

for 2 GHz frequency. The path loss exponent value was also captured in urban environment [153] for 800 MHz frequency and reached a value of n = 3.3.

Figure 5.25 depicts the measured path loss for the 5.8 GHz sounding system in the case of horizontal and vertical co-polarizations, represented by black and blue circles, respectively. The best line fit have been produced using a MATLAB function with path loss exponents n equaling 4.6 and 4.1 for horizontal and vertical polarization cases, respectively. These values can be compared with values achieved
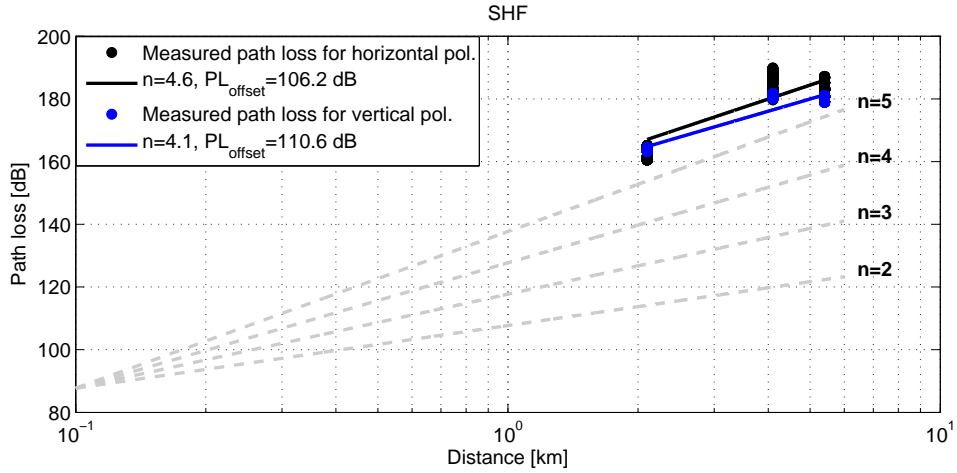
Fig. 5.25: The measured path loss for 5.8 GHz center frequency of the outdoor NLOS environment. The black and blue circles represent the measured NLOS path loss values for horizontal and vertical co-polarizations, respectively. Source: author.

in [149], for frequencies $3 - 6$ GHz where the path loss exponents between 3.92 and 4.7 were achieved. The dashed grey lines represent the theoretical path loss model in the case of different exponents.

Figures 5.26 and 5.27 display the cumulative probability of the RMS delay spread for LOS environment presented as the R1 route and 2.089, 5.429, and 4.11 km NLOS environments presented as R2, R3, and R4 routes, respectively. The RMS delay spread values for all routes and frequencies fit well with the Normal distribution with μ mean and σ standard deviation parameters. It can be distinguished, that the R1 LOS route offers smaller RMS delay spread compared with all plotted RMS values for NLOS environments in both 1.3 and 5.8 GHz. This behavior is expected. On one hand it can be due to a very strong LOS component compared with the reflected or scattered path, leading to lower RMS delay spread. On the other hand, in the case of NLOS environment, the transmitted signal is blocked or severely attenuated causing multipath to arrive at the receiver over a large propagation time interval. Similar characteristics are observed in [149, 157]. The wideband RMS delay spread for the R1 route is in the range of $15.11 - 18.42$ ns for 1.3 GHz with horizontal co-polarization, $23.18 - 32.58$ ns for 1.3 GHz with vertical co-polarization, $11.53 - 12.21$ ns for 5.8 GHz horizontal co-polarization, and $15.82 - 16.62$ ns for 5.8 GHz with vertical co-polarization. It can be seen from Figure 5.26 that in the case of the first route R1 LOS, the higher frequency provides smaller mean RMS delay spread in both horizontal and vertical polarization settings. This behavior was also mentioned in [149, 158]. It is also clear that in the case of both UHF and SHF frequencies, the vertical co-polarization shows higher mean RMS delay than
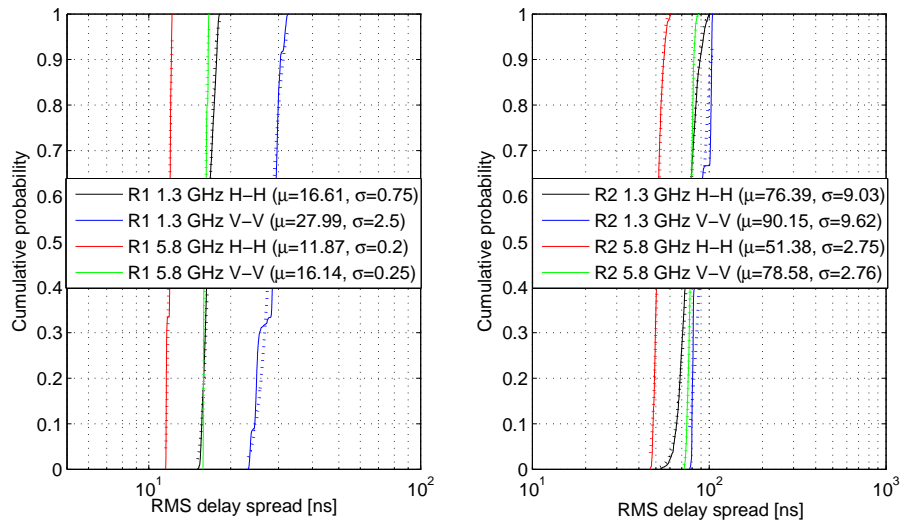
Fig. 5.26: CDF of the RMS delay spread in [ns] for different frequencies and both horizontal and vertical co-polarizations of the first and second measurement routes (R1 and R2) in LOS and NLOS scenarios, respectively. The colored dotted lines represent the Normal distribution of the corresponding frequency and polarization combinations. Source: author.
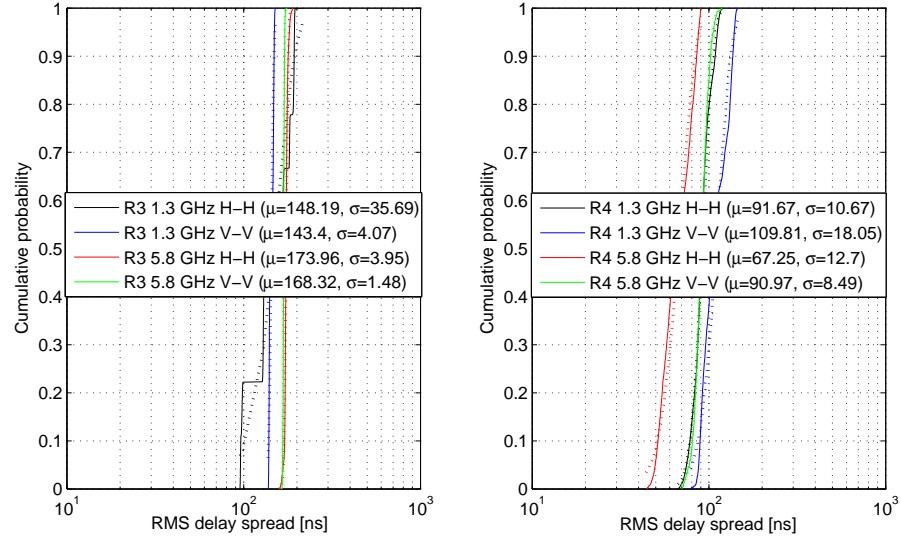
Fig. 5.27: CDF of RMS delay spread in [ns] for different frequencies and both horizontal and vertical co-polarizations captured for the third and fourth measurement routes (R3 and R4). The colored dotted lines represent the Normal distribution of the corresponding frequency and polarization combinations. Source: author.

Tab. 5.2: The mean, standard deviation, minimum, and maximum values of RMS delay spread for different frequencies and co-polarizations in both LOS and NLOS environments

RMS Delay							
Route	**Env.**	**Freq.**	**Pol.**	μ **[ns]**	σ **[ns]**	**Min [ns]**	**Max [ns]**
R1	LOS	1.3 GHz	H-H	16.61	0.75	15.11	18.42
			V-V	27.99	2.50	23.18	32.58
		5.8 GHz	H-H	11.87	0.20	11.53	12.21
			V-V	16.14	0.25	15.82	16.62
R2	NLOS	1.3 GHz	H-H	76.39	9.03	52.99	99.70
			V-V	90.15	9.62	77.44	104.82
		5.8 GHz	H-H	51.38	2.75	46.43	60.67
			V-V	78.58	2.76	72.15	87.63
R3		1.3 GHz	H-H	148.19	35.69	95.21	215.39
			V-V	143.40	4.07	137.24	151.27
		5.8 GHz	H-H	173.96	3.95	157.70	189.54
			V-V	168.32	1.48	163.33	176.58
R4		1.3 GHz	H-H	91.67	10.67	66.85	119.73
			V-V	109.81	18.05	78.73	147.76
		5.8 GHz	H-H	67.25	12.70	44.12	89.91
			V-V	90.97	8.49	70.44	119.11

horizontal co-polarization. For the R2 route, the RMS delay spread is in the range of $52.99 - 99.70$ ns for 1.3 GHz with horizontal co-polarization, $77.44 - 104.82$ ns for 1.3 GHz with vertical co-polarization, $46.43 - 60.67$ ns for 5.8 GHz horizontal co-polarization, and $72.15 - 87.63$ ns for 5.8 GHz with vertical co-polarization. In the case of the R3 route, the RMS delay spread is in the range of $95.21 - 215.39$ ns for 1.3 GHz with horizontal co-polarization, $137.24 - 151.27$ ns for 1.3 GHz with vertical co-polarization, $157.70 - 189.54$ ns for 5.8 GHz horizontal co-polarization, and $163.33 - 176.58$ ns for 5.8 GHz with vertical co-polarization. For the R4 route, it is in the range of $66.85 - 119.73$ ns for 1.3 GHz with horizontal co-polarization, $78.73 - 147.76$ ns for 1.3 GHz with vertical co-polarization, $44.12 - 89.91$ ns for
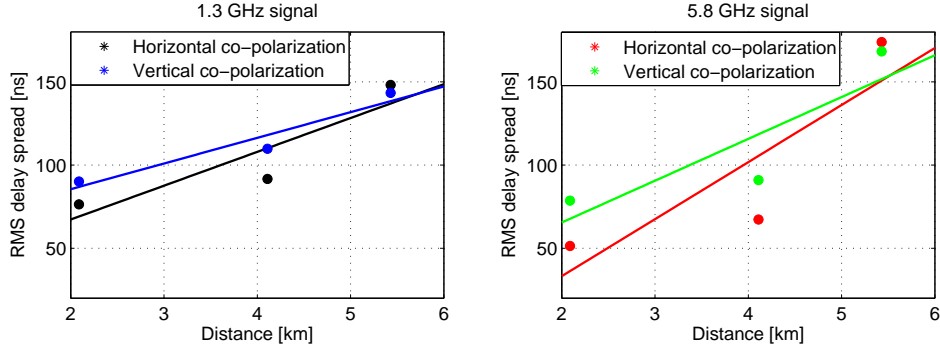
Fig. 5.28: The mean values of RMS delay spread as a function of TX-RX distance for different frequencies and co-polarizations in NLOS environment. Source: author.

5.8 GHz horizontal co-polarization, and $70.44 - 119.11$ ns for 5.8 GHz with vertical co-polarization. It can be observed that the horizontal co-polarization shows smaller mean RMS delay spread than the vertical co-polarization for 1.3 and 5.8 GHz. However, the third route, R3, shows different characteristics. This can be due to the building with a metal roof between the transmitter and the receiver, that causes depolarization. Table 5.2 combines all needed information about the RMS delay spread values. The effect of TX-RX distance on the mean values of RMS delay spread is also investigated. The mean RMS delay spread values increase with increasing the distance between the transmitter and the received. A similar trend is observed in [159]. The relation between the mean RMS delay spread and the distance can be fitted with linear mode $\sigma_{\tau UHF,H} = 20d + 27$ for UHF with horizontal co-polarization, $\sigma_{\tau UHF,V} = 15d + 55$ for UHF with vertical co-polarization, $\sigma_{\tau SHF,H} = 34d - 33$ for SHF with horizontal co-polarization, $\sigma_{\tau SHF,V} = 25d + 15$ for SHF with vertical co-polarization, where d is the distance between the transmitter and the receiver in [km]. From these functions, it can be noticed that the line slope of the RMS delay spread of SHF frequencies is greater than the line slope of RMS delay spread of UHF frequencies. Therefore, the mean RMS delay spread for SHF frequencies more extremely increases compared with the mean RMS delay spread of UHF frequencies. The same characteristics were captured in the case of comparing horizontal and vertical co-polarization where the horizontally polarized signal is more sensitive to distance changes. All above mentioned properties are depicted in Fig. 5.28.

Figure 5.29 depicts the RMS delay spread dependency of the coherence bandwidth in 1.3 GHz NLOS environments where the coherence bandwidth in MHz and the RMS delay spread in ns. This relation is fitted with the exponential model $B_c = 18.34 \cdot e^{-0.002\sigma_\tau}$.

Figure 5.30 depicts RMS delay spread dependency of the coherence bandwidth in 5.8 GHz NLOS environments where the coherence bandwidth in MHz and the
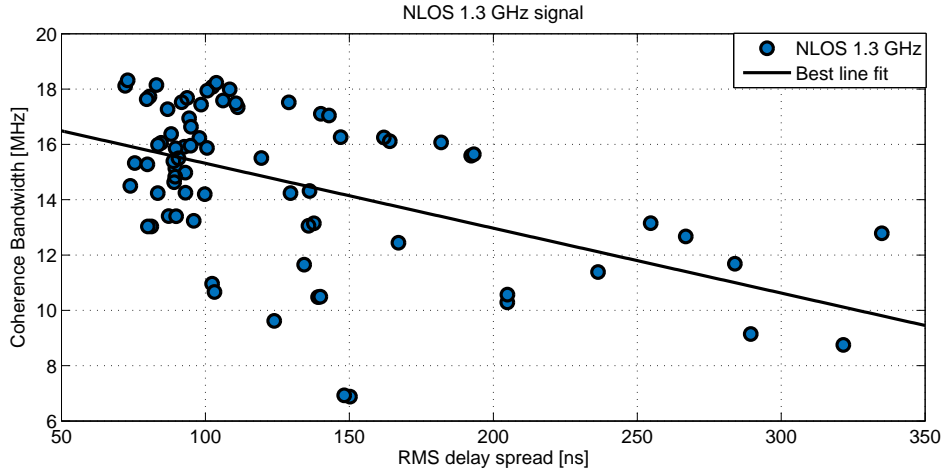
Fig. 5.29: Scatter plot of the coherence bandwidth B_c against the RMS delay spread in the case of transmitted signal with 1.3 GHz center frequency in NLOS environments. Source: author.
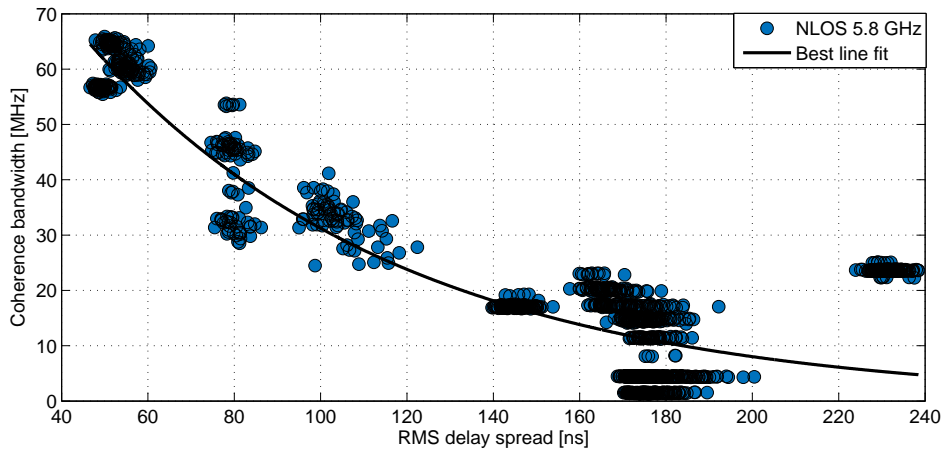
Fig. 5.30: Scatter plot of the coherence bandwidth B_c against the RMS delay spread in the case of a transmitted signal with 5.8 GHz center frequency in NLOS environments. Source: author.

RMS delay spread in ns. The measurement represented as blue circles which are achieved from the R2, R3, R4 route measurements fit with the exponential model $B_c = 121.5 \cdot e^{-0.014\sigma_\tau}$. A similar relation was observed in [160, 161].

Figure 5.31 depicts the cumulative probability of the measured wideband CFR variation for different routes (R1, R2, R3, R4) of 1.3 GHz center frequency and horizontal and vertical co-polarizations. It can be observed that the CFR variation values fit well with the Normal distribution which is plotted as a dotted curve colored according to a particular route. The CFR variations have mean values of 0.044, 0.25,
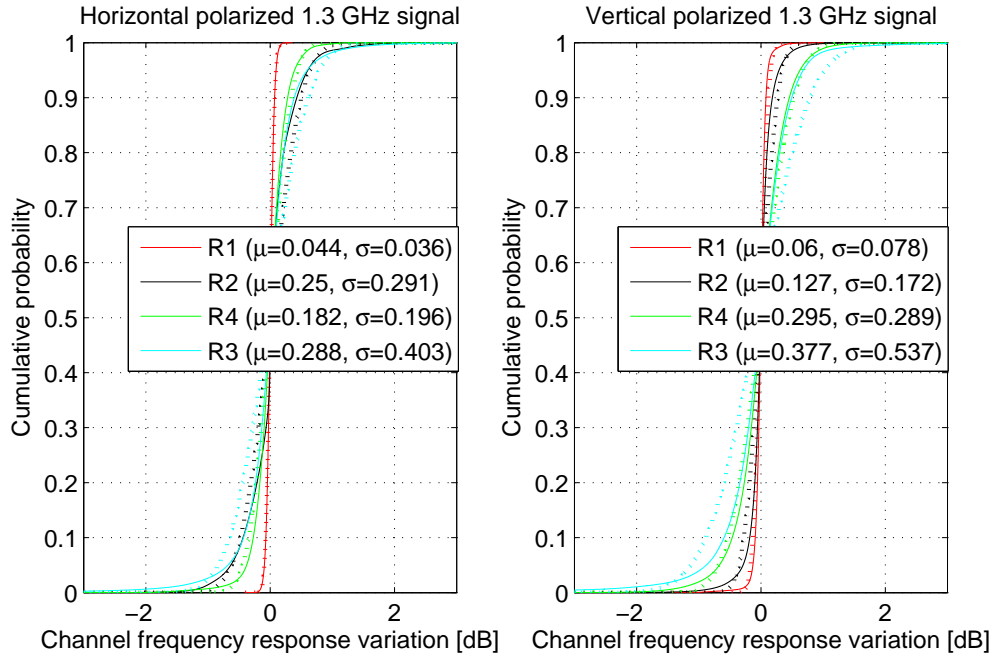
Fig. 5.31: CDF of CFR variation of 1.3 GHz center frequency for both horizontal and vertical co-polarizations. The curve colored in red, black, blue, and green represent the calculated CFR variation for the first to the fourth routes, respectively. The colored dotted lines represent the Normal distribution of the corresponded measured CFR variation values. Source: author.

0.288, 0.182 dB and standard deviation of 0.036, 0.291, 0.403, 0.196 dB in the case of horizontal co-polarization, whereas mean values of 0.06, 0.127, 0.377, 0.295 dB and standard deviation of 0.078, 0.172, 0.537, 0.289 dB in the case of vertical co-polarization. It can be noticed that the CFR variations have the smallest mean and standard deviation values in the case of the R1 route which corresponds to the LOS scenario.

Figure 5.32 presents the cumulative probability of the measured wideband CFR variation for different routes (R1, R2, R3, R4) of 5.8 GHz center frequency and horizontal and vertical co-polarizations. It can be seen that the CFR variation values also fit well with the Normal distribution which is plotted as a dotted curve colored according to a particular route. The CFR variations have mean values of 0.041, 3.083, 1.246, 2.296 dB and standard deviation of 0.119, 2.902, 1.686, 2.3 dB in the case of horizontal co-polarization, whereas mean values of 0.044, 3.48, 1.621, 1.491 dB and standard deviation of 0.119, 2.952, 1.621, 1.478 dB in the case of vertical co-polarization. The same feature of lowest mean and standard deviation values appears for the first route, R1, which represents the LOS scenario.

It is also clear from Fig. 5.31 and Fig. 5.32 that the CFR variations increase
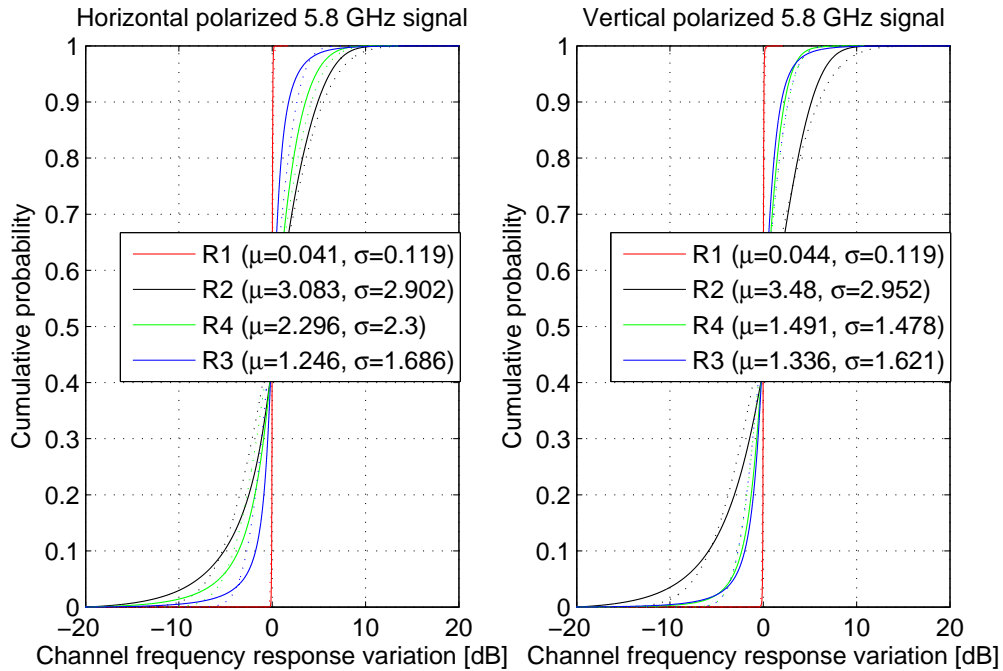
Fig. 5.32: CDF of CFR variation of 5.8 GHz center frequency for both horizontal and vertical co-polarization. The curve colored in red, black, blue, and green represent the calculated CFR variation for the first to the fourth routes, respectively. The colored dotted lines represent the Normal distribution of the corresponding measured CFR variation values. Source: author.

with frequency. This merit becomes more visible in the case of the NLOS scenario. The second route, R2, shows the highest CFR variation that can be due to the fact that higher frequency signals tend to scatter more than the lower ones. These scatter objects can be moving people and cars.

5.6 Conclusion

In this chapter, a rapid wireless channel sounding system for D2D communication is designed and implemented. In the case of indoor measurements, the Zadoff-Chu sequence with 2 MHz bandwidth is used as the transmitted signal. The auto-correlation of the Zadoff-Chu sequence is not considered in this research. Emphasis is placed on the constant amplitude property of this sequence in the frequency domain. According to this property, the Zadoff-Chu sequence is capable of scanning a specific bandwidth at each transmission. The bandwidth depends on several factors; sequence length is one of them. A MATLAB-based simulator of Zadoff-Chu channel sounding in fading channel conditions has been created. In order to prove

the trustworthiness of the frequency domain Zadoff-Chu sounding technique, it has been tested in real channel conditions using USRP devices. A frequency domain channel sounding method is employed to characterize this channel with 100 MHz wide bandwidth. The results of the frequency domain channel sounding are compared with the results of our proposed sounding method. It has been observed that both methods gave us the same channel response. The frequency domain Zadoff-Chu technique is tested in indoor LOS channel with different distances between the transmitter and the receiver. Channel characteristics as RMS delay spread, coherence bandwidth, average mean excess delay and path loss are calculated. Channel exponential $n = 1.67$ is measured. As a conclusion, the proposed method provides us with the same results of channel characteristics as the frequency domain channel sounder but with 20 times faster performance. That makes the sounder useful for time-varying channels. The speed of wide channel measurement also depends on the sequence length and the measurement resolution. Its main disadvantage is the long post-processing procedure that must be carried out to obtain the channel impulse response.

In the case of outdoor measurements, the D2D outdoor long-range communication channel was utilized for the measurement campaign. Both UHF and SHF bands were sounded using Yagi Tonna antennas as a transmitter and a receiver at 1.3 GHz and parabolic RD-5G30-LW RocketDish antenna transmitter and AM-V5G-Ti sector antenna receiver at 5.8 GHz. The vertical and the horizontal co-polarizations were presented in both LOS and NLOS scenarios. As output, channel characteristics as RMS delay spread, path loss, coherence bandwidth, and CFR variation were extracted. In the case of microcell LOS environment (with 315 m distance), the mean path loss value for vertical co-polarization exceed the mean path loss value of the horizontal one by 0.93 dB and 1.62 dB in the case of UHF and SHF bands, respectively. It was observed that path loss increases with frequency about 27 and 28 dB in the case of horizontal and vertical co-polarizations, respectively. Moreover, higher frequency provides smaller mean RMS delay spread in both horizontal and vertical polarization settings. It was also mentioned that vertical co-polarization shows higher mean RMS delay than horizontal co-polarization. Finally, the CFR variations were negligible in the case of UHF and SHF channel sounding with horizontal and vertical polarization cases. In the case of macrocell NLOS environments (with 2.089, 4.11, and 5.429 km distances), path loss exponents are ($n = 3.9$ for horizontal and $n = 3.7$ for vertical polarizations) and ($n = 4.6$ for horizontal and $n = 4.1$ for vertical polarizations) for UHF and SHF bands, respectively. All NLOS routes offer larger RMS delay spread compared with the LOS scenario. The vertically polarized signal shows higher mean RMS delay than the horizontally polarized one in the case of UHF and SHF bands for R1, R2, R4 routes. However, an inverse

relation was observed in the case of R3 which is explained by depolarization effects caused by the metal roof of the building between the transmitter and the receiver. It was also noticed that the mean RMS delay spread values increase with increasing the distance between the transmitter and the received for all above tested combinations. Furthermore, the relation between the coherence bandwidth and the RMS delay spread was investigated. The relation is described by the exponential equation $B_c = k \cdot e^{-a\sigma_\tau}$, where the coherence bandwidth is in MHz and the RMS delay spread in ns. The CFR variations were also studied. It was observed that the variation increases with frequency and becomes more critical in the case of NLOS scenarios.

6 CONCLUSION

This dissertation is focused on improving D2D communication underlay LTE Advanced networks. The LTE Advanced or 3GPP LTE Release 10 standard consists of various developed radio access technologies supporting advanced services that include carrier aggregation, up to eight layers downlink spatial multiplexing, and up to four layers uplink spatial multiplexing and so on. D2D communication is a promising method that gives different devices the ability to create a direct wireless link between each other. Therefore, it reduces transmission delay and increases network capacity. There are several types of D2D communications, however, in this research, only D2D communication underlay LTE Advanced cellular network was considered. This method is more spectrum utilizing, but less interference resistant. Therefore, the compatibility of both technologies was investigated. The achieved outcomes of this research with respect to the targets can be presented as follow:

Target 1: Evaluate the uplink physical layer of LTE Advanced systems.

Outcome: The structure of previously described LTE Advanced systems which includes a transmitter, receiver, and radio channel were implemented in MATLAB. Two codewords of an LTE Advanced signal with normal cyclic prefix and 1.4 MHz bandwidth was generated and transmitted over different ITU-R channels (Flat Rayleigh, Ped A, Veh A). Several modulation schemes were applied like 4QAM, 16QAM, and 64QAM. In the receiver, the transmitted signal is recovered by applying different combinations of Channel estimation and signal detection techniques. That includes (LS,ZF), (LS, SSD), (ALMMSE, ZF), and (ALMMSE, SSD). Finally, the achieved results of performance evaluation in terms of BER and throughput were depicted. It can be observed that using the combination of ALMMSE channel estimation and the SSD signal detection technique provides the system with the best performance. Depending on the combination of channel estimation and signal detection, the SNR threshold value can also be determined. This threshold specifies the usefulness of implementing MIMO technology in the uplink layer of LTE Advanced systems.

Target 2: Interference management for D2D communication user underlay LTE Advanced networks.

Outcome: Frequency Reuse (FFR) with the three power level method was proposed. It works with multiple power levels and utilizes the whole assigned bandwidth in each cell. Each cell is divided into three regions (interior, medium, and outer). The normalized capacity densities of the cells and their regions were calculated. For more realistic cases, three different cases of user distribution inside the cells were considered. Two of them are non-uniform user distributions which are compared with the performance of the default uniform distribution. The correlation between

both region and the overall capacity and the radius of each region were presented. The achieved results of the proposed scheme outperform the results of traditional Reuse-3 for specific radiuses of each region. More information was presented in Chapter 3.

Another method of interference mitigation for D2D communication was also analyzed. The usefulness of the cooperative spectrum sensing methods were declared. Therefore, a MATLAB-based simulator in fading channel conditions was created and presented. Two types of spectrum sensing detectors (Energy Detection and Kolmogorov-Smirnov tests) were evaluated. Different channel conditions, simulated (Ped A, Ped B, Veh A, Veh B) and real ones (indoor-indoor, indoor-outdoor, outdoor-indoor and outdoor-outdoor) were tested. The results depict the advantage of using cooperate spectrum sensing methods with AND, OR, and MAJORITY rules. All achieved results were discussed in Chapter 4.

Target 3: Improve D2D communication performance underlay LTE Advanced networks.

Outcome: In order to achieve high capacity and throughput in any communication system, a good knowledge of channel characteristics should be available. This knowledge enables system designers to ensure that inter symbol interference (ISI) does not dominate and hence lead to an excessive irreducible bit error rate. Therefore, a new method of channel estimation was proposed. It can be used for static as well as vehicular communication. Frequency domain Zadoff-Chu sounding technique can be used for both indoor and outdoor channel measurements. The autocorrelation of the Zadoff-Chu sequence was not considered in this research. Emphasis was placed on the constant amplitude property of this sequence in the frequency domain. According to this property, the Zadoff-Chu sequence is capable of scanning a specific bandwidth at each transmission. The bandwidth depends on several factors; sequence length is one of them. In order to verify the proposed sounder, a MATLAB based system has been created. Universal Software Radio Peripheral (USRP) devices were used to test the system in real channel conditions. Channel impulse response of three different environments (cable, LOS, and NLOS) were extracted using both a basic frequency domain channel sounder and the proposed method. It has been observed that both methods gave us the same channel response. However, the proposed method showed 20 times faster performance. The frequency domain Zadoff-Chu technique was tested in indoor LOS channel with different distances between the transmitter and the receiver. The channel characteristics as RMS delay spread, the coherence bandwidth, the average mean excess delay and the path loss were calculated. The channel exponential n = 1.67 was measured. A D2D outdoor long-range communication channel measurement campaign was also conducted. It investigates the channel characteristics of D2D communi-

cation scenarios underlaying 5G networks in both ultra-high frequency (UHF) and super high frequency (SHF) bands with co-polarized horizontal and vertical antenna configurations. As an output, the channel characteristics as RMS delay spread, path loss, coherence bandwidth, and channel frequency response variation were extracted. It was observed that path loss increases with frequency about 27 and 28 dB in the case of horizontal and vertical co-polarizations, respectively. However, mean RMS delay spread increases with decreasing the frequency and increasing the distance between the transmitter and receiver. The relation between the coherence bandwidth and the RMS delay spread was captured and depicted by the exponential equation $B_c = k \cdot e^{-a\sigma_\tau}$. The channel frequency response (CFR) variations increase with frequency and become more critical in the case of NLOS scenarios.

AUTHOR'S PUBLICATIONS

[1] Kasem, E., & Prokopec, J. (2012). The evolution of LTE to LTE-Advanced and the corresponding changes in the uplink reference signals. *Elektrore-vueEng*, ISSN: 1213–1539.

[2] Kasem, E., & Prokopec, J. (2013) Evolution of physical uplink channels in LTE-advanced. *ElektrorevueEng*, ISSN: 1213–1539.

[3] Kasem, E., Marsalek, R., & Blumenstein, J. (2013). Performance of LTE advanced uplink in a Flat rayleigh channel. *Advances in Electrical and Electronic Engineering*, vol. 11 no. 4, pp. 266–274.

[4] Kasem, E., & Marsalek, R. (2013). The Performance of LTE Advanced Uplink in Flat Rayleigh and Pedestrian Channels. *ElektrorevueEng*, vol.4, no. 3, ISSN: 1213-1539.

[5] Lekomtcev, D., Kasem, E., & Marsalek, R. (2015). Matlab-based simulator of cooperative spectrum sensing in real channel conditions. In *25th International Conference Radioelektronika (RADIOELEKTRONIKA)*, IEEE, pp. 209–212.

[6] Kasem, E., Lekomtcev, D., & Marsalek, R. (2015). Cooperative spectrum sensing in real channel conditions. In *13th International Conference on Telecommunications (ConTEL)*, IEEE, pp. 1–6.

[7] Kassem, E., Marsalek, R., & Blumenstein, J. (2016). On the capacity of fractional frequency reuse with three power levels for non-uniform user distribution. In *International Conference on Systems, Signals and Image Processing (IWSSIP)*, IEEE, pp. 1–5.

[8] Kassem, E., Marsalek, R., & Blumenstein, J. (2018). Frequency Domain Zadoff-Chu Sounding Technique for USRPs. In *25th International Conference on Telecommunications (ICT)*, IEEE.

[9] (Impact in review) Kassem, E., Blumenstein, J., Povalac, A., Vychodil, J., Pospisil, M., Marsalek, R., & Hruska, J. Wideband UHF and SHF Long-Range Static Channel Characterization. In *EURASIP Journal on Wireless Communications and Networking*.

BIBLIOGRAPHY

[1] Americas, G. (2012). 4G Mobile Broadband Evolution: 3GPP Release 10 and Beyond *HSPA+, SAE/LTE* and LTE advanced. *4G Mobile Broadband Evolution: 3GPP Release 10 and Beyond HSPA+, SAE/LTE and LTE advanced,* pp. 80–95

[2] 3GPP, 3rd generation partnership project (2013).Technical specification group radio access network; Physical Channels and Modulation. *3gpp TS 36.211 V10.7.0,* France: Organizational Partners (ARIB, ATIS, CCSA, ETSI, TTA, TTC).

[3] 3GPP, 3rd generation partnership project (2011). Requirements for Further Advancements for Evolved Universal Terrestrial Radio Access (E-UTRA) *3gpp TR 136 913 V10.0.0,* . France: European Telecommunications Standards Institute.

[4] Sawahashi, M., Kishiyama, Y., Taoka, H., Tanno, M., & Nakamura, T. (2009). Broadband radio access: LTE and LTE-advanced. In *International Symposium on Intelligent Signal Processing and Communication Systems, 2009. ISPACS 2009,* 2009, pp. 224–227.

[5] Lee, J., Han, J. K., & Zhang, J. (2009). MIMO technologies in 3GPP LTE and LTE-advanced. *EURASIP Journal on Wireless Communications and Networking,* 3.

[6] 3GPP, 3rd generation partnership project (2010). Evolved universal terrestrial radio access (E-UTRA) and evolved universal terrestrial radio access network (E-UTRAN). *3gpp TS 36.300 V8.12.0,* France: Partners (ARIB, ATIS, CCSA, ETSI, TTA, TTC).

[7] 3GPP, 3rd generation partnership project (2010). Evolved Universal Terrestrial Radio Access (E-UTRA); LTE physical layer *3gpp TS 36.201 V10.0.0,* France: Organizational Partners (ARIB, ATIS, CCSA, ETSI, TTA, TTC).

[8] Song, L., Niyato, D., Han, Z., & Hossain, E. (2015). *Wireless device-to-device communications and networks.* Cambridge University Press.

[9] Asadi, A., Wang, Q., & Mancuso, V. (2014). A survey on device-to-device communication in cellular networks. *IEEE Communications Surveys & Tutorials.* vol. 16 no. 4, pp. 1801–1819.

[10] 3GPP, 3rd generation partnership project (2009). Technical specification group radio access network; Physical Channels and Modulation. *3gpp TS 36.211*

V8.9.0, France: Organizational Partners (ARIB, ATIS, CCSA, ETSI, TTA, TTC).

[11] Kasem, E., & PROKOPEC, J. (2013). Evolution of physical uplink channels in LTE-advanced. *ElektrorevueEng e-journal,* vol. 4, no. 1, pp. 12–16, ISSN: 1213-1539

[12] Park, C. S., Wang, Y. P. E., Jongren, G., & Hammarwall, D. (2011). Evolution of uplink MIMO for LTE-advanced. *IEEE Communications Magazine,* vol. 49 no. 2.

[13] Sesia, S., Baker, M., & Toufik, I. (2011). *LTE–the UMTS long term evolution: from theory to practice .* 2nd ed, John Wiley & Sons., ISBN 978-047-0660-256.

[14] Dahlman, E., Parkvall, S., & Skold, J. (2013). *4G: LTE/LTE-advanced for mobile broadband,* Amsterdam: Academic Press, ISBN 978-0-12-385489-6.

[15] Yu, C. H., Doppler, K., Ribeiro, C. B., & Tirkkonen, O. (2011). Resource Sharing Optimization for Device-to-Device Communication Underlaying Cellular Networks. In *IEEE Transactions on Wireless communications,* vol. 10, no. 8, pp. 2752–2763.

[16] Doppler, K., Rinne, M., Wijting, C., Ribeiro, C. B., & Hugl, K. (2009). Device-to-device communication as an underlay to LTE-advanced networks. *IEEE Communications Magazine, .* vol. 47, no. 12.

[17] Chae, H. S., Gu, J., Choi, B. G., & Chung, M. Y. (2011). Radio resource allocation scheme for device-to-device communication in cellular networks using fractional frequency reuse. In *17th Asia-Pacific Conference on Communications (APCC),* pp. 58–62.

[18] Wang, B., Chen, L., Chen, X., Zhang, X., & Yang, D. (2011). Resource allocation optimization for device-to-device communication underlaying cellular networks. In *73rd Vehicular Technology Conference (VTC Spring),* pp. 1–6.

[19] Liu, Z., Peng, T., Xiang, S., & Wang, W. (2012). Mode selection for device-to-device (D2D) communication under LTE-advanced networks. In *IEEE International Conference on Communications (ICC),* pp. 5563–5567.

[20] Lin, X., Andrews, J. G., & Ghosh, A. (2014). Spectrum sharing for device-to-device communication in cellular networks. *IEEE Transactions on Wireless Communications,* vol. 13 no. 12, pp. 6727–6740.

[21] Yu, C. H., Tirkkonen, O., Doppler, K., & Ribeiro, C. (2009). On the performance of device-to-device underlay communication with simple power control. In *69th Vehicular Technology Conference, VTC Spring 2009,* pp. 1–5.

[22] Huang, Y., Nasir, A. A., Durrani, S., & Zhou, X. (2016). Mode selection, resource allocation, and power control for D2D-enabled two-tier cellular network. *IEEE Transactions on Communications,* vol. 64 no. 8, pp. 3534–3547.

[23] Lee, N., Lin, X., Andrews, J. G., & Heath, R. W. (2015). Power control for D2D underlain cellular networks: Modeling, algorithms, and analysis. *IEEE Journal on Selected Areas in Communications,* vol. 33 no. 1, 1–13.

[24] Zhao, W., & Wang, S. (2015). Resource allocation for device-to-device communication underlying cellular networks: An alternating optimization method. *IEEE Communications Letters,* vol. 19 no.8, pp. 1398–1401.

[25] Xu, H., Yang, Z., Huang, N., Wang, J. Y., Shi, J., & Chen, M. (2016). Channel allocation and power control in D2D uplink underlain cellular networks. In *IEEE Globecom Workshops,* pp. 1–6.

[26] Janis, P., Koivunen, V., Ribeiro, C., Korhonen, J., Doppler, K., & Hugl, K. (2009). Interference-aware resource allocation for device-to-device radio underlying cellular networks. In *IEEE 69th Vehicular Technology Conference, VTC Spring,* pp. 1–65.

[27] Zulhasnine, M., Huang, C., & Srinivasan, A. (2010). Efficient resource allocation for device-to-device communication underlaying LTE network. In *6th International Conference on Wireless and Mobile Computing, Networking and Communications (WiMob),* pp. 368–375.

[28] Xu S. , Wang H., Chen T., Huang Q. & Peng T. (2010) Effective Interference Cancellation Scheme for Device-to-Device Communication Underlying Cellular Networks. *IEEE 72nd Vehicular Technology Conference* Fall, Ottawa, ON, pp. 1–65.

[29] Chen, T., Charbit, G., & Hakola, S. (2010). Time hopping for device-to-device communication in LTE cellular system. In *Wireless Communications and Networking Conference (WCNC),* (pp. 1–66).

[30] Reed, J. H. (2002). *Software radio: a modern approach to radio engineering.* Prentice Hall Professional.

[31] Ettus Research (2018). The leader in Software Defined Radio (SDR) [online]. <https://www.ettus.com/>.

[32] Analog Devices (2018). AD-FMCOMMS5EBZ User Guide. [online]. <https://wiki.analog.com/resources/eval/user-guides/ad-fmcomms5-ebz>.

[33] National Instruments (2018). FlexRIO Custom Instruments and Processing. [online]. <http://www.ni.com/product-documentation/10800/en/>.

[34] Ettus Research (2018). Spectra DTP, baseband and RF SDR Development and Test Platform. [online]. <http://www.prismtech.com/spectra/products/spectra-dtp>.

[35] Microsoft (2018). Microsoft Research Software Radio (Sora). [online]. <http://research.microsoft.com/en-us/projects/sora/>.

[36] Data Soft (2018). Thunder SDR Waveform Development and Test System. [online]. <https://www.datasoft.com/products/thunder/index.html>.

[37] Gutierrez-Agullo, J. R., Coll-Perales, B., & Gozalvez, J. (2010). An IEEE 802.11 MAC Software Defined Radio implementation for experimental wireless communications and networking research. In *Wireless Days (WD), IFIP,* pp. 1–5.

[38] Berardinelli, G., Zetterberg, P., Tonelli, O., Cattoni, A. F., Sřrensen, T. B., & Mogensen, P. (2011). An SDR architecture for OFDM transmission over USRP2 boards. In *Conference Record of the Forty Fifth Asilomar Conference on Signals, Systems and Computers (ASILOMAR),* pp. 965–969.

[39] Humphries, J. R., & Malocha, D. C. (2013). Software defined radio for passive sensor interrogation. In *European Frequency and Time Forum & International Frequency Control Symposium (EFTF/IFC), 2013 Joint,* pp. 270–273.

[40] USRP Hardware Driver and USRP Manual (2018). [online] <https://files.ettus.com/manual/page_dboards.html>.

[41] Sriram, S., Srivasta, G., Gandhiraj, R., & Soman, K. P. (2012). Plug-ins for gnu radio companion. *International Journal of Computer Applications,* vol. 52 no. 16.

[42] ITU, International Telecommunication Union (1997). *Guidelines for evaluation of radio transmission technologies for IMT-2000,* Recommendation ITU-R M.1225.

[43] Tranter, W. H., Rappaport, T. S., Kosbar, K. L., & Shanmugan, K. S. (2004). *Principles of communication systems simulation with wireless applications,* vol. 1. New Jersey: Prentice Hall.

[44] Pahlavan, K., & Levesque, A. H. (2005). *Wireless information networks,* vol. 93. John Wiley & Sons.

[45] Jain, R. (2007). Channel models A tutorial. *WiMAX Forum AATG,* pp. 1–6.

[46] Van De Beek, J. J., Edfors, O., Sandell, M., Wilson, S. K., & Borjesson, P. O. (1995). On channel estimation in OFDM systems. In *45th Vehicular Technology Conference,* vol. 2, pp. 815–819.

[47] Coleri, S., Ergen, M., Puri, A., & Bahai, A. (2002). Channel estimation techniques based on pilot arrangement in OFDM systems. *IEEE Transactions on broadcasting,* vol. 48 no. 3, 223–229.

[48] Biguesh, M., & Gershman, A. B. (2006). Training-based MIMO channel estimation: a study of estimator tradeoffs and optimal training signals *IEEE transactions on signal processing,* vol. 54 no. 3, 884–893.

[49] Barhumi, I., Leus, G., & Moonen, M. (2003). Optimal training design for MIMO OFDM systems in mobile wireless channels. *IEEE Transactions on signal processing,* vol. 51 no. 6, 1615–1624.

[50] Qiao, Y., Yu, S., Su, P., & Zhang, L. (2005). Research on an iterative algorithm of LS channel estimation in MIMO OFDM systems. *IEEE Transactions on Broadcasting,* vol. 51 no. 1, 149–153.

[51] Ancora, A., Bona, C., & Slock, D. T. (2007). Down-sampled impulse response least-squares channel estimation for LTE OFDMA. In *IEEE International Conference on Acoustics, Speech and Signal Processing, ICASSP,* vol. 3, pp. III–293.

[52] Niranjane, V. B., & Bhoyar, D. B. (2011, June). Performance analysis of different channel estimation techniques. In *International Conference on Recent Trends in Information Technology (ICRTIT),* . pp. 74–78.

[53] Kewen, L. (2010). Research of MMSE and LS channel estimation in OFDM systems. In *2nd International Conference on Information Science and Engineering (ICISE),* pp. 2308–2311.

[54] Simko, M., Wu, D., Mehlführer, C., Eilert, J., & Liu, D. (2011). Implementation aspects of channel estimation for 3GPP LTE terminals. In *11th European*

Wireless Conference 2011-Sustainable Wireless Technologies (European Wireless), . Published in Proc. 17th European Wireless Conference, Vienna, Austria, pp. 1–5.

[55] Noh, M., Lee, Y., & Park, H. (2006). Low complexity LMMSE channel estimation for OFDM. *IEE Proceedings-Communications,* vol. 153 no.5, pp. 645–650.

[56] Mehlfuhrer, C., Caban, S., & Rupp, M. (2008). An accurate and low complex channel estimator for OFDM WiMAX. In *3rd International Symposium on Communications, Control and Signal Processing, ISCCSP,* pp. 922–926.

[57] Chen, C. J., & Wang, L. C. (2007). Performance analysis of scheduling in multiuser MIMO systems with zero-forcing receivers. *IEEE Journal on Selected Areas in Communications,* vol. 25 no. 7.

[58] Klein, A., Kaleh, G. K., & Baier, P. W. (1996). Zero forcing and minimum mean-square-error equalization for multiuser detection in code-division multiple-access channels. *IEEE transactions on Vehicular Technology,* vol. 45 no. 2, pp. 276–287.

[59] Zhu, X., & Murch, R. D. (2002). Performance analysis of maximum likelihood detection in a MIMO antenna system. *IEEE Transactions on Communications,* vol. 50 no. 2, pp. 187–191.

[60] Benjebbour, A., Murata, H., & Yoshida, S. (2001). Comparison of ordered successive receivers for space-time transmission. In *IEEE VTS 54th Vehicular Technology Conference, VTC 2001 Fall,* vol. 4, pp. 2053–2057.

[61] Golden, G. D., Foschini, C. J., Valenzuela, R. A., & Wolniansky, P. W. (1999). Detection algorithm and initial laboratory results using V-BLAST space-time communication architecture. *Electronics letters,* vol. 35 no. 1, pp. 14–16.

[62] Wolniansky, P. W., Foschini, G. J., Golden, G. D., & Valenzuela, R. A. (1998). V-BLAST: An architecture for realizing very high data rates over the rich-scattering wireless channel. In *International Symposium on Signals, Systems, and Electronics, ISSSE 98,* pp. 295–300.

[63] Pammer, V., Delignon, Y., Sawaya, W., & Boulinguez, D. (2003). A low complexity suboptimal MIMO receiver: The combined ZF-MLD algorithm. In *14th IEEE Proceedings on Personal, indoor and mobile radio communications, PIMRC 2003,* vol. 3, pp. 2271–2275.

[64] Fu, W., Zhao, C., Wei, W., & Kong, Q. (2011). Improved sphere decoding algorithm in TD-LTE system. In *3rd International Conference on Communication Software and Networks (ICCSN),* pp. 514–517.

[65] Hassibi, B., & Vikalo, H. (2005). On the sphere-decoding algorithm I. Expected complexity. *IEEE transactions on signal processing,* vol. 53 no. 8, 2806–2818.

[66] Studer, C., Burg, A., & Bolcskei, H. (2008). Soft-output sphere decoding: Algorithms and VLSI implementation. *IEEE Journal on Selected Areas in Communications,* vol. 26 no. 2.

[67] Kim, J. G., & Choi, W. S. (2011). Joint ZF and partial ML detection for uplink cellular base station cooperation. In *International Conference on ICT Convergence (ICTC),* South Korea, Seoul, pp.321–326.

[68] Shariat-Yazdi, R., & Kwasniewski, T. (2008). Low complexity sphere decoding algorithms. In *In Wireless Communication Systems. 2008. ISWCS'08. IEEE International Symposium on* (pp. 438–442).

[69] Huynh, T. A., Hoang, D. C., Islam, M. R., & Kim, J. (2008). Two-level-search sphere decoding algorithm for MIMO detection. In *IEEE International Symposium on Wireless Communication Systems. 2008. ISWCS'08,* pp. 448–452.

[70] Noaman, N. M., & Al-Hemiary, E. H. (2014). Performance Evaluation of LTE-Advanced Channel Estimation Techniques in Vehicular Environments. *International Journal of Science, Engineering and Computer Technology,* vol. 4 no. 11, pp.301–307.

[71] Mehlführer, C., Ikuno, J. C., Simko, M., Schwarz, S., Wrulich, M., & Rupp, M. (2011). The Vienna LTE simulators-Enabling reproducibility in wireless communications research. *EURASIP Journal on Advances in Signal Processing,* no. 1.

[72] Khoshnevis, A., Yamada, S., Yin, Z., & Choudhury, S. (2013). *U.S. Patent No. 8,437,705.* Washington, DC: U.S. Patent and Trademark Office.

[73] Mehlführer, C., Wrulich, M., Ikuno, J. C., Simko, M., Schwarz, S., & Rupp, M. *Vienna LTE Simulators Link Level Simulator Documentation .* Institute of Telecommunications Vienna University of Technology,Vienna, Austria

[74] Blumenstein, J., Ikuno, J. C., Prokopec, J., & Rupp, M. (2011). Simulating the long term evolution uplink physical layer. In *53rd International Symposium ELMAR,* Croatia, Zadar, pp.114–144

[75] Kasem, E., Marsalek, R., & Blumenstein, J. (2013). Performance of LTE advanced uplink in a flat rayleigh channel. *Advances in Electrical and Electronic Engineering,* vol. 11 no. 4, pp. 266–274.

[76] Kasem, E., & Marsalek, R. (2013) The Performance of LTE Advanced Uplink in Flat Rayleigh and Pedestrian Channels *ElektrorevueEng,* ISSN: 1213-1539, pp. 1213–1539.

[77] Khan, F. (2009). *LTE for 4G mobile broadband: air interface technologies and performance.* Cambridge University Press.

[78] Hardouin, E., Hassan, M. S., & Saadani, A. (2013). Downlink interference cancellation in LTE: Potential and challenges. In *2013 IEEE Wireless Communications and Networking Conference (WCNC),* pp. 3597–3602.

[79] Bosisio, R., & Spagnolini, U. (2008). Interference coordination vs. interference randomization in multicell 3GPP LTE system. In *Wireless Communications and Networking Conference,* pp. 824–829.

[80] Rahman, M., & Yanikomeroglu, H. (2010). Enhancing cell-edge performance: a downlink dynamic interference avoidance scheme with inter-cell coordination. *IEEE Transactions on Wireless Communications,* vol. 9 no. 4.

[81] Xie, Z., & Walke, B. (2009). Enhanced fractional frequency reuse to increase capacity of OFDMA systems. In *3rd International Conference on New Technologies, Mobility and Security (NTMS),* pp. 1–5.

[82] Kiani, S. G., & Gesbert, D. (2008). Optimal and distributed scheduling for multicell capacity maximization. *IEEE Transactions on Wireless Communications,* vol. 7 no. 1.

[83] Zhao, Y., & Haggman, S. G. (2001). Intercarrier interference self-cancellation scheme for OFDM mobile communication systems. *IEEE Transactions on Communications,* vol. 49 no. 7, pp. 1185-1191.

[84] Seaton, K. A., & Armstrong, J. (2000). Polynomial cancellation coding and finite differences. *IEEE transactions on Information Theory,* vol. 46 no. 1, pp. 311–313.

[85] Xiong, X., & Luo, Z. (2011). SC-FDMA-IDMA: A hybrid multiple access scheme for LTE uplink. In *7th International Conference on Wireless Communications, Networking and Mobile Computing (WiCOM),* pp. 1–5.

[86] Khan, D. A., & Priyanto, B. E. (2008). Performance evaluation of frequency hopping schemes in UTRA-ITE uplink. In *2008 Annual IEEE Conference, Student Paper,* pp. 1–5.

[87] Ali, N. A., Mourad, H. A. M., ElSayed, H. M., El-Soudani, M., Amer, H. H., & Daoud, R. M. (2016). General expressions for downlink signal to interference and noise ratio in homogeneous and heterogeneous LTE-Advanced networks. *Journal of advanced research,* vol. 7 no. 6, pp. 923–929.

[88] Chiu, C. S., & Huang, C. C. (2008). Combined partial reuse and soft handover in OFDMA downlink transmission. In *Vehicular Technology Conference, VTC Spring 2008* pp. 1707–1711.

[89] Xiang, Y., Luo, J., & Hartmann, C. (2007). Inter-cell interference mitigation through flexible resource reuse in OFDMA based communication networks. In *European wireless,* pp. 1–7.

[90] Alsawah, A., & Fijalkow, I. (2008). Optimal frequency-reuse partitioning for ubiquitous coverage in cellular systems. In *16th European Signal Processing Conference,* pp. 1–5.

[91] Cho, Y. S., Kim, J., Yang, W. Y., & Kang, C. G. (2010). MIMO-OFDM wireless communications with MATLAB. *John Wiley & Sons.,* pp. 251–263.

[92] Novlan, T. D., Ganti, R. K., Ghosh, A., & Andrews, J. G. (2011). Analytical evaluation of fractional frequency reuse for OFDMA cellular networks. *IEEE Transactions on wireless communications,* vol. 10 no. 12, pp. 4294–4305

[93] Elfadil, H. E. E. O. M., Ali, M. A. I., & Abas, M. (2015). Fractional frequency reuse in LTE networks. In *2nd World Symposium on Web Applications and Networking (WSWAN),* pp. 1-6.

[94] Bilios, D., Bouras, C., Kokkinos, V., Papazois, A., & Tseliou, G. (2012). Optimization of fractional frequency reuse in long term evolution networks. In *Wireless Communications and Networking Conference (WCNC),* pp. 1853-1857.

[95] Chang, R. Y., Tao, Z., Zhang, J., & Kuo, C. C. J. (2013). Dynamic fractional frequency reuse (D-FFR) for multicell OFDMA networks using a graph framework. *Wireless Communications and Mobile Computing,* vol. 13 no. 1, pp. 12–27.

[96] Tse, D., & Viswanath, P. (2005). *Fundamentals of Wireless Communication* . Cambridge University Press, ISBN 978-0-521-84527-4.

[97] Abhayawardhana, V. S., Wassell, I. J., Crosby, D., Sellars, M. P., & Brown, M. G. (2005). Comparison of empirical propagation path loss models for fixed wireless access systems. In *61st Vehicular Technology Conference, VTC 2005-Spring,* vol. 1, pp. 73–77.

[98] Lee, D., Xu, C., Mayekar, U., & Mohile, M. (1997). Frequency reuse factor vs. pathloss exponent and sectorization. In *IEEE MTT-S Symposium on Technologies for Wireless Applications Digest,* pp. 109–112.

[99] Elalem, M., & Zhao, L. (2009). Realistic user distribution and its impact on capacity and coverage for a WCDMA mobile network. In *Sarnoff Symposium, SARNOFF'09,* pp. 1–5.

[100] Lei, Z., Goodman, D. J., & Mandayam, N. B. (1999). Location-dependent other-cell interference and its effect on the uplink capacity of a cellular CDMA system. In *IEEE 49th Vehicular Technology Conference,* vol. 3, pp. 2164–2168.

[101] Newton, M., & Thompson, J. (2006). Classification and generation of non-uniform user distributions for cellular multi-hop networks. In *IEEE International Conference on Communications, ICC'06,* Vol. 10, pp. 4549–4553.

[102] Taranetz, M., Ikuno, J. C., & Rupp, M. (2011). Capacity density optimization by fractional frequency partitioning. In *2011 Conference Record of the Forty Fifth Asilomar Conference on Signals, Systems and Computers (ASILOMAR),* pp. 1398–1402.

[103] Ali, A., & Hamouda, W. (2017). Advances on spectrum sensing for cognitive radio networks: Theory and applications. *IEEE Communications Surveys and Tutorials,* vol. 19 no. 2, pp. 1277–1304.

[104] Deng, R., Chen, J., Yuen, C., Cheng, P., & Sun, Y. (2012). Energy-efficient cooperative spectrum sensing by optimal scheduling in sensor-aided cognitive radio networks. *IEEE Transactions on Vehicular Technology,* vol. 61 no. 2, pp. 716–725.

[105] Du, H., Wei, Z., Wang, Y., & Yang, D. (2011). Hybrid cooperative spectrum sensing scheme using double-fusion in cognitive radio networks. *Journal of Computational Information Systems,* vol. 7 no. 5, pp. 1500–1507.

[106] Kyperountas, S., Correal, N., & Shi, Q. (2010). A Comparison of Fusion Rules for Cooperative Spectrum Sensing in Fading Channels. *Virginia Tech Symposium on Wireless Personal Communications,* pp. 1–6.

[107] El-Hajj, W., Safa, H., & Guizani, M. (2011). Survey of security issues in cognitive radio networks. *Journal of Internet Technology,* vol. 12 no. 2, pp. 181-198.

[108] Marsalek, R., & Povalac, K. (2012). Kolmogorov-smirnov test for spectrum sensing: From the statistical test to energy detection. In *IEEE Workshop on Signal Processing Systems (SiPS),* pp. 97–102.

[109] Prashob, R. N., Vinod, A. P., & Krishna, A. K. (2010). An adaptive threshold based energy detector for spectrum sensing in cognitive radios at low SNR. In *IEEE International Conference on Communication Systems (ICCS),* pp. 574–578.

[110] Lekomtcev, D., & Marsalek, R. (2014). Evaluation of Kolmogorov-Smirnov test for cooperative spectrum sensing in real channel conditions. In *22nd Telecommunications Forum Telfor (TELFOR),* pp. 557-560.

[111] Conover, W. J. (1999). Practical Nonparametric Statistics. *3rd Edition, John Wiley and Sons,* ISBN: 978-0471160687.

[112] Kay, S. (2006). *Intuitive Probability and Random Processes Using MATLAB.* New York, USA: Springer, ISBN 978-0387241579.

[113] Xiao, Y., & Hu, F. (Eds.). (2008). *Cognitive Radio Networks,* 2nd Ed. Taylor and Francis Group, LLC.

[114] Teguig, D., Scheers, B., & Le Nir, V. (2012, October). Data fusion schemes for cooperative spectrum sensing in cognitive radio networks. In *Military Communications and Information Systems Conference (MCC),* pp. 1–7.

[115] Lekomtcev, D., Kasem, E., & Marsalek, R. (2015). Matlab-based simulator of cooperative spectrum sensing in real channel conditions. In *25th International Conference Radioelektronika (RADIOELEKTRONIKA),* . pp. 209–212.

[116] Wei, H., Yang, L. L., & Hanzo, L. (2005). Interference-free broadband single- and multicarrier DS-CDMA. *EEE Communications Magazine* vol. 43 no. 2, pp. 68–73.

[117] IEEE Std 802.22-2011 *IEEE Standard for Information Technology - Telecommunications and information exchange between systems Wireless Regional Area Networks (WRAN) .*

[118] Wang, J., Liu, K., Xiao, K., Chen, C., Wu, W., Lee, V. C., & Son, S. H. (2017). Dynamic Clustering and Cooperative Scheduling for Vehicle-to-Vehicle Communication in Bidirectional Road Scenarios. *IEEE Transactions on Intelligent Transportation Systems.*

[119] Mecklenbrauker, C., Bernado, L., Klemp, O., Kwoczek, A., Paier, A., Schack, M., & Zemen, T. (2012). Vehicle-to-Vehicle Communications. In *Pervasive Mobile and Ambient Wireless Communications*, Springer, London, pp. 577–608.

[120] Harding, J., Powell, G., Yoon, R., Fikentscher, J., Doyle, C., Sade, D., & Wang, J. (2014). *Vehicle-to-vehicle communications: Readiness of V2V technology for application,* No. DOT HS 812 014.

[121] Kemp, A. H., & Barton, S. K. (2005). The impact of delay spread on irreducible errors for wideband channels on industrial sites. In *Wireless Personal Communications*, vol. 34, no. 3, pp. 307–319.

[122] Durgin, G., Rappaport, T. S., & Xu, H. (1998). Measurements and models for radio path loss and penetration loss in and around homes and trees at 5.85 GHz. *IEEE Transactions on Communications*, vol. 46, no. 11, pp. 1484–1496.

[123] Falcone, P., Colone, F., Bongioanni, C., & Lombardo, P. (2010). Experimental results for OFDM WiFi-based passive bistatic radar. In *IEEE Radar Conference*, pp. 516–521.

[124] Blossom, E. (2004). GNU radio: tools for exploring the radio frequency spectrum. In *Linux journal*, vol. 4, no. 122.

[125] Ettus, M., & Braun, M. (2015). The universal software radio peripheral (usrp) family of low-cost sdrd. *Opportunistic Spectrum Sharing and White Space Access: The Practical Reality*, pp. 3–23.

[126] Troxel, G. D., Blossom, E., Boswell, S., Caro, A., Castineyra, I., Colvin, A., & Hussain, T. (2006). Adaptive dynamic radio open-source intelligent team (ADROIT): Cognitively-controlled collaboration among SDR nodes. In *IEEE 1 st Workshop on Networking Technologies for Software Defined Radio Networks*, pp. 8–2317.

[127] Islam, M. N., Kim, B. J. J., Henry, P., & Rozner, E. (2013). A wireless channel sounding system for rapid propagation measurements. In *IEEE International Conference on Communications (ICC)*, pp. 5720–5725.

[128] Merwaday, A., Rupasinghe, N., Guvenc, I., Saad, W., & Yuksel, M. (2014). USRP-based indoor channel sounding for D2D and multi-hop communications. In *IEEE 15th Annual Wireless and Microwave Technology Conference (WAMI-CON)*, pp. 1–6.

[129] Maas, D., Firooz, M. H., Zhang, J., Patwari, N., & Kasera, S. K. (2012). Channel sounding for the masses: Low complexity gnu 802.11 b channel impulse response estimation. *IEEE Transactions on Wireless Communications*, vol. 11, no. 1, pp. 1–8.

[130] Garcia-Pardo, C., Molina-Garcia-Pardo, J. M., Rodriguez, J. V., & Juan-Llacer, L. (2010). Comparison between time and frequency domain MIMO channel sounders. In *IEEE 72nd Vehicular Technology Conference Fall (VTC 2010-Fall)*, pp. 1–5.

[131] Moschevikin, A., Tsvetkov, E., Alekseev, A., & Sikora, A. (2016). Investigations on passive channel impulse response of ultra wide band signals for monitoring and safety applications. In *3rd International Symposium on Wireless Systems within the Conferences on Intelligent Data Acquisition and Advanced Computing Systems (IDAACS-SWS)*, pp. 97–104, 2016.

[132] Gahadza, M., Kim, M., & Takada, J. I. (2009). Implementation of a channel sounder using gnu radio open source sdr platform. *Grad. School of Engineering, Tokyo Institute of Technology.*

[133] Nilsson, R., & van de Beek, J. (2016). Channel measurements in an open-pit mine using USRPs: 5G-expect the unexpected. In *IEEE Wireless Communications and Networking Conference Workshops (WCNCW)*, pp. 212–217.

[134] Rappaport, T. S. (2002). *Wireless communications: principles and practice.* 2nd ed. Upper Saddle River, NJ, USA: Prentice-Hall, 2002.

[135] Daoben, L., Deng, Y., Leroudier, F., & Jacks, E. (2000). Physical Layer Specification for LAS-2000. *CWTS - China Wireless Telecommunication Standards,* Vancouver, Canada.

[136] Choi, J. H., Chung, H. K., Lee, H., Cha, J., & Lee, H. (2006). Code-division multiplexing based MIMO channel sounder with loosely synchronous codes and Kasami codes. In *64th Vehicular Technology Conference, VTC-2006 Fall,* pp. 1–5.

[137] Yue-liang, L., Yu-zhong, J., & Wei, Z. (2011). Interpolation algorithm of Zadoff-Chu sequence. In *International Conference on Mechatronic Science, Electric Engineering and Computer (MEC)*, pp. 1183–1187, 2011.

[138] Budisin, S. (2010). Decimation generator of zadoff-chu sequences. In *In International Conference on Sequences and Their Applications*, pp. 30–40, Springer, Berlin, Heidelberg.

[139] ETSI, E. T. 136 211 V14. 2.0: LTE. E-UTRA; Physical Channel and Modulation, 2017.

[140] Hou, X., Zhang, Z., & Kayama, H. (2009). DMRS design and channel estimation for LTE-advanced MIMO uplink. In *IEEE 70th Vehicular Technology Conference Fall (VTC 2009-Fall)*, pp. 1–5.

[141] Bertrand, P. (2011). Channel gain estimation from sounding reference signal in LTE. In *IEEE 73rd Vehicular Technology Conference (VTC Spring)*, pp. 1–5.

[142] Wen, Y., Huang, W., & Zhang, Z. (2006). CAZAC sequence and its application in LTE random access. In *Information Theory Workshop, 2006. ITW'06 Chengdu*, pp. 544–547.

[143] Rohrs, U. H., & Linde, L. P. (1992). Some unique properties and applications of perfect squares minimum phase CAZAC sequences. In *Proceedings of the 1992 South African Symposium on Communications and Signal Processing, COMSIG'92*, pp. 155–160.

[144] 3GPP, 3rd generation partnership project (2018). Technical Specification Group Radio Access Network; User Equipment (UE) radio transmission and reception. *3GPP TS 38.101-1 V1.0.0,* France: Organizational Partners (ARIB, ATIS, CCSA, ETSI, TTA, TTC).

[145] Guan, K., Ai, B., Nicolas, M. L., Geise, R., Moller, A., Zhong, Z., & Kurner, T. (2016). On the Influence of Scattering From Traffic Signs in Vehicle-to-X Communications. In *IEEE Trans. Vehicular Technology*, vol. 65, no. 8, pp. 5835–5849.

[146] Sun, S., Rappaport, T. S., Rangan, S., Thomas, T. A., Ghosh, A., Kovacs, I. Z., Rodriguez, I., Koymen, O., Partyka, O., & Jarvelainen, J. (2016). Propagation path loss models for 5G urban micro-and macro-cellular scenarios. In *83rd IEEE Vehicular Technology Conference (VTC Spring)*, pp. 1–6.

[147] Chen, J., Yin, X., Tian, L., Zhang, N., He, Y., Cheng, X., Duan, W., & Ruiz Boque, S. (2014). Measurement-based LoS/NLoS channel modeling for hot-spot urban scenarios in UMTS networks. In *International Journal of Antennas and Propagation*, vol. 2014.

[148] Li, J., Zhao, Y., Tao, C., & Ai, B. (2017). System design and calibration for wideband channel sounding with multiple frequency bands. In *IEEE Access*, vol. 5, pp. 781–793.

[149] Kristem, V., Bas, C. U., Wang, R., & Molisch, A. F. (2018). Outdoor Wideband Channel Measurements and Modeling in the 3-18 GHz Band. In *IEEE Transactions on Wireless Communications*, vol. 17, no. 7.

[150] Healey, A., Bianchi, C. H., & Sivaprasad, K. (2000). Wideband outdoor channel sounding at 2.4 GHz. In *2000 IEEE-APS Conference on Antennas and Propagation for Wireless Communications*, pp. 95–98.

[151] Liang, J., Lee, J., Kim, M. D., & Kim, J. (2014). Experimental wideband spatial correlation measurements of low-height mobiles in outdoor urban environments. In *2014 International Conference on Information and Communication Technology Convergence (ICTC)*, pp. 854–857.

[152] Wang, W., Jost, T., & Fiebig, U. C. (2015). A Comparison of Outdoor-to-Indoor Wideband Propagation at S-Band and C-Band for Ranging. In *IEEE Transactions on Vehicular Technology*, vol. 64, no. 10, pp. 4411–4421.

[153] Suikkanen, E., Hentila, L., & Meinila, J. (2010). Wideband radio channel measurements around 800 MHz in outdoor to indoor and urban macro scenarios. In *Future Network and Mobile Summit*, pp. 1–9.

[154] Nie, X., Zhang, J., Liu, Z., Zhang, P., & Feng, Z. (2010). Experimental investigation of mimo relay transmission based on wideband outdoor measurements at 2.35 GHz. In *Wireless Communications and Networking Conference (WCNC)*, pp. 1–6.

[155] Molina-Garcia-Pardo, J. M., Lienard, M., & Degauque, P. (2009). Propagation in tunnels: Experimental investigations and channel modeling in a wide frequency band for MIMO applications. *EURASIP Journal on Wireless Communications and Networking*, pp. 1–9.

[156] Di Benedetto, M. G., Kaiser, T., & Molisch, A. F. (2006). *UWB communication systems: a comprehensive overview*. Hindawi Publishing Corporation, vol. 5.

[157] Hashemi, H., & Tholl, D. (1994). Statistical modeling and simulation of the RMS delay spread of indoor radio propagation channels. *IEEE Transactions on Vehicular Technology*, vol. 43 no. 1, pp. 110–120.

[158] Rappaport, T. S., MacCartney, G. R., Samimi, M. K., & Sun, S. (2015). Wideband millimeter-wave propagation measurements and channel models for future wireless communication system design. *IEEE Transactions on Communications*, vol. 63 no. 9, pp. 3029–3056.

[159] Sangodoyin, S., Niranjayan, S., & Molisch, A. F. (2016). A measurement-based model for outdoor near-ground ultrawideband channels. *IEEE Transactions on Antennas and Propagation*, vol. 64 no. 2, 740–751.

[160] Wang, Y., Lu, W. J., & Zhu, H. B. (2013). Propagation characteristics of the LTE indoor radio channel with persons at 2.6 GHz. *IEEE Antennas and Wireless Propagation Letters*, vol. 12, pp. 991–994.

[161] Tonello, A. M., Versolatto, F., & Bejar, B. (2011). A top-down random generator for the in-home PLC channel. In *Global Telecommunications Conference (GLOBECOM 2011)*, pp. 1–5.

LIST OF SYMBOLS, PHYSICAL CONSTANTS AND ABBREVIATIONS

H_{est} Estimated channel matrix in FD

H_{ALMMSE} ALMMSE estimated channel matrix in FD

M_{sc}^{RS} Number of subcarriers in the reference signal

$M_{symb}^{(layer)}$ Number of modulation symbols per layer

n_s Slot number within a radio frame

n_{sc} Adaptive linear minimum mean square error

c_i Average channel power

N_{symb}^{UL} Number of SC-FDMA symbols in an uplink slot

R_{h,h_p} Cross-correlation matrix

R_{h_p,h_p} Auto-correlation matrix

P   Number of antenna ports

α Cyclic shift

σ_w^2 Noise distribution

τ Relative delay for the used channel

υ Subcarrier spacing

$\triangle f$ Number of transmission layers

$T(r)$ Test statistic

σ_n^2 Noise variance

$r(n)$ Received signal

J Indicator function

$F(x)$ Empirical CDF function

$G(x)$ Theoretical CDF function

$P_{d,i}$ Probability of detection

$k(\alpha, N)$	Critical value for K-S test
$P_{fa,i}$	Probability of false alarm
P_{tot}	total power
r	partitioning radius
T_{KS}	K-S test statistics
γ	Threshold of signal presence
Γ	Edge region Signal to Noise ratios
τ_w	channel delay of wth path
PL_F	free space path loss
d	distance
d_0	Reference distance
PL	path loss
n	path loss exponent
L_{LA}	LA code length
M_{LA}	Minimum spacing durations between non-zero pulses
K_{LA}	Number of ± 1 pulses
LSN_{com}	Complementary code length (CCs)
P_{LS}	Walsh-Hadamard matrix dimensions
W_{LS}	Number of zeros between CCs
N_{ZC}	Zadoff-Chu sequence length
N_{step}	Number of steps
N_{fr}	Number of frames
$\bar{\tau}$	Mean excess delay
w	Path number
φ_w	Phase characterize channel path

σ_τ	Root mean square delay spread
B_c	Coherence bandwidth
3GPP	3rd Generation partnership project
4G	4th Generation of mobile communications
ADC	Analog to digital converter
ALMMSE	Adaptive linear minimum mean square error
AP	Access point
AWGN	Additive white Gaussian noise
BER	Bit error rate
BS	Base station
BW	Bandwidth
CP	Cyclic prefix
CBS	Clustering to the base station
CCE	Clustering to the cell edge
CCI	Co-channel interference
CDF	cumulative distribution function
CFR	Conventional frequency reuse
CRN	Cognitive radio networks
D2D	Device to Device
D-FFR	Dynamic fractional frequency reuse
D-FFR	Energy detection
CQI	Channel quality indication
CRC	Cyclic redundancy check
D2D	Device to device
DAC	Digital to analog converter

DDC   Digital down converter

DMRS   Demodulation reference signals

DSP   Digital signal processing

DFT   Discrete time Fourier transformation

DUC   Digital up converter

eNodeB   E-UTRAN Node B

ETSI   European telecommunications standards institute

FFT   Fast Fourier transform

FC   Fusion center

FFR   Fractional frequency reuse

FM   Frequency modulation

FPGA   Field programmable gate array

FR   Full reuse

FRF   Frequency reuse factor

FSPL   Free space path loss

GPS   Global positioning system

IEEE   Institute of electrical and electronics engineers

IF   Intermediate frequency

IMT-Advanced   International mobile telecommunications - advanced

ITU   International telecommunication union

ICI   Inter-cell interference

IDMA   Interleave division multiple access

K-S   Kolmogorov-Smirnov

LNA   Low noise amplifier)

LPF   Low pass filter

LTE	Long term evolution
LTE-A	Long term evolution-advanced
MIMO	Multiple input multiple output
OFDM	Orthogonal frequency division multiplexing
PA	Power amplifier
PC	Personal computer
PCC	Polynomial cancellation coding
Ped	Pedestrian
PDN	Packet data network
PER	Packet error rate
PFR	Partial frequency reuse
PR	Partial reuse
PSK	Phases shift keying
PU	Primary user
PUCCH	Physical uplink control channel
PUSCH	Physical uplink shared channel
QPSK	Quadrature phase shift keying
QAM	Quadrature amplitude modulation
QoS	Quality of service
ROC	Receiver operating characteristics
SC-OFDMA	Signal carrier-orthogonal frequency division multiple access
SDR	Software defined radio
SFR	Soft frequency reuse
SINR	Signal to interference plus noise ratio
SISO	Single Input Single output

SNR	Signal to noise ratio
SSD	Soft sphere detection
SU	Secondary user
UL	Uplink
UD	Uniform distribution
USRP	Universal software radio peripheral
ZF	Zero forcing
Veh	Vehicular